Investigations of $SrRuO_3$ and Sr_2RuO_4

by

Özhan Ünverdi

A Doctoral Thesis
Submitted in partial fulfilment of the requirements
for the award of

Doctor of Philosophy of Loughborough University

October 2005

Abstract

The structural and magnetic properties of perovskites $SrRuO_3$, $CaRuO_3$, $Sr_{(1-x)}Ca_xRuO_3$ (x= 0.5, 0.75) and the layered perovskite Sr_2RuO_4 have been investigated using X-ray diffraction, neutron scattering and SQUID measurements. $SrRuO_3$ is ferromagnetic with a transition temperature of T_C=162K. It remains orthorhombic up to 450K. $CaRuO_3$ is paramagnetic down to 2K and shows no structural phase transition between 2K and 300K. Sr_2RuO_4 is neither magnetically ordered nor does it changes its crystallographic structure between 2K and 450K. The nature of the magnetism in $SrRuO_3$ has been found to originate from itinerant 4*d* band electrons. $CaRuO_3$ possesses a narrower 4*d* band compared to $SrRuO_3$. The width of the 4*d* band in $CaRuO_3$ does not allow any magnetic order. The unit cell differences between $SrRuO_3$ and $CaRuO_3$ are also due to the band structure. Paramagnetic neutron scattering also supports the notion of itinerant 4*d* band magnetism in these ruthenates.

Acknowledgment

I would like to thank my supervisor Dr Klaus-Ulrich Neumann for his constant support and encouragement, for proof-reading hundreds of thesis drafts, beautiful "time-outs" while doing experiments at the ILL, and helping me throughout my research project whenever I was in need. I thank Professor Kurt Ziebeck, who greatly enriched my knowledge with his exceptional insight into neutron scattering and condensed matter physics.

My thanks also go to ILL staff: Dr Ross Steward, Dr Amir Murani and Dr Bachir Ouladdiaf for their help, advice and discussions during the neutron scattering experiments and data analysis.

I would also like to thank Ms Maureen McKenzie and Mrs. Tania Moore, who are the most beautiful angels of our department, for their kindly help during my time in the department. I am grateful to our technicians –the secret heroes- Mr Bryan Dennis, Mr Chas Chavda, Mr Martin Stenlake, Raj Pancholi and Ramesh Pancholi.

I am deeply indebted to Professor Feodor Kusmartsev who helped me to find funding during my PhD. Without his help, this work would not have been possible.

My friends with whom I have spent fascinating times and shared unforgettable moments in Loughborough: Yiğit and his wife Ebru, Volkan and his wife Berna, Becky, Mihalis, Nektaria, Nora, Katerina, my undergrad friend Dr Aşan Bacak and his girlfriend Celine, my "colleagues" Tamsin, Stefan, Kristin, Michael, Julia and Nina deserve huge thanks as well.

I would also like to thank my lecturers from Ondokuz Mayis University who have introduced me to the fundamentals of physics during my undergraduate years.

And special thanks go to my wife and my parents who have supported me unconditionally during my research.

Contents

Chapter 1

Introduction

1.1 General Introduction

Transition metal oxides exhibit a variety of physical properties. The discovery of high-T_C cuprate superconductors [1] has drawn much attention to transport in metal oxides, particularly to those which have perovskite-related structures. Among those, the series of ruthenium oxides have very interesting structural, electrical, and magnetic properties [2]. The crystallographic structure and magnetic structure of the layered ruthenates $Sr_{x+1}Ru_xO_{3x+1}$ ($SrRuO_3$ when x= ∞ and Sr_2RuO_4 when x=1) and $Sr_xCa_{1-x}RuO_3$ (x= 0, 0.5, 0.75) have been investigated using X-ray diffraction, neutron scattering and SQUID measurements to determine the electron correlations in Ru-based oxides.

The n = 1 compound Sr_2RuO_4 is the first example of an unconventional noncuprate layered perovskite superconductor at low temperatures (T_C =0.93K) [3, 4]. Magnetically it is a paramagnetic metal.

Since the observation of superconductivity in $La_{2-x}Ba_xCuO_4$ (LBCO) [1], several superconducting copper oxides have been discovered, forming a new class of superconductors with remarkably high transition temperatures, namely high-temperature superconductors (HTSCs). The most peculiar feature commonly seen in HTSCs is that all of them have a layered perovskite crystal structure containing a planar CuO_2 network. It has been well recognized that, in the CuO_2 planes, significant and large hybridisation between the Cu $d(x^2-y^2)$ and O $p\sigma$ states is a crucial factor in describing the electronic structure as well as the strong correlation on the Cu site. A number of efforts have been made for some years to find a layered perovskite superconductor without copper but no one has succeeded until very recently. Maeno *et al.* [3,5] discovered superconductivity at 0.93 K in the non-copper-oxide Sr_2RuO_4 with the same crystal structure as LBCO [5].

The crystal structure of Sr_2RuO_4 is of the K_2NiF_4 [6] structure type which is realized for a considerable number of compounds with the general composition A_2BX_4 [7, 8]. The structure can be built up theoretically by perovskite monolayers stacked along the *c*-axis where the layers 1 and 3 are ABX_3 perovskite cells centred with atoms of type *A*, while layer 2 is centred with *B* atoms.

The n = ∞ compounds $SrRuO_3$, $CaRuO_3$ and $Sr_{(1-x)}Ca_xRuO_3$ have also a layered perovskite structure with a similar crystallographic structure. In despite of the similarity in crystallographic structure, the magnetic properties show quite different behaviour [9, 10].

Perovskite $SrRuO_3$ has been known for quite some time [11]. However, it has become the subject of considerable attention lately, both because of its relationship with the unconventional superconductor Sr_2RuO_4 and because of its unusual position as a *4d* metallic perovskite oxide ferromagnet. The Curie temperature is high, $T_C \approx 165K$, and the magnetisation of $1.6 \pm 0.4\ \mu_B/Ru$ [4, 12] is significant. The octahedral crystalline electric field of O atoms splits the fivefold degeneracy of the Ru $4d^4$ configuration into a triplet (t_{2g}) ground state, two-third occupied, and a doublet (e_g) excited state, which is unoccupied [13].

$SrRuO_3$ occurs in a distorted perovskite structure, specifically, of the $GdFeO_3$ type, with orthorhombic P*nma* symmetry as is typical in perovskite with an A-site cation that is too small relative to the B-site. The distortions consist of rotations of the oxygen octahedra with very little change in Ru-O bond lengths [14, 15].

In addition $SrRuO_3$ exhibits a structural phase transition at high temperatures. At room temperatures it has an orthorhombic structure ($a \neq b \neq c$, where a=5.5304(1) Å, b=7.8446(2) Å and c=5.5670(1) Å [14]). At 823 K it changes to a tetragonal structure ($a=b \neq c$, where $a=b$=5.5784(2) Å and c=7.9078(78) Å) and at 973 K it becomes cubic ($a=b=c=3.9557(1)$ Å) [16].

$CaRuO_3$ has the same crystal structure and symmetry as $SrRuO_3$, with the exception that the octahedral rotations are approximately twice as large, reflecting the smaller size of the Ca^{2+} ion relative to Sr^{2+} [13]. Although initially reported as antiferromagnetic [17], it is now established to be a paramagnetic metal down to low temperatures [15, 18]. The LSDA (Local Spin Density Approximation) calculations for $CaRuO_3$ but using the crystal structure of $SrRuO_3$ yield magnetic properties that are practically the same as those of

$SrRuO_3$. The difference between $CaRuO_3$ and $SrRuO_3$ is therefore clearly structural in origin [4, 17].

In the literature it is claimed that the $CaRuO_3$ has a cubic structure with $a=b=c=3.910(1)$ Å [19]. However, no cubic structure has been observed in any scattering experiment.

Ca dopped $SrRuO_3$ compounds, $Sr_{(1-x)}Ca_xRuO_3$ compounds have similar crystallographic structure and symmetry compared to $SrRuO_3$. The unit cell volume decreases with increasing x and the magnetisation vanishes for $x \geq 0.7$ [13]. Here, again the diameter differences between Sr^{2+} and Ca^{2+} plays an important role for the altering of the crystallographic structure.

1.2 Main Objectives of the Research

Ruthenium oxides exhibited a wide variety of physical properties. $SrRuO_3$ and $CaRuO_3$ show metallic properties at room temperature. The outstanding difference in magnetic properties of $SrRuO_3$ and $CaRuO_3$ render solid solutions of $Sr_{(1-x)}Ca_xRuO_3$ quite interesting. $SrRuO_3$ is ferromagnetic below $T_C=160K$, whereas $CaRuO_3$ follows a Curie-Weiss law at high temperatures with a negative Curie-Weiss constant. On the other hand Sr_2RuO_4 is an unconventional superconductor at low temperature ($T_C=1.2K$). All this variety arises from the magnetic and electronic structure of Ruthenium oxides.

The magnetic and electronic structure can be understood by magnetic measurements and polarized neutron scattering experiments. In addition to this, the differences in crystallographic structure also play an important role for their physical properties. With the aid of neutron scattering and X-ray diffraction the crystallographic structure can be obtained.

Details of the electronic correlations as seen in the magnetic behaviour can be investigated using spin polarised neutron scattering. Such an experimental method will focus on the electrons close to the Fermi level, which are also the most relevant for determining the thermodynamic properties of these compounds.

To start the investigation first a detailed crystallographic structure determination is carried out and presented. Secondly, the magnetic properties of some compounds are investigated. Finally, a polarised neutron scattering experiment is performed in order to determine the details of the magnetic behaviour on an atomic scale.

1.3 Structure of the Thesis

The thesis is divided into four chapters.

Chapter one is a general introduction to the research which has been carried out. It points out the aims and gives a short introduction to various aspects of physics which have been relevant for this thesis. It also gives a brief introduction to the properties of compounds and the path that has followed during the research.

Chapter two covers the background of the theory of X-ray scattering, neutron scattering, magnetism and refinements. It also gives a description of crystal field theory as applied to Ruthenium oxides.

Chapter three presents all the experimental results which have been obtained. Detailed information and results of X-ray diffraction experiments, neutron scattering experiments and magnetic measurements are presented in this section.

Chapter four is a discussion of the experimental results. It also contains the conclusion of the whole thesis.

References

[1] Bednorz, J. G., Muller, K.A, *Z. Phys., B* **64**, 189 (1986)

[2] Kiyama, T., *et. al. Phys. Rev., B* **54**, R756 (1996)

[3] Maeno, Y., *et al., Nature (London),* **372**, 532 (1994)

[4] Singh, D. J., Papaconstantopoulos, D. A., *Electronic structure and Magnetism of Complex Materials*, Springer, Berlin, (2002)

[5] Yokoya, T., *et al., Phys. Rev., B* **54**, 13311 (1996)

[6] Neumeier, J. J., *et al., Phys. Rev., B* **50**, 17910 (1994)

[7] Oguchi, T., *Phys. Rev., B* **51**, 1385 (1995)

[8] Walz, L., Lichtenberg, F., *Acta Crys., C* **49**, 1268 (1993)

[9] Longo, J. M., *et al., J.App. Phys.,* **39**, 1327, (1968)

[10] Shikano, M., *Solid State Comm.*, **90**, 115, (1994)

[11] Randal, J. J., *et al., J. Am. Chem. Soc.*, **81**, 2629, (1959)

[12] Fujioka, K., *et al., Phys. Rev., B* **56**, 6380 (1997)

[13] Cao, G., *et al., Phys. Rev., B* **56**, 321, (1997)

[14] Johnes, C. W., *et al., Acta Cryst., C* **45**, 365 (1989)

[15] Chakoumakos, B. C., *et al., Physica B*, **241**, 358, (1998)

[16] Kennedy, B. J., Hunter, B. A., *Phys. Rev., B*, **58**, 653, (1998)

[17] Longo, J. M., *et al., J. Appl. Phys.*, **39**, 1327 (1968)

[18] He, T., Cava, R. J., *Phys. Rev., B* **63**, 1724 (2001)

[19] Bensch, W., *et al., Solid States Ionics,* **43**, 171, (1990)

Chapter 2

Theoretical Background

2.1 X-rays

2.1.1 Introduction

X-rays are electromagnetic radiation of short wavelength, and can be produced by the sudden deceleration of rapidly moving electrons inside a target material. If an electron falls through a potential difference of V volt, it acquires energy of eV electron-volt (eV), where e is the charge of an electron. This energy may be expressed as quanta of X-rays of wavelength λ, where each quantum is given by

$$\lambda = \frac{hc}{eV} \tag{2.1.1}$$

h being Plank's constant and c the speed of light in vacuum. Substitution of numerical values into (2.1.1) leads to:

$$\lambda = \frac{12.4}{V} \quad [\text{Å}] \tag{2.1.2}$$

where V is measured in kilovolt and λ is given in Angström. The wavelength range of X-rays is approximately 0.1-100 Å. For the purposes of practical X-ray crystallography, the range used is approximately 0.6-3.0 Å [1].

X-rays are produced through the impact of electrons on a metal target (anode). The most widely used source of X-rays is the sealed hot-cathode tube. In such a device, electrons emitted from a heated tungsten filament (cathode) are accelerated by a high voltage (40 kV or more) towards a water cooled target anode, usually made of copper or molybdenum. A large proportion of the energy reaching the target is dissipated as heat on account of multiple collisions within the target material, but about 10% of the energy is converted to X-rays. As a consequence, the device can be operated with a higher current density resulting in a more powerful source. If the energy eV is not too high, there will be

a continuous distribution of X-ray wavelengths, or white radiation. As the accelerating voltage V is increased, the intensity of the radiation increases.

At a certain higher value of V_m the impinging electrons begin to excite inner electrons in the target atoms. Then, other electrons from higher energy levels fall back to the inner levels. This transition is accompanied by the emission of X-rays, *characteristic* for the material of the target. In this case, the X-ray wavelength depends on the energies of the two levels involved, E_1 and E_2, such that

$$\lambda = \frac{hc}{|E_2 - E_1|} \tag{2.1.3}$$

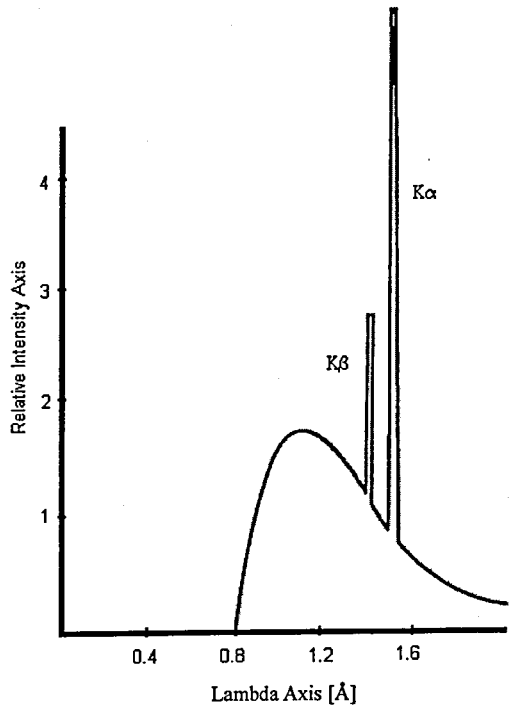

Figure 2.1.1: Characteristic K spectrum from an X-ray tube, superimposed upon the white radiation (continuous spectrum)

Figure 2.1.1. illustrates the curve of radiation intensity against X-ray wavelength, when the accelerating voltage is sufficient to excite the K spectrum of the target metal. The K spectrum consist of the K_α and K_β wavelengths, which are always produced together, and

correspond to electrons falling back from the L and M levels, respectively to the K-shell. Two slightly different L energy levels exist, so that the important K_α spectrum consist of two components of closely similar wavelength, $K_{\alpha 1}$ and $K_{\alpha 2}$. The wavelength of K radiation for a target material of copper are K_β=1.3926 Å, $K_{\alpha 1}$=1.54056 Å and $K_{\alpha 2}$=1.54437 Å respectively. The mean value for K_α is obtained by averaging the $K_{\alpha 1}$ and $K_{\alpha 2}$ wavelength in their intensity ratio of 2:1, thus giving the average value of 1.54183 for K_α; the α_1- α_2 doublet is resolved when the scattering angle is large, that is, at high values of the Bragg angle θ [1, 2].

2.2.2 Bragg Law

When X-rays of wavelength λ are directed onto a correctly oriented single crystal at an angle θ, diffraction will occur which arises due to parallel atomic planes of separation d. The amplitude of the diffracted X-ray beam will be maximal when the path difference between rays reflected from successive planes is equal to an integer multiple of the wavelengths ($n\lambda$). The relation which describes this phenomenon is called *Bragg's law*. Bragg's law is a consequence of the periodicity of the lattice. (Fig.2.1.2)

$$n\lambda = 2d\sin\theta \qquad (2.1.4)$$

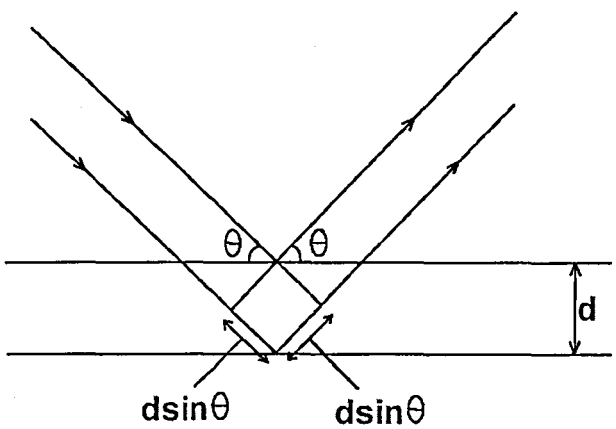

Figure 2.1.2: Illustration of Bragg's Law

2.2 Neutron Diffraction

2.2.1 Introduction

The neutron is a chargeless, elementary particle of mass m_n=1.675x10^{-27} kg spin ½ and it possesses an intrinsic magnetic dipole moment μ_n=1.042x10$^{-3}\mu_B$ [6]. On account of these properties, the neutron is subjected to scattering of magnetic as well as nuclear origin and therefore permits the experimental investigation of both nuclear and magnetic solid state phenomena on an atomic scale. Its intrinsic properties are as follows:

- The mass of the neutron results in the de Broglie wavelength of thermal neutrons being of the order 1 → 3 Å. This is of the same order of magnitude as the interatomic distances in solids. The interference effects that consequently occur yield information on both the nuclear and magnetic structure of the scattering system.
- The neutron is a neutral particle and thus it can penetrate deeply into the target and close to the nuclei without having to overcome a Coulomb barrier due to electrostatic forces.
- The neutron has an intrinsic magnetic moment, which interacts with the unpaired electrons in magnetic atoms.
- The energy of thermal neutrons is of the same order as that of many excitations in condensed matter. Thus, the analysis of the energy of the inelastically scattered neutrons gives information on the dynamic processes occurring in solids due to the coherent motion of the nuclei (phonons) or that of the magnetic moments (magnons).

The energy E of a neutron with a wave vector $\vec{k}$ is

$$E = \frac{\hbar^2 k^2}{2m} \qquad (2.2.1)$$

where m is the neutron mass. It is sometimes useful to rewrite the energy relation (eq.2.2.1) in terms of the neutron wavelength λ or alternatively the inverse relation

$$\lambda = \sqrt{\frac{h^2}{2mE}} \tag{2.2.2}$$

can be used.

Low energy neutron beams (high wavelengths) are often described as being cold, thermal, and hot or epithermal.

In an actually scattering experiment the key variables are the change in the neutron energy and the concomitant change in wave vector. If $\hbar\omega$ and $\vec{\kappa}$ is the transfer of energy and wave vector to the target sample, thus,

$$\hbar\omega = E - E' = \frac{\hbar^2}{2m}\left(k^2 - k'^2\right) \tag{2.2.3}$$

where E, $\vec{k}$ is the initial and $E', \vec{k}'$, are the final states. The scattering vector is then written

$$\vec{\kappa} = \vec{k} - \vec{k}' \tag{2.2.4}$$

The spectrum of the scattered neutrons is a function of $\vec{\kappa}$ and not some other function of $\vec{k}$ and $\vec{k}'$ [5].

It is evident from (2.2.3) and (2.2.4) that ω and κ are related. The relation imposes kinematical constrains on the scattering experiments. For example not all of (ω, κ) is accessible in a neutron scattering experiment. The kinematically allowed region is a function of the incident neutron energy E and lies between the (ω, κ) corresponding to forward and backward scattering.

2.2.2 Definitions of cross sections

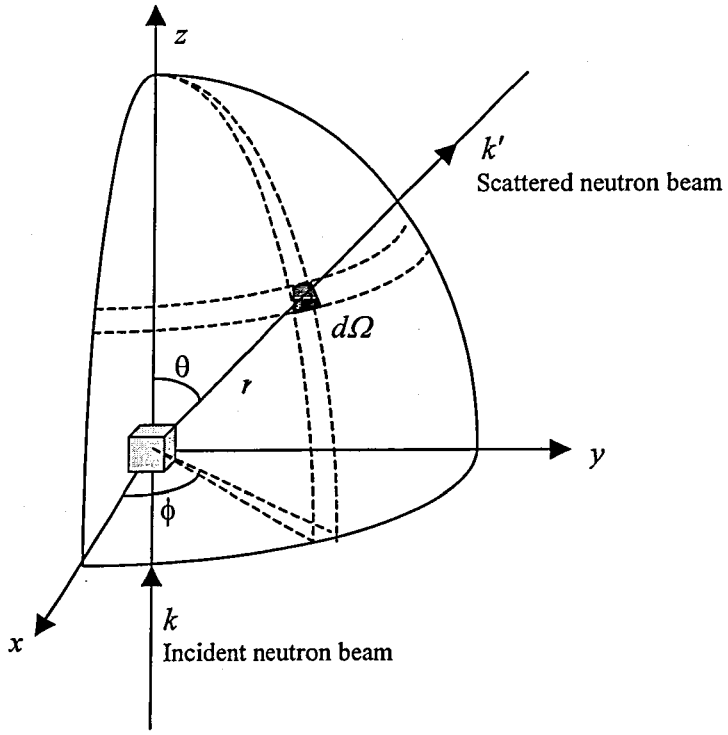

Figure 2.2.1.: Geometry of scattering experiment and cross section

Various types of measurement can be made on the neutrons after they have interacted with the scattering system. The result in each case can be expressed in terms of a quantity known as a cross section.

To specify the geometry of the scattering process polar coordinates are used (fig.2.2.1). If the directions of scattering neutrons are θ and ϕ then the double cross section is defined by

$$\frac{\partial^2\sigma}{\partial\Omega\partial E'} = \frac{\left(\begin{array}{l}\text{Number of neutrons scattered per second into}\\ \text{the solid angle } d\Omega \text{ in direction } (\theta,\phi) \text{ with}\\ \text{energy between } E' \text{ and } E'+dE'\end{array}\right)}{\Phi d\Omega dE'} \qquad (2.2.5)$$

where Φ is the flux of the incident neutrons and E' is the energy of the scattered neutrons. The dimension of the double differential scattering cross section is [area].

If only the scattered neutrons into a solid angle $d\Omega$ in the direction θ, ϕ are analysed, not the energy, the cross section corresponding to this measurement is known as the differential cross section, and it is defined by

$$\frac{\partial\sigma}{\partial\Omega} = \frac{\left(\begin{array}{l}\text{Number of neutrons scattered per second into} \\ \text{the solid angle } d\Omega \text{ in the direction } (\theta, \phi)\end{array}\right)}{\Phi d\Omega} \tag{2.2.6}$$

The *total scattering cross section* is defined by the equation

$$\sigma_{tot} = \frac{(\text{Total number of neutrons scattered per second})}{\Phi} \tag{2.2.7}$$

The total numbers means the total number of neutrons scattered in any direction.

From their definitions the three cross section are related by the following equations

$$\frac{\partial\sigma}{\partial\Omega} = \int_0^\infty \left(\frac{d^2\sigma}{d\Omega dE'}\right) dE' \tag{2.2.8}$$

$$\sigma_{tot} = \int_\Omega \left(\frac{d\sigma}{d\Omega} d\Omega\right) \tag{2.2.9}$$

If the scattering is axially symmetric, i.e. if $d\sigma/d\Omega$ depends only on θ and not on ϕ, eq. 2.2.9 becomes

$$\sigma_{tot} = \int_0^\pi \frac{d\sigma}{d\Omega} 2\pi \sin\theta \, d\theta \tag{2.2.10}$$

2.2.3 Nuclear Scattering

2.2.3.1 Scattering of neutrons by a single fixed nucleus

Plane wave of neutrons are described by a wave-function of the form [6]

$$\psi_{inc} = e^{ikz} \tag{2.2.11}$$

where $k = 2\pi / \lambda$ is the wave-number, is incident on a nucleus. The scattered wave will be spherically symmetric of the form

$$\psi = -\frac{b}{r} e^{ikr} \tag{2.2.12}$$

where r is the distance of the point of measurement from the origin to which the nucleus is considered to be rigidly fixed. The quantity b, which has the dimension of length, is defined as the scattering length and is a complex quantity

$$b \equiv \alpha + i\beta \tag{2.2.13}$$

However, the imaginary component only becomes important for nuclei which have a high absorption coefficient, such as cadmium or boron. If the scattering length is real, the resultant neutron wave will be given by

$$\psi = e^{ikz} - \frac{b}{r} e^{ikr} \tag{2.2.14}$$

The definition of the scattering cross section (eq. 2.2.7)

$$\begin{aligned} \sigma_{tot} &= \frac{(\text{Total number of neutrons scattered per second})}{\Phi} \\ &= 4\pi r^2 v \frac{\left|(b/r)e^{ikr}\right|^2}{v\left|e^{ikz}\right|^2} \\ &= 4\pi b^2 \end{aligned} \tag{2.2.15}$$

where v is the neutron velocity [6, 7].

The neutron interacts only very weakly with matter, and does so without disturbing the intrinsic properties of the target sample. The amplitude of a wave scattered from one nucleus is very small at the position of neighbouring nuclei. This condition allows the total scattering amplitude for an array of nuclei to be treated as the coherent sum of those for the individual nuclei.

2.2.3.2 Scattering from an assembly of nuclei

If the target sample has no internal structure, then clearly the energy of the scattered neutron is identical to that of the incident neutron. To calculate the differential cross section for this the probability of a transition from the plane-wave state should be known. The transition is from $\vec{k}$ to $\vec{k}'$ and the energy is $E = \hbar^2 k^2 / 2m$ for both. This probability is given by Fermi's Golden rule, namely [5]:

$$W_{K\to K'} = \frac{2\pi}{\hbar}\left|\int d\vec{r}\,\psi^*_{\vec{k}'}\hat{V}\psi_{\vec{k}}\right|^2 \rho_{\vec{k}'}(E) \qquad (2.2.16)$$

Here $\hat{V}$ is the interaction potential that causes the transition, in this case the interaction is between the incident neutron and the target sample, and $\rho_{\vec{k}'}(E)$ is the density of final scattering states per unit energy range.

One can obtain an expression using the standard device in quantum mechanics, known as *box normalisation*, for the density of final scattering states $\rho_{\vec{k}'}(E)$. This is achieved by confining the neutron and target system to a large box of volume L^3, such that only those neutron states with a de Broglie wavelength periodic with respect to the box are allowed. Doing so, one obtains for the density of final states

$$\rho_{\vec{k}'}(E) = \left(\frac{L}{2\pi}\right)^3 \frac{mk'}{\hbar^2} d\Omega \qquad (2.2.17)$$

To obtain the cross section the incident flux of the neutrons should be determine. This is:

$$\frac{(velocity\ of\ incident\ neutrons)}{L^3} = \frac{\hbar k}{mL^3} \tag{2.2.18}$$

Hence from eq.2.2.16, eq.2.2.17 and eq.2.2.18

$$\begin{aligned} d\sigma &= \frac{W_{k\to k'}}{\Phi} \\ &= L^6\left(\frac{m}{2\pi\hbar^2}\right)^2 \left|\int d\vec{r}\,\psi^*_{\vec{k}'}\hat{V}\psi_{\vec{k}}\right|^2 d\Omega \end{aligned} \tag{2.2.19}$$

and

$$\frac{m}{2\pi\hbar^2}\int d\vec{r}\,e^{-i\vec{k}'\cdot\vec{r}}\hat{V}e^{-i\vec{k}\cdot\vec{r}} = \left\langle \vec{k}'\middle|\hat{V}\middle|\vec{k}\right\rangle \tag{2.2.20}$$

$$\frac{d\sigma}{d\Omega} = \left|\left\langle \vec{k}'\middle|\hat{V}\middle|\vec{k}\right\rangle\right|^2 \tag{2.2.21}$$

gives the desired result for the cross section.

These results might be used for calculating the partial differential cross section that includes inelastic scattering events. For such an event the neutron energy is changed by $\hbar\omega$. A state of the target is labelled by the index λ and the corresponding eigenstate is $|\lambda\rangle$. If the response of the target sample to the neutron interaction is to change from the state labelled λ to the λ', in that case conservation of energy requires

$$\hbar\omega = E_{\lambda'} - E_{\lambda} \tag{2.2.22}$$

If this is taken into account the associated cross section is readily shown to be

$$\left(\frac{d\sigma}{d\Omega}\right)=\frac{k'}{k}\left|\left\langle \vec{k}'\lambda'\left|\hat{V}\right|\vec{k}\lambda\right\rangle\right|^2 \tag{2.2.23}$$

where the factor (k/k') arises from the density of final neutron states divided by the incident neutron flux.

The partial differential cross section is obtained from eq.2.2.23 by incorporating the energy conservation eq.2.2.22. This is accomplished with the aid of a delta function

$$\delta(E+E_\lambda-E'-E_{\lambda'})=\delta(\hbar\omega+E_\lambda-E_{\lambda'}) \tag{2.2.24}$$

so as the partial differential cross section is

$$\left(\frac{d^2\sigma}{d\Omega dE'}\right)_{\lambda'}^{\lambda}=\frac{k'}{k}\left|\left\langle \vec{k}'\lambda'\left|\hat{V}\right|\vec{k}\lambda\right\rangle\right|^2\delta(\hbar\omega+E_\lambda-E_{\lambda'}) \tag{2.2.25}$$

The interaction potential V at a position $\vec{r}$ is selected on the basis that, when inserted, it gives the required results of isotropic scattering for a single nucleus. It turns out that in using the Born approximation, the only form of $V(\vec{r})$ to do so is a delta function and is defined, for a nucleus at position $\vec{R}$, by

$$V(\vec{r})=\frac{2\pi\hbar^2}{m}b\delta(\vec{r}-\vec{R}) \tag{2.2.26}$$

This result is known as the Fermi pseudo-potential. If eq.2.2.26 is substituted into eq.2.2.20 and $\vec{R}$ is set to $\vec{R}=0$, in case of an elastic scattering event ($\lambda=\lambda'$ and $\left|\vec{k}\right|=\left|\vec{k}'\right|$)

$$\left\langle \vec{k}'\left|\hat{V}\right|\vec{k}\right\rangle=\left(\frac{m}{2\pi\hbar^2}\right)\frac{2\pi\hbar^2}{m}b\int d\vec{r}e^{-i\vec{k}'\cdot\vec{r}}\delta(\vec{r})e^{i\vec{k}\vec{r}}=b \tag{2.2.27}$$

From eq.2.2.21

$$\frac{d\sigma}{d\Omega} = |b|^2 \tag{2.2.28}$$

hence the total cross section is

$$\sigma = 4\pi|b|^2 \tag{2.2.29}$$

2.2.3.3 Coherent and incoherent scattering

In practice, a scattering system will consist of isotopic nuclei of varying abundance and spin. Because the scattering length is dependant on both the individual isotope, and the relative orientation of the neutron and nuclear spin (if present), it will not take a single value throughout the assembly. If the scattering length b in an elemental target system varied from one nucleus to another as a result of nuclear spin or the presence of isotopes, then each nucleus type ξ can be assigned a scattering length b_ξ which occurs with a concentration c_ξ. The average value of b for the system is then

$$\overline{b} = \sum_\xi c_\xi b_\xi \tag{2.2.30}$$

and the average of b^2 is

$$\overline{b}^2 = \sum_\xi c_\xi b_\xi^2 \tag{2.2.31}$$

If it is assumed that no correlations exist between the scattering lengths of any nuclei (j and j') and that we have a large number of scattering systems of which the positions and motions of the nuclei are identical but the distribution of b's among the nuclei differs such that every possible distribution is represented once, then the measured cross section will approximately be the cross section averaged over all the systems provided that each system contains a large number of nuclei. This is given by

$$\frac{d^2\sigma}{d\Omega dE'} = \frac{k'}{k}\frac{1}{2\pi\hbar}\sum_{j'j}\overline{b_{j'}, b_j}\int\langle j', j\rangle e^{-i\omega t}dt \tag{2.2.32}$$

where the delta function for energy of eq.2.2.24 has been expressed as an integral with respect to time and

$$\langle j', j\rangle = \left\langle e^{-i\vec{\kappa}\vec{R}_{j'}(0)} e^{i\vec{\kappa}\vec{R}_j(t)}\right\rangle \tag{2.2.33}$$

The assumption that the scattering length of different nuclei are not correlated means that the following conditions apply

$$\begin{aligned}\overline{b_{j'}b_j} &= (\bar{b})^2, \quad j' \neq j \\ \overline{b_{j'}b_j} &= \overline{b^2}, \quad j' = j\end{aligned} \tag{2.2.34}$$

so that it can be shown [6]

$$\begin{aligned}\frac{d^2\sigma}{d\Omega dE'} = \frac{k'}{k}\frac{1}{2\pi\hbar}(\bar{b})^2\sum_{jj'}\int\langle j', j\rangle \exp^{-i\omega t}\,dt \\ + \frac{k'}{k}\frac{1}{2\pi\hbar}\left\{\overline{b^2} - (\bar{b})^2\right\}\sum_j\int\langle j, j\rangle \exp^{-i\omega t}\,dt\end{aligned} \tag{2.2.35}$$

It is in the above expression that two types of scattering can be distinguished. The first term in eq.2.2.35 represents what is known as *coherent scattering* which can be written

$$\left(\frac{d^2\sigma}{d\Omega dE'}\right)_{coh} = \frac{\sigma_{coh}}{4\pi}\frac{k'}{k}\frac{1}{2\pi\hbar}\sum_{jj'}\int_{-\infty}^{\infty}\left\langle e^{-i\vec{\kappa}\vec{R}_j(0)} e^{i\vec{\kappa}\vec{R}_{j'}(t)}\right\rangle \times e^{(-i\omega t)}dt \tag{2.2.36}$$

and the second term represents the *incoherent scattering* for which the double differential cross section is given by

$$\left(\frac{d^2\sigma}{d\Omega dE'}\right)_{inc} = \frac{\sigma_{inc}}{4\pi}\frac{k'}{k}\frac{1}{2\pi\hbar}\sum_{j}\int_{-\infty}^{\infty}\left\langle e^{-i\vec{\kappa}\vec{R}_j(0)} e^{i\vec{\kappa}\vec{R}_j(t)}\right\rangle \times e^{(-i\omega t)}dt \tag{2.2.37}$$

where

$$\sigma_{coh} = 4\pi(\bar{b})^2, \qquad \sigma_{inc} = 4\pi\{\overline{b^2} - (\bar{b})^2\} \tag{2.2.38}$$

From eq.2.2.36 and 2.2.37 it can be inferred that coherent and incoherent scattering are of vastly different nature. The coherent scattering is a result of strong interference between the waves scattered from different nuclei. It arises due to the correlation between the positions of different nuclei. Indeed strict geometric conditions must be satisfied for the interference to be strong enough to produce this type of scattering. On the other hand, the incoherent scattering is dependant only on the self correlation of one nucleus at different times. For this reason, it does not yield any interference. The cross section is isotropic.

2.2.4 Magnetic Scattering

The elements of the second transition series which includes Ru have incomplete *4d* shells. The arrangements of the *4d* and *5s* shells of some free atoms and ions give some unpaired electrons. These unpaired electrons give rise to a resultant magnetic moment. Interaction of this with the magnetic moment of the neutron, which has a spin quantum number of ½ and a magnetic moment of 1.9 nuclear magnetons [8], produces neutron scattering which is additional to that produced by the nucleus. The determination of the magnetic structures of such materials is a task which can be achieved only by making neutrons scattering measurements.

The magnetic moment of a neutron is defined in terms of a vector of Pauli matrices $\hat{\sigma}$; the spin operator is then proportional to $(\hat{\sigma}/2)$. Denoting the nuclear Bohr magneton by $\mu_N \left(\mu_N = \frac{e\hbar}{2m_p} \right)$ the magnetic moment for a neutron is

$$\hat{\mu} = \gamma \mu_N \hat{\sigma} \tag{2.2.39}$$

where the gyromagnetic ratio γ=-1.91. In addition to this the magnetic moment operator of an electron is given by

$$\hat{\mu}_e = -2\mu_B \hat{s} \tag{2.2.40}$$

2.2.4.1 The partial cross section

The eq.2.2.27 gives the cross section for a specific transition $\lambda \to \lambda'$ due to an interaction V between the neutron and the scattering system. This expression is correct for nuclear scattering of unpolarised neutrons. The spin state of the neutron does not appear; the dependence of the interaction on the spin state of the nucleus-neutron system is allowed for in the value of the scattering length. However, the magnetic potential contains the spin operator $\hat{\sigma}$ explicitly, and it is therefore necessary to specify not only wave vector $\vec{k}$ of the neutron but also its spin state σ. In the description of the magnetic scattering process the spin state σ too must be specified such that a process in which the system changes from state λ to λ' and the neutron changes from state $\vec{k},\sigma$ to $\vec{k}',\sigma'$ the partial cross section is given by

$$\left(\frac{d^2\sigma}{d\Omega dE'}\right)_{\lambda'}^{\lambda} = \frac{k'}{k}\left(\frac{m}{2\pi\hbar^2}\right)^2 \left|\left\langle \vec{k}'\sigma'\lambda' \middle| \hat{V} \middle| \vec{k}\sigma\lambda \right\rangle\right|^2 \delta(\hbar\omega + E_\lambda - E_{\lambda'}) \tag{2.2.41}$$

where V is the magnetic interaction potential between the neutron and the constituent electrons of the system. If one considers the interaction between the neutron and the magnetic field $\vec{B}$ due to a single moving electron then it may be shown [5] that the corresponding interaction potential can be expressed as the sum of two terms arising from the spin and the orbital motion of the electron respectively.

$$V = -\gamma\mu_N \hat{\sigma}\cdot\vec{B}\left\{2\mu_B \hat{\sigma}\cdot curl\left(\frac{\hat{s}\times\vec{R}}{|\vec{R}|^3}\right) - \frac{e}{2m_e c}\left(\hat{p}_e \cdot \frac{\hat{\sigma}\times\vec{R}}{|\vec{R}|^3} + \frac{\hat{\sigma}\times\vec{R}}{|\vec{R}|^3}\cdot\hat{p}_e\right)\right\} \tag{2.2.42}$$

where m_e is the mass of electron, $\hat{p}_e$ is the momentum operator of the electron given by $\hat{p}_e = -i\hbar\nabla_e$ and $\vec{R}$ is the distance from the electron to the point at which the field is measured.

Substituting eq. 2.2.42 into eq.2.2.41 and using the following identities

$$\frac{\vec{R}}{\left|\vec{R}\right|^3} = -\vec{\nabla}\left(\frac{1}{\left|\vec{R}\right|}\right) \tag{2.2.43}$$

and

$$\frac{1}{\left|\vec{R}\right|} = \frac{1}{2\pi^2}\int d\vec{q}\,\frac{1}{q^2}e^{i\vec{q}\cdot\vec{R}} \tag{2.2.44}$$

where $\vec{q}$ is a wave vector. It can be shown that the partial differential cross section representing a magnetic interaction for unpaired electron is given by

$$\frac{d^2\sigma}{d\Omega dE'} = (\gamma r_0)^2 \frac{k'}{k}\sum_{\lambda\lambda'} p_\lambda \langle\lambda|\hat{Q}_\perp^+|\lambda'\rangle\cdot\langle\lambda'|\hat{Q}_\perp|\lambda\rangle\delta(\hbar\omega + E_\lambda - E_{\lambda'}) \tag{2.2.45}$$

where r_0 known as the classical radius of the electron and equal to $\frac{e^2}{m_e c^2}$.

The operator $\hat{Q}_\perp$, related to the magnetisation of the target system, is defined in terms of a spin and orbit contribution as

$$\hat{Q}_\perp = \sum_i e^{i\vec{\kappa}\cdot\vec{r}_i}\left\{\tilde{\kappa}\times(\hat{s}\times\tilde{\kappa}) - \frac{i}{\hbar|\vec{\kappa}|}\tilde{\kappa}\times\hat{p}_i\right\} \tag{2.2.46}$$

where $\tilde{\kappa}$ represents the unit vector in the direction of the scattering vector κ (eq.2.2.4).

For unpolarised neutrons the Kronecker delta function is

$$\sum_\sigma p_\sigma \langle\sigma|\hat{\sigma}_\alpha\hat{\sigma}_\beta|\sigma\rangle = \delta_{\alpha,\beta} \tag{2.2.47}$$

which can be incorporated into the following identity

$$\hat{Q}_{\perp}^{+}\cdot\hat{Q}_{\perp}=\sum_{\alpha\beta}\left(\delta_{\alpha\beta}-\tilde{\kappa}_{\alpha}\tilde{\kappa}_{\beta}\right)\hat{Q}_{\perp}^{+}\hat{Q}_{\perp} \tag{2.2.48}$$

this gives us an alternative expression for eq.2.2.45

$$\begin{aligned}\frac{d^2\sigma}{d\Omega dE'}&=(\gamma r_0)^2\frac{k'}{k}\sum_{\alpha\beta}\left(\delta_{\alpha\beta}-\tilde{\kappa}_{\alpha}\tilde{\kappa}_{\beta}\right)\\&\times\sum_{\lambda\lambda'}p_{\lambda}\langle\lambda|\hat{Q}_{\alpha}^{+}|\lambda'\rangle\cdot\langle\lambda'|\hat{Q}_{\beta}|\lambda\rangle\delta(\hbar\omega+E_{\lambda}-E_{\lambda'})\end{aligned} \tag{2.2.49}$$

where the operator $\hat{Q}$ is related by $\hat{Q}_{\perp}=\tilde{\kappa}\left(\hat{Q}\times\tilde{\kappa}\right)$. In terms of the magnetisation, the operator $Q(\kappa)$ is effectively the Fourier transform of the magnetisation operator $\hat{M}(\vec{r})$. That is

$$\begin{aligned}\hat{Q}(\vec{\kappa})&=\hat{Q}_S(\vec{\kappa})+\hat{Q}_L(\vec{\kappa})\\&=-\frac{1}{2\mu_B}\int\hat{M}(\vec{r})e^{i\vec{\kappa}\cdot\vec{r}}d\vec{r}\\&=-\frac{1}{2\mu_B}\hat{M}(\vec{\kappa})\end{aligned} \tag{2.2.50}$$

where subscripts S and L indicate spin and orbital contributions respectively.

2.2.4.2 Elastic magnetic scattering

The magnetic cross section for a Bravais crystal can be defined [6]:

$$\frac{\partial^2\sigma}{\partial\Omega\partial E} = \frac{(\gamma r_0)^2}{2\pi\hbar}\frac{k'}{k} N\left\{\tfrac{1}{2} gF(\vec{\kappa})\right\}^2 \sum_{\alpha\beta}\left(\delta_{\alpha\beta} - \hat{\kappa}_\alpha\hat{\kappa}_\beta\right)\sum_l e^{i\vec{\kappa}\cdot\vec{l}} \times \int_{-\infty}^{\infty}\left\langle e^{-i\vec{\kappa}\cdot\vec{u}_0(0)} e^{i\vec{\kappa}\cdot\vec{u}_l(t)}\right\rangle \times \left\langle S_0^\alpha(0) S_l^\beta(t)\right\rangle e^{(-i\omega t)} dt \qquad (2.2.51)$$

where $\vec{u}_l(t)$ is the displacement of nucleus from its equilibrium position and $\vec{l}$ is the lattice vector of the nucleus.

For a Bravais crystal with localised electrons the elastic cross sections is obtained from eq.2.2.51 by replacing the matrix elements by their limiting values as $t\to\infty$. As $t\to\infty$ $\left\langle S_0^\alpha(0) S_l^\beta(t)\right\rangle$ becomes independent of time. Thus

$$\lim_{t\to\infty}\left\langle S_0^\alpha(0) S_l^\beta(t)\right\rangle = \left\langle S_0^\alpha\right\rangle\left\langle S_l^\beta\right\rangle \qquad (2.2.52)$$

Substituting eq.2.2.52 in 2.2.51 and integrating with respect to E' gives the elastic cross section

$$\left(\frac{\partial\sigma}{\partial\Omega}\right)_{el} = (\gamma r_0)^2 N\left\{\tfrac{1}{2} gF(\vec{\kappa})\right\}^2 e^{-2W}\sum_{\alpha\beta}(\delta_{\alpha\beta} - \hat{\kappa}_\alpha\hat{\kappa}_\beta)\times\sum_l e^{i\vec{\kappa}\cdot\vec{l}}\left\langle S_0^\alpha\right\rangle\left\langle S_l^\beta\right\rangle \qquad (2.2.53)$$

where $\vec{l}$ is vector in crystal lattice, e^{-2W} is the Debye-Waller factor and $F(\vec{\kappa})$ is the magnetic form factor.

In the absence of an external magnetic field a ferromagnetic crystal is composed of small regions called domains, in each of which the electron spins tend to align in the same direction. If the z-axis is the quantisation axis, then the mean direction of the spins will be;

$$\left\langle S_l^x \right\rangle = \left\langle S_l^y \right\rangle = 0 \tag{2.2.54}$$

and because the z-direction is independent of the site position l,

$$\left\langle S_l^z \right\rangle = \left\langle S^z \right\rangle \tag{2.2.55}$$

From eq.2.2.53, eq.2.2.54 and eq.2.2.55 the elastic scattering cross section for a single domain is

$$\left(\frac{\partial\sigma}{\partial\Omega}\right)_{el} = (\gamma r_0)^2 N \left\{\tfrac{1}{2} g F(\vec{\kappa})\right\}^2 e^{-2W} \left(1 - \hat{\kappa}_\xi^2\right) \left\langle \vec{S}^z \right\rangle^2 \sum_l e^{i\vec{\kappa}\cdot\vec{l}} \tag{2.2.56}$$

The latter term on 2.2.51 can be written:

$$\sum_l e^{i\vec{\kappa}\cdot\vec{l}} = \frac{(2\pi)^3}{v_0} \sum_{\vec{\tau}} \delta\left(\vec{\kappa} - \vec{\tau}\right) \tag{2.2.57}$$

When

$$\vec{\kappa} = \vec{\tau}, \qquad \hat{\kappa}_z = \hat{\tau}\cdot\hat{\eta} \tag{2.2.58}$$

where $\hat{\tau}$ is a unit vector in the direction of $\vec{\tau}$, $\hat{\eta}$ is a unit vector in the mean direction of the spins and v_0 is the volume of the unit-cell the in the crystal lattice. Thus the cross section for a sample with many domains is

$$\left(\frac{\partial\sigma}{\partial\Omega}\right)_{el} = (\gamma r_0)^2 N \frac{(2\pi)^3}{v_0} \left\langle S^\eta \right\rangle^2 \sum_\tau \left\{\tfrac{1}{2} g F(\vec{\tau})\right\}^2 e^{-2W} \times \left\{1 - \left(\hat{\tau}\cdot\hat{\eta}\right)_{av}^2\right\} \delta\left(\vec{\kappa} - \vec{\tau}\right) \tag{2.2.59}$$

The quantity $\langle S^{\eta} \rangle$ is the mean value of the component of the spin in the direction of $\hat{\eta}$ for each domain.

From eq.2.2.59 it can be seen that for a ferromagnetic crystal the magnetic Bragg peaks occur at the same points in reciprocal space as the nuclear Bragg peaks. Both contributions can be distinguished by their dependency on temperature. The magnetic scattering cross section is proportional to $\langle S^{\eta} \rangle^2$, it is very temperature dependent and falls to zero at the Curie temperature. The nuclear scattering varies a little with temperature; the only term in the cross section that is temperature dependent is the Debye-Waller factor. In addition, the magnetic form factor $F(\vec{\tau})$ falls rapidly with the increasing $|\vec{\tau}|$. This is because the form factor is the Fourier transform of the magnetic potential, and the latter has a long range. The nuclear potential on the other hand is very short range, and its Fourier transform is independent of $|\vec{\tau}|$. For a Bravais crystal the only term that causes the intensity of the nuclear peaks to vary with $\vec{\tau}$ is again the Debye-Waller factor.

2.2.4.3 Paramagnetic scattering

The technique of using spin polarised neutron scattering and spin polarisation analysis to separate the paramagnet and ordered state scattering from all other scattering contributions has been described by Moon *et al.* [9] and Schärpf & Capellmann [10]. This technique exploits the dependence of the scattering cross sections on the scattering vector $\vec{\kappa}$ and the quantisation axis *z*. The scattering process depends on some rules and they can be summarized as follows [11]:

- Only those parts of the vector component of the nuclear interaction potential that are perpendicular to quantisation axis, *z*, give rise to nuclear scattering with flip of the neutron spin in the scattering process.

- Only the component of the magnetic interaction potential that is perpendicular to scattering vector, $\vec{\kappa}$, can give rise to magnetic scattering.

- The component of the magnetic interaction potential parallel to z gives rise to non-spin flip magnetic scattering whereas the component perpendicular to z results in neutron spin flip scattering.

As such, both the coherent scattering and isotopic incoherent scattering contributions are entirely non-spin flip scattering contributions. The nuclear spin incoherent scattering gives contributions to both the spin flip and non-spin flip measured cross sections.

Schärpf and Capellmann [10] have given a complete description of the *x-y-z* difference method with polarized neutrons and how this may be used to separate the coherent, spin incoherent and magnetic scattering cross sections in a multi detector instrument, such as D7 at the ILL. Here, the main results of their paper will be described and related to the measurements that will be presented in chapter 3.

The neutron energy transfer during the scattering process is given by eq.2.2.22 and the different types of scattering cross section that contribute to the total observed cross sections are defined by:

$$\frac{\partial^2\sigma_{para}}{\partial\Omega\partial\omega} = \frac{k'}{k}\frac{2}{3}\left(\frac{\gamma r_0}{2}\right)^2 F^2(\vec{\kappa})M(\vec{\kappa},\omega) \qquad (2.2.60)$$

$$\frac{\partial^2\sigma_{inc}^{spin}}{\partial\Omega\partial\omega} = \frac{k'}{k}B^2 S_{inc}(\vec{\kappa},\omega) \qquad (2.2.61)$$

$$\frac{\partial^2\sigma_{inc}^{isotop}}{\partial\Omega\partial\omega} = \frac{k'}{k}\left(\overline{b^2} - \overline{b}^2\right)S_{inc}(\vec{\kappa},\omega) \qquad (2.2.62)$$

$$\frac{\partial^2\sigma_{coh}}{\partial\Omega\partial\omega} = \frac{k'}{k}\left|\overline{b}\right|^2 S_{coh}(\vec{\kappa},\omega) \qquad (2.2.63)$$

where $M(\kappa,\omega)$ is the Fourier transform of the spatial magnetisation density and B is the dipole magnetic field of the neutron.

The equations above represent the magnetic scattering, the nuclear spin incoherent scattering, the isotope incoherent scattering and the coherent scattering respectively. Implicit in the derivation of these results is that there are no correlations between the nuclear spin and the electron magnetic moments, there is no nuclear polarisation, no nuclear magnetic interference term and only an on site correlation between nuclear spins [10].

For a spectrometer such as D7 for which the scattering vector is defined to lie in the x-y plane, Schärpf and Capellmann [10] show that for a powder sample, the measurement of the spin flip (sf) and non-spin flip (nsf) scattering with the incident neutron spin polarisation alternatively in the x-y-z directions yields the following experimental cross sections:

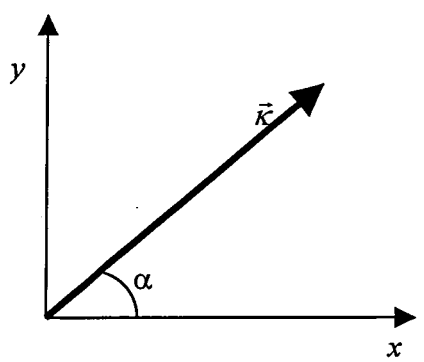

Figure 2.2.2: Scattering geometry of D7

$$\left(\frac{\partial^2\sigma}{\partial\Omega\partial\omega}\right)_x^{sf} = \frac{1}{2}\frac{\partial\sigma_{para}}{\partial\Omega\partial\omega}\left(1+\cos^2\alpha\right)+\frac{2}{3}\frac{\partial^2\sigma_{inc}^{spin}}{\partial\Omega\partial\omega}$$

$$\left(\frac{\partial^2\sigma}{\partial\Omega\partial\omega}\right)_y^{sf} = \frac{1}{2}\frac{\partial\sigma_{para}}{\partial\Omega\partial\omega}\left(1+\sin^2\alpha\right)+\frac{2}{3}\frac{\partial^2\sigma_{inc}^{spin}}{\partial\Omega\partial\omega}$$

$$\left(\frac{\partial^2\sigma}{\partial\Omega\partial\omega}\right)_z^{sf} = \frac{1}{2}\frac{\partial\sigma_{para}}{\partial\Omega\partial\omega}+\frac{2}{3}\frac{\partial^2\sigma_{inc}^{spin}}{\partial\Omega\partial\omega}$$

$$\left(\frac{\partial^2\sigma}{\partial\Omega\partial\omega}\right)_x^{nsf} = \frac{1}{2}\frac{\partial\sigma_{para}}{\partial\Omega\partial\omega}\sin^2\alpha+\frac{1}{3}\frac{\partial^2\sigma_{inc}^{spin}}{\partial\Omega\partial\omega}+\frac{\partial^2\sigma_{coh}}{\partial\Omega\partial\omega}+\frac{\partial^2\sigma_{inc}^{isotop}}{\partial\Omega\partial\omega} \qquad (2.2.64)$$

$$\left(\frac{\partial^2\sigma}{\partial\Omega\partial\omega}\right)_y^{nsf} = \frac{1}{2}\frac{\partial\sigma_{para}}{\partial\Omega\partial\omega}\cos^2\alpha+\frac{1}{3}\frac{\partial^2\sigma_{inc}^{spin}}{\partial\Omega\partial\omega}+\frac{\partial^2\sigma_{coh}}{\partial\Omega\partial\omega}+\frac{\partial^2\sigma_{inc}^{isotop}}{\partial\Omega\partial\omega}$$

$$\left(\frac{\partial^2\sigma}{\partial\Omega\partial\omega}\right)_z^{nsf} = \frac{1}{2}\frac{\partial\sigma_{para}}{\partial\Omega\partial\omega}+\frac{1}{3}\frac{\partial^2\sigma_{inc}^{spin}}{\partial\Omega\partial\omega}+\frac{\partial^2\sigma_{coh}}{\partial\Omega\partial\omega}+\frac{\partial^2\sigma_{inc}^{isotop}}{\partial\Omega\partial\omega}$$

Figure 2.2.2 presents the scattering geometry of the instrument D7 at the ILL. α presents the angle between the scattering vector $\vec{\kappa}$ and the x direction. By combining these measured cross sections it is possible to separate the different scattering contributions from one another. It may be easily verified from eq.2.2.64 that the following combination of measured cross sections gives directly the paramagnetic or ordered state scattering cross section,

$$\left(\frac{\partial^2\sigma_{para}}{\partial\Omega\partial\omega}\right)^{sf} = 2\left[\left(\frac{\partial^2\sigma}{\partial\Omega\partial\omega}\right)_x^{sf}+\left(\frac{\partial^2\sigma}{\partial\Omega\partial\omega}\right)_y^{sf}-2\left(\frac{\partial^2\sigma}{\partial\Omega\partial\omega}\right)_z^{sf}\right] \qquad (2.2.65)$$

and similarly

$$\left(\frac{\partial^2\sigma_{para}}{\partial\Omega\partial\omega}\right)^{nsf} = 2\left[2\left(\frac{\partial^2\sigma}{\partial\Omega\partial\omega}\right)_z^{nsf}-\left(\frac{\partial^2\sigma}{\partial\Omega\partial\omega}\right)_x^{nsf}-\left(\frac{\partial^2\sigma}{\partial\Omega\partial\omega}\right)_y^{nsf}\right] \qquad (2.2.66)$$

Furthermore, one can obtain the nuclear spin incoherent scattering cross section by

$$\frac{\partial^2\sigma_{inc}^{spin}}{\partial\Omega\partial\omega}=\frac{3}{2}\left[3\left(\frac{\partial^2\sigma}{\partial\Omega\partial\omega}\right)_z^{sf}-\left(\frac{\partial^2\sigma}{\partial\Omega\partial\omega}\right)_x^{sf}-\left(\frac{\partial^2\sigma}{\partial\Omega\partial\omega}\right)_y^{sf}\right] \qquad (2.2.67)$$

and subtracting the cross section obtained in this way in eq. 2.2.65 and 2.2.66 from the measured cross section $\left(\frac{\partial^2\sigma}{\partial\Omega\partial\omega}\right)_z^{nsf}$ gives

$$\frac{\partial^2\sigma_{coh}}{\partial\Omega\partial\omega}+\frac{\partial^2\sigma_{inc}^{isotop}}{\partial\Omega\partial\omega}=\left(\frac{\partial^2\sigma}{\partial\Omega\partial\omega}\right)_z^{nsf}-\frac{1}{2}\frac{\partial^2\sigma_{para}}{\partial\Omega\partial\omega}-\frac{1}{3}\frac{\partial^2\sigma_{inc}^{spin}}{\partial\Omega\partial\omega} \qquad (2.2.68)$$

It is not possible to distinguish the coherent scattering from the isotope incoherent scattering. It is stressed that x-y-z difference technique allows the unambiguous separation of the individual contributions to the total scattering. σ_{para}, σ_{inc}^{spin} and σ_{coh} are obtained solely by combination of the observed scattering cross sections as shown in equations 2.60, 2.61, 2.62, and, 2.63.

2.3 Magnetism

2.3.1 The Origin of Atomic Moments

a) Spin and orbit states of electrons

The elementary quantum-mechanical treatment of isolated atoms by means of the Schrödinger equation has led to information on the energy levels that can be occupied by the electrons. The states are characterized by four quantum numbers. These are *principal quantum number, n, orbital angular quantum momentum number, l, magnetic quantum number, m_l, and, spin quantum number, m_s.* The principal quantum number, can take the values from 1 to ∞, l can take the values from 0 to n-1 and m_l may alter between $-l$ and $+l$. The spin quantum number has only two values for each electron and it is either +½ or –½ which are refers to spin up and spin down.

According to Pauli's principle it is not possible for two electrons to occupy the same state. That is, the states of two electrons are characterised by different sets of quantum numbers n, l, m_l and m_s. The maximum number of electrons occupying a given shell is therefore

$$2\sum_{l=0}^{n-1}(2l+1)=2n^2 \qquad (2.3.1)$$

For a given value of l, the angular momentum of an electron due to its orbital motion equals $\hbar\sqrt{l(l+1)}$. For instance, for a d electronic like in ruthenium the permissible values of the angular momentum along a field direction are $2\hbar,\hbar,0,-\hbar,-2\hbar$ (fig 2.3.1). On the other hand the allowed values of spin quantum number, m_s are $\pm\hbar/2$, where plus stands for spin us states and minus for spin down states.

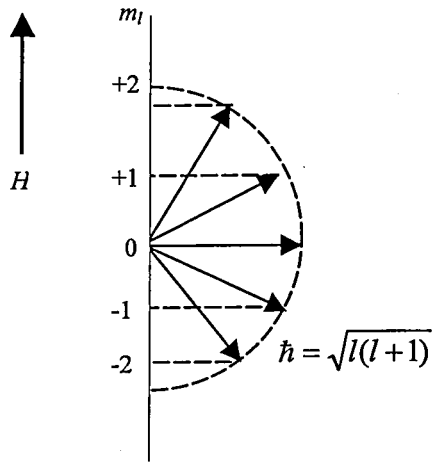

Figure 2.3.1 Vector model of the atom applied to the situation l=2 and nonzero external field.

The moving electron can basically be considered as a current flowing along the electron orbit. An electron with an orbital angular momentum $\hbar l$ has an associated magnetic moment

$$\vec{\mu}_l = -\frac{|e|}{2m}\hbar\vec{l} = -\mu_B\vec{l} \tag{2.3.2}$$

where μ_B is the Bohr magneton. The absolute value of the magnetic moment is given by

$$|\vec{\mu}_l| = \mu_B\sqrt{l(l+1)} \tag{2.3.3}$$

Its projection onto the direction of the applied field is

$$\mu_{lz} = -m_l\mu_B \tag{2.3.4}$$

The situation is different for the spin angular momentum. In this case, the associated magnetic moment is

$$\vec{\mu}_s = -g_e \frac{|e|}{2m} \hbar \vec{s} = -g_e \mu_B \vec{s} \tag{2.3.5}$$

where $g_e = |2.002|$ is the spectroscopic splitting factor (or the *g*-factor for the free electron). The component in field direction is

$$\vec{\mu}_{sz} = -g_e m_s \mu_B \tag{2.3.6}$$

The energy of a magnetic moment $\vec{\mu}$ in a magnetic field $\vec{H}$ is given by the Hamiltonian

$$H = \mu_0 \vec{\mu} \cdot \vec{H} = \vec{\mu} \cdot \vec{B} \tag{2.3.7}$$

where $\vec{B}$ is the flux density or the magnetic induction and $\mu_0 = 4\pi \times 10^{-7}\,\mathrm{Hm^{-1}}$ is the permeability of vacuum. The lowest energy E_0, the ground-state energy, is reached for $\vec{\mu}$ and $\vec{H}$ parallel. Using (2.3.6) and m_s=-1/2, one finds for one single electron

$$E_0 = -\mu_0 \vec{\mu}_{sz} H = +g_e m_s \mu_{0\mu_B} H = -\tfrac{1}{2} g_e \mu_0 \mu_B H \tag{2.3.8}$$

b) Vector model of atoms

The orbital and spin motions of the electrons and interactions between them have to be considered when describing the atomic origin of magnetism. The total orbital angular momentum of a given atom is defined as

$$\vec{L} = \sum_i \vec{l}_i \tag{2.3.9}$$

where the summation extends over all electrons. The summation over a complete shell is zero, the only contributions coming from incomplete shells. The same arguments apply to the total spin angular momentum, defined as:

$$\vec{S} = \sum_i \vec{s}_i \qquad (2.3.10)$$

The resultants $\vec{S}$ and $\vec{L}$ thus formed are coupled through the spin-orbit interaction to form the resultant total angular momentum $\vec{J}$.

$$\vec{J} = \vec{L} + \vec{S} \qquad (2.3.11)$$

This type of coupling is referred to as *Russell-Saunders* coupling. It has been proven to be applicable to most heavy magnetic atoms. *J* can assume values ranging from *J=(L-S), (L-S+1),* to *(L+S-1), (L+S)*. Such a group of levels is called a *multiplet.* The level lowest in energy is called *ground-state multiplet level.* The splitting into different kinds of multiplet levels occurs because the angular momenta $\vec{L}$ and $\vec{S}$ interact with each other via the spin-orbit interaction with interaction energy $\lambda\vec{L}\cdot\vec{S}$ (λ is the spin-orbit coupling constant). Owing to this interaction, the vector $\vec{L}$ and $\vec{S}$ exert a torque on each other which causes them to precess around the constant vector $\vec{J}$. This leads to a situation as shown the figure 2.3.2, where the dipole moments $\vec{\mu}_L = -\mu_B\vec{L}$ and $\vec{\mu}_S = -g_e\mu_B\vec{S}$, corresponding to the orbital and spin momentum, also precess around the total momentum $\vec{\mu}_{tot} = \vec{\mu}_L + \vec{\mu}_S$ which is not collinear with $\vec{J}$ but is tilted towards the spin owing to its larger gyromagnetic ratio. It may be seen from figure 2.3.2 that the vector $\vec{\mu}_{tot}$ makes an angle θ with $\vec{J}$ and also precesses around $\vec{J}$. The precession frequency is usually quite high so that only the components of $\vec{\mu}_{tot}$ along $\vec{J}$ is observed, while the other components average to zero. The magnetic properties are therefore determined by the quantity

$$\vec{\mu} = \vec{\mu}_{tot} \cos\theta = -g_J \mu_B J \tag{2.3.12}$$

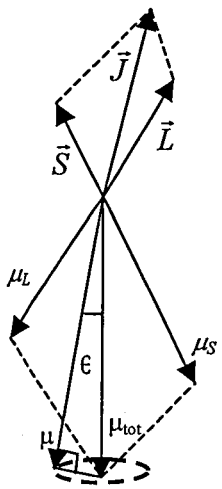

Figure 2.3.2: Spin-orbit interaction between the angular momenta $\vec{S}$ *and* $\vec{L}$

It can be shown that [12, 13]

$$g_J = 1 + \frac{J(J+1) + S(S+1) - L(L+1)}{2J(J+1)} \tag{2.3.13}$$

This factor is called the *Landé spectroscopic g-factor* and has the value 2 when L=0 and 1 when S=0.

For a given atom, one usually knows the ionisation state i.e. the number of electrons residing on an incomplete electron shell, the latter being specified by its quantum numbers. Then *Hund's rules* [12, 14] predict the values of L, S and J for the free atom in its ground-state.

2.3.2 Magnetic Ordering

2.3.2.1 Paramagnetism of free ions

a) The Brillouin function

Once the vector model and Hund's rules have been applied to find the quantum numbers J, L and S of the ground-state multiplet of a given type of atom, the magnetic properties of a system of such atoms can be described based on these quantum numbers and the number of atoms N contained in the system.

If the quantization axis is chosen in the z-direction the z-component m of J for each atom may adopt $2J+1$ values ranging from $m=-J$ to $m=+J$. When a magnetic field B_0 is applied, the energy depends on the occupation of the $(2J+1)$ sub-levels, all of which differ in their m_J value. The magnetic energy of a noninteracting magnetic atom is given by eq.2.3.8.

Most of the magnetic properties of different types of materials depend on how this level scheme is occupied under various experimental conditions. At zero temperature, the situation is comparatively simple because for any of the N participating atoms only the lowest level will be occupied. In this case, the magnetisation of the system is:

$$M = -Ng_J m\mu_B = Ng_J J\mu_B \qquad (2.3.14)$$

However, at finite temperatures, higher lying levels will become occupied. The extent to which this happens depends on the temperature but also the energy separation between the ground-state level and the excited levels, that is, on the magnetic field strength.

The relative population of the levels at a given temperature T and given field strength H can be determined by assuming a Boltzmann distribution for which the probability p_i of finding an atom in a state with energy E_i is given by

$$p_i = \frac{e^{-E_i/kT}}{\sum_i e^{-E_i/kT}} \tag{2.3.15}$$

The magnetisation M of the system can be found from the statistical average $\langle \mu_z \rangle$ of the magnetic moment $\mu_z = -g_J\, m\mu_B$. This statistical average is obtained by weighing the magnetic moment μ_z of each state by the probability that this state is occupied and summing over all states:

$$M = N\langle \mu_z \rangle = N \frac{\sum_{m=-J}^{J} g_J m\mu_B e^{-g_J m\mu_0 \mu_B H/kT}}{\sum_{m=-J}^{J} e^{-g_J m\mu_0 \mu_B H/kT}} \tag{2.3.16}$$

By substituting $x = -g_j\mu_B\mu_0 H/kT$ and using the relations $d\ln(x) = x^{-1}$ and $de^{mx} = me^{mx}dx$,

$$M = Ng\mu_B \frac{d}{dx}\left(\ln \sum_{m=-J}^{J} e^{mx}\right) \tag{2.3.17}$$

Since there will not be any confusion with g_e henceforth the subscript J will be dropped from g_J.

From the standard expression for the sum of a geometric series,

$$\sum_{m=-J}^{J} e^{mx} = e^{-Jx}(1 + e^{x} + e^{2x} + \ldots + e^{2Jx}) = e^{-Jx}\frac{e^{(2J+1)x} - 1}{e^{x} - 1} \tag{2.3.18}$$

Substitution of this result into eq 2.3.17

$$M = Ng\mu_B \frac{d}{dx}\left(\ln\frac{e^{(J+1)x} - e^{-Jx}}{e^x - 1}\right) = Ng\mu_B \frac{d}{dx}\left(\ln\frac{e^{(J+\frac{1}{2})x} - e^{-(J+\frac{1}{2})x}}{e^{\frac{1}{2}x} - e^{-\frac{1}{2}x}}\right) \qquad (2.3.19)$$

Since $\sinh x = (e^x - e^{-x})/2$,

$$M = Ng\mu_B \frac{d}{dx}\left(\ln\frac{\sinh\left(J+\frac{1}{2}\right)x}{\sinh\frac{1}{2}x}\right) \qquad (2.3.20)$$

After carrying out the differentiation

$$M = Ng\mu_B J B_J(y) \qquad (2.3.21)$$

with $B_J(y)$, the so-called *Brillouin function*, being given by

$$B_J(y) = \frac{2J+1}{2J}\coth\frac{(2J+1)y}{2J} - \frac{1}{2J}\coth\frac{y}{2J} \qquad (2.3.22)$$

with

$$y = \frac{gJ\mu_B\mu_0 H}{kT} \qquad (2.3.23)$$

In this expression H is the field responsible for the level splitting of the $2J+1$ fold degenerate ground-state manifold. In most cases H is an external field. Expression 2.3.21 makes it possible to calculate the magnetisation for a system of N non-interacting atoms with quantum number J at various combinations of applied field and temperature.

b) The Curie law

Expression (2.3.21) becomes much simpler in the paramagnetic phase under the condition of small y. The paramagnetic susceptibility is related to the initial slope of the Brillouin function.

When $y \langle\langle 1$, it is justified to use only the first term of the series expansion of $B_J(y)$ for small values of y

$$B_J(y) = \frac{J+1}{3J} y - \frac{[(J+1)^2 + J^2](J+1)}{90J^3} y^3 + \ldots \qquad (2.3.24)$$

From this follows, keeping only the first term,

$$M = Ng\mu_B J B_J(y) = Ng\mu_B J \cdot \frac{J+1}{3J} \cdot \frac{Jg\mu_B \mu_0 H}{kT} = \frac{N\mu_0 g^2 J(J+1)\mu_B^2 H}{3kT} \qquad (2.3.25)$$

The magnetic susceptibility is defined as $\chi = M/H$. Using equation (2.3.25) the magnetic susceptibility can be derived as

$$\chi = \frac{N\mu_0 g^2 J(J+1)\mu_B^2}{3kT} = \frac{C}{T} \qquad (2.3.26)$$

The Curie constant C is given by

$$C = \frac{N\mu_0 g^2 J(J+1)\mu_B^2}{3k} \qquad (2.3.27)$$

The relationship in eq.2.3.26 is known as the *Curie law*. Curie's law states that if the reciprocal values of the magnetic susceptibility, measured at various temperatures, are plotted versus the corresponding temperatures, a line which passed through the origin will

be found. From the slope of this line the Curie constant C can be obtained and hence a value for the effective moment.

$$\mu_{eff} = g\sqrt{J(J+1)}\mu_B \qquad (2.3.28)$$

In general, it may be stated that the Curie law $\chi=C/T$, as expressed in eq.2.3.26, is a consequence of the fact that the thermal average calculating eq.2.3.15 involves only the $2J+1$ equally spaced levels originating from the effect of the applied field on one multiplet level. When more than $2J+1$ levels are involved, or when these levels are no longer equally spaced deviations from Curie behaviour can occur. The latter situation occurs when electrostatic fields in the solid, the crystal field, come into play. It will be shown in section 2.3.4 how crystal fields can also lift the degeneracy of the $2J+1$ ground-state manifold. The combined action of crystal fields and magnetic fields generally leads to a splitting of this manifold such that the $2J+1$ sublevels are no longer equally spaced, or to a spitting where the level with $m=-J$ is not the lowest level in moderate magnetic fields.

2.3.2.2 The magnetically ordered state

a) The Heisenberg exchange interaction and the Weiss field

All of the atomic moments of a system with N atoms will become aligned parallel if the conditions of temperature and applied field are such that for all of the participating magnetic atoms only the lowest is occupied. The magnetisation of the system is then said to be saturated, no higher value being possible than

$$M_S = Ng\mu_B J \qquad (2.3.29)$$

The parallel alignment of moments is reached only in very high applied fields and at fairly low temperatures. A substance, for which a high magnetisation is observed without the application of a magnetic field is called *ferromagnetic* and it is characterised by a

spontaneous magnetisation. This spontaneous magnetisation vanishes at temperatures higher than the *Curie temperature*, T_C. Below T_C, the material is said to be ferromagnetically ordered.

On the basis of the understanding of the magnetisation in terms of the level splitting and level population (Eq 2.3.15), the occurrence of a spontaneous magnetisation would be compatible with the presence of a huge internal magnetic field, H_m. This internal field should be able to produce a level splitting of sufficient magnitude so that practically only the lowest level m=-J is populated. In 1928, Heisenberg [13] has shown that such an internal field may arise as the result of a quantum mechanical exchange interactions between atomic spins. The Heisenberg exchange Hamiltonian is usually written in the form

$$H_{exch} = -\sum_{i,j} J_{ij} \vec{S}_i \cdot \vec{S}_j \qquad (2.3.30)$$

where the summation extends over all spin pairs in the crystal lattice. The exchange constant J_{ij} depends, amongst other things, on the distance between the two atoms i and j.

In most cases, it is sufficient to consider only the exchange interaction between spins on nearest neighbour atoms. If there are Z magnetic nearest neighbour atoms surrounding a given magnetic atom,

$$H_{exch} = -ZJ_{nn} \vec{S}_n \cdot \left\langle \vec{S}_m \right\rangle \qquad (2.3.31)$$

with $\left\langle \vec{S} \right\rangle$ the average spin of the nearest neighbour atoms. Relation 2.3.31 can be rewritten by using $\vec{S} = (g-1)\vec{J}$, which follows from the relation $g\vec{J} = \vec{L} + 2\vec{S}$ and $\vec{J} = \vec{L} + \vec{S}$:

$$H_{exch} = -ZJ_{nn}(g-1)^2 \vec{J} \cdot \langle \vec{J} \rangle \tag{2.3.32}$$

Since the atomic moment is related to the angular momentum by $\vec{\mu} = -g_J \mu_B \vec{J}$ (eq 2.3.12)

$$H_{exch} = \frac{-ZJ_{nn}(g-1)^2 \vec{\mu} \cdot \langle \vec{\mu} \rangle}{g^2 \mu_B^2} = -\mu_0 \vec{\mu} \cdot \vec{H}_m \tag{2.3.33}$$

where

$$\vec{H}_m = \frac{-ZJ_{nn}(g-1)^2 \langle \vec{\mu} \rangle}{g^2 \mu_B^2} \tag{2.3.34}$$

can be regarded as an effective internal field, the so-called *molecular field*, produced by the average moment $\langle \vec{\mu} \rangle$ of the Z nearest-neighbour atoms.

Since $\vec{M} = N\langle \vec{\mu} \rangle$, it follows that $\vec{H}_m$ is proportional to the magnetization

$$\vec{H}_m = N_W \vec{M} \tag{2.3.35}$$

The constant N_W is called molecular-field constant or the Weiss-field constant.

The exchange interaction between two neighbouring spin moments introduced in eq. 2.3.31 has the same origin as the exchange interaction between two electrons on the same atom, where it can lead to parallel and antiparallel spin states, the exchange interaction between two neighbouring spin moments arises as a consequence of the overlap between the electronic orbitals of two adjacent atoms.

b) Ferromagnetism

A ferromagnetic sample is usually divided up into domains that are spontaneously magnetised. Applied magnetic fields can change the direction of the magnetisation within the domains. Except in certain circumstances, the domains make little difference to the magnitude of the atomic magnetisation. The magnetisation within the domain is called the intrinsic magnetisation and its value in zero field is the spontaneous magnetisation. The saturation magnetisation is the value of the spontaneous magnetisation at zero temperature.

A basic explanation of the occurrence of the spontaneous magnetisation was derived from the postulate put forward by Weiss that an intense internal or molecular field (also called Weiss field) exists within the ferromagnetic solid. The magnitude of this field was found to be of the order of 100 T.

The total field experienced by the magnetic moments comprises the applied field H and the molecular field or Weiss field H_m:

$$\vec{H}_{tot} = \vec{H} + \vec{H}_m = \vec{H} + N_W \vec{M} \tag{2.3.36}$$

Firstly, the effect of the presence of the Weiss field $N_W M$ on the magnetic behaviour of a magnetic material above T_C will be investigated. The high-temperature approximation eq. 2.3.25 may be used.

$$M = \frac{C}{T} H \tag{2.3.37}$$

It has to be born in mind, however, that the splitting of the (2J+1)-manifold used to calculate the statistical average $\langle \mu_z \rangle$ is larger owing to the presence of the Weiss field. For a ferromagnet above T_C H_{tot} has to be used instead of H when going through all the steps from eq.2.3.15 to eq.2.3.25. This means that eq.2.3.25 should be written in the form

$$M = \frac{C}{T}(H + N_W M) \tag{2.3.38}$$

Introducing the magnetic susceptibility χ=M/H,

Above their Curie temperature, ferromagnetics become paramagnetic and their susceptibility depends on temperature. The reciprocal of the susceptibility varies with temperature with an intercept on the positive temperature axis at the paramagnetic Curie temperature θ_p, which is usually close to T_C, though the two quantities are rarely exactly equal. This dependence of susceptibility on temperature is of the form [12, 13]:

$$\chi = \frac{C}{T - N_W C} = \frac{C}{T - \theta_p} \tag{2.3.39}$$

where θ_p is called the asymptotic or paramagnetic Curie temperature.

Relation 2.3.39 is known as the *Curie-Weiss* law. It describes the temperature dependence of the magnetic susceptibility for temperatures above T_C. When plotted as a function of T versus the reciprocal susceptibility it is again a straight line. However, this time it does not pass through the origin (as it did for the Curie law) but it intersects the temperature axis at $T=\theta_p$. Plots of χ^{-1} versus T for an ideal Curie paramagnet ($\chi=C/T$) and a ferromagnet material above T_C ($\chi=C/(T-\theta_p)$) are compared with each other in fig 2.3.2.

At $T=\theta_p$, the susceptibility diverges which implies that one may have nonzero magnetisation in zero applied field. This exactly corresponds to the definition of the Curie temperature, being the upper limit for having a spontaneous magnetisation. Therefore, for a ferromagnet, it could be written

$$\theta_p = T_C = N_W C = \frac{N_W N \mu_0 g^2 J(J+1)\mu_B^2}{3k} \tag{2.3.40}$$

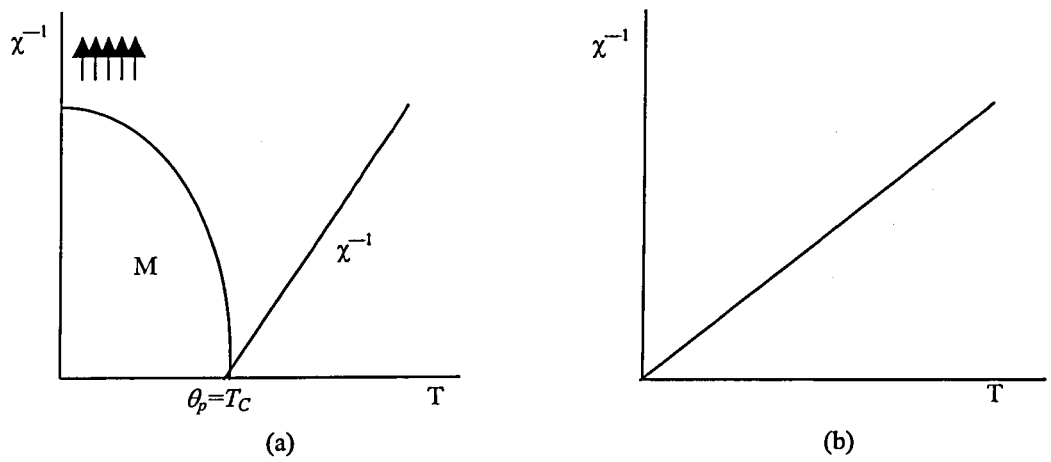

Figure 2.3.3: Temperature depencence of the magnetisation M and the inverse magnetic susceptibility 1/χ a) Ferromagnetism, b) Ideal paramagnetism

This relation offers the possibility to determine the magnitude of the Weiss constant N_W from the experimental value of T_C or θ_p, obtained by plotting the spontaneous magnetisation versus T or plotting the reciprocal susceptibility versus T.

2.3.3 SQUID

A Superconducting Quantum Interference Device, SQUID for short, was used to measure the magnetic properties of $SrRuO_3$, Sr_2RuO_4 and $Sr_{(1-x)}Ca_xRuO_3$. This device is widely accepted as the most accurate method of measuring magnetic moments. The resolution of 10^{-8} e.m.u. (10^{-11} JT^{-1}) allows accurate measurements of samples with small magnetic moments. This highly sensitive method was appropriate for investigating the magnetic properties of $SrRuO_3$. With the data obtained from SQUID measurements and using Arrott plots the spontaneous magnetisation, Curie temperature and the paramagnetic effective Bohr magneton number can be obtained.

The SQUID is a sophisticated analytical instrument configured specifically for the investigation of the magnetic properties of small experimental samples over a broad range of temperature and magnetic fields. The magnetometer consists of a superconducting solenoid, a SQUID detector system, a sample transport mechanism, a

liquid helium Dewar, a temperature control module and an electronic control console which is connected to the computer with the control system software. The superconducting solenoid includes a superconducting magnet, which consists of a multifilament superconducting wire. This magnet provides a reversible field operating to plus or minus 5.5 Tesla using an oscillatory technique to minimize magnet drift immediately following field changes. Together with the temperature control system the whole device provides an actively regulated, precision thermal environment over a temperature range of 1.7K to 400K and an external magnetic field range of -5.5T to 5.5T

Sensing pick-up loops, also consisting of a superconducting wire, are mounted in the solenoid and connected to a signal coil in the SQUID detector system below the solenoid. The SQUID ring is a superconducting wire with a small insulating layer, the "weak link". The flux induced in the signal coil and passing through the ring is quantised once the ring has gone superconducting but the "weak link" forces the flux trapped in the ring to change only by discrete amounts [7]. Quantized changes in the flux occur as a result of tunnelling by electrons through a Josephson junction in the SQUID ring [8, 9]. These quantised changes are used by the instrument to calculate the magnetic moment of the sample.

For measurements of the magnetic moment the sample was placed below the detection loops with the transport set at its lower limit of travel. The sample then rose through the sensing loops while measuring the output of the SQUID detector. The moment was then measured by repeatedly moving the sample upwards in small steps and reading the voltage from the SQUID detector at each position (figure 2.3.4). The final average voltage data is plotted as a function of the sample position as a figure.

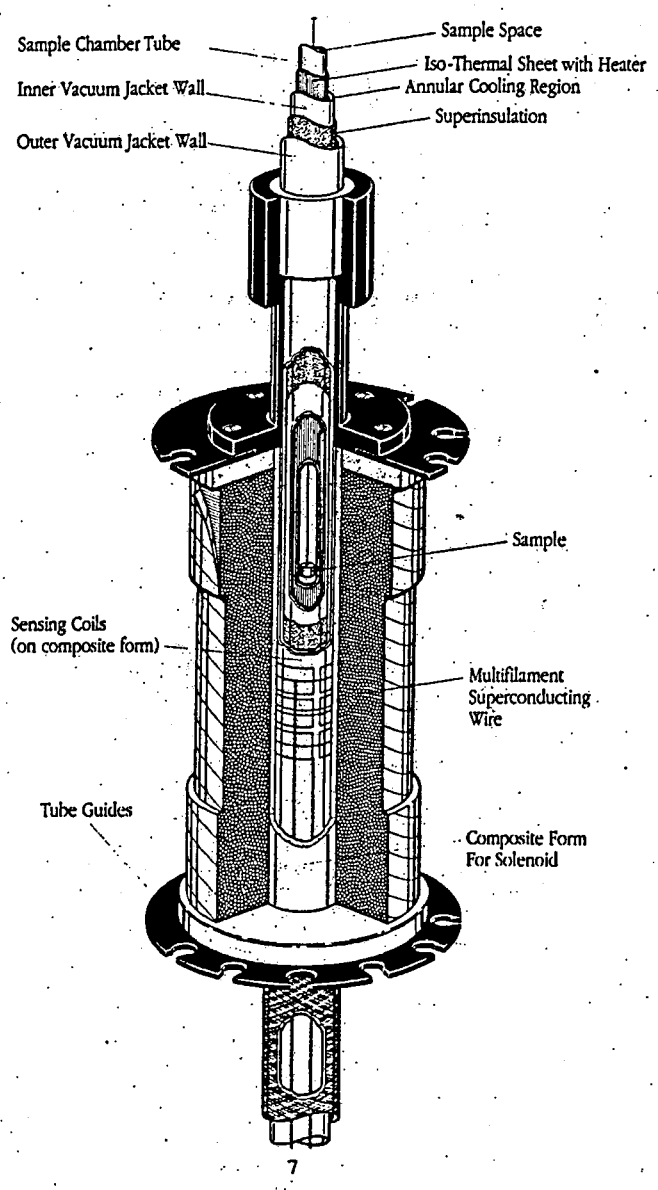

Figure 2.3.4.: Cross section of SQUID device [15]

2.3.3.1 Arrott plots

The basis of Arrott plots is a Landau description of the magnetisation using an expansion of the free energy in powers of the magnetic order parameter, the ferromagnetic moment for a ferromagnet and the staggered magnetisation for an antiferromagnet. The magnetic behaviour may be described using a small number of, possibly temperature dependent, coefficients.

The free energy as a function of the order parameter M and normalised to one magnetic atom is given by

$$F = F_0 + \frac{1}{2}AM^2 + \frac{1}{4}CM^4 - BM \qquad (2.3.41)$$

Here A and C are expansion coefficients. All contributions, which do not depend on the magnetisation, are contained in the term F_0 which will be omitted from all further formulae.

The magnetic moment is obtained by minimisation of the free energy expansion with respect to M.

$$0 = \frac{\partial F}{\partial M} = AM + CM^3 - B \qquad (2.3.42)$$

If eq.2.3.42 is rearranged, one can obtain

$$M^2 = \frac{1}{C}\frac{B}{M} - \frac{A}{C} \qquad (2.3.43)$$

The coefficient C is taken to be temperature independent. It is related to the third order susceptibility. B is the external field and the coefficient A is assumed to be temperature dependent and it is given by

$$A = 3\frac{k_B}{J(J+1)}(T-\theta_P) \qquad (2.3.44)$$

and θ_P is the paramagnetic Curie temperature.

Equation eq.2.3.43 resembles the equation of a straight line. Plotting the magnetisation for a given temperature as a function of field and using units of ratio of applied field divided by observed magnetisation on the x-axis and the square of the magnetisation on the y-axes will yield straight lines with *1/C* as a slope and *–A/C* as the intersection point with the M^2 axis. The intersection point with the x-axis is given by the coefficient A and is directly related to the inverse susceptibility in zero field as can be seen in eq.2.3.44. As discussed above coefficient A is proportional to the temperature and C is temperature independent. As temperature is varied, the lines of the Arrott plots are displaced parallel to each other. The temperature of the isotherm which intersects the origin of the Arrott plot is the ferromagnetic transition temperature $T_C=\theta_P$. For temperatures that are smaller than T_C the straight line cuts the M^2 axis at positive values and gives the value of the spontaneous magnetisation in the absence of a magnetic field. Thus Arrott plots are a more physically transparent and useful tool for the analysis and description of magnetic materials.

2.3.4 Crystal fields

Crystal field (CF) theory is the name given to the model which describes how transition metal ions with d^n configuration are perturbed by their chemical environment. The basic idea is shown in Fig 2.3.5 [16]

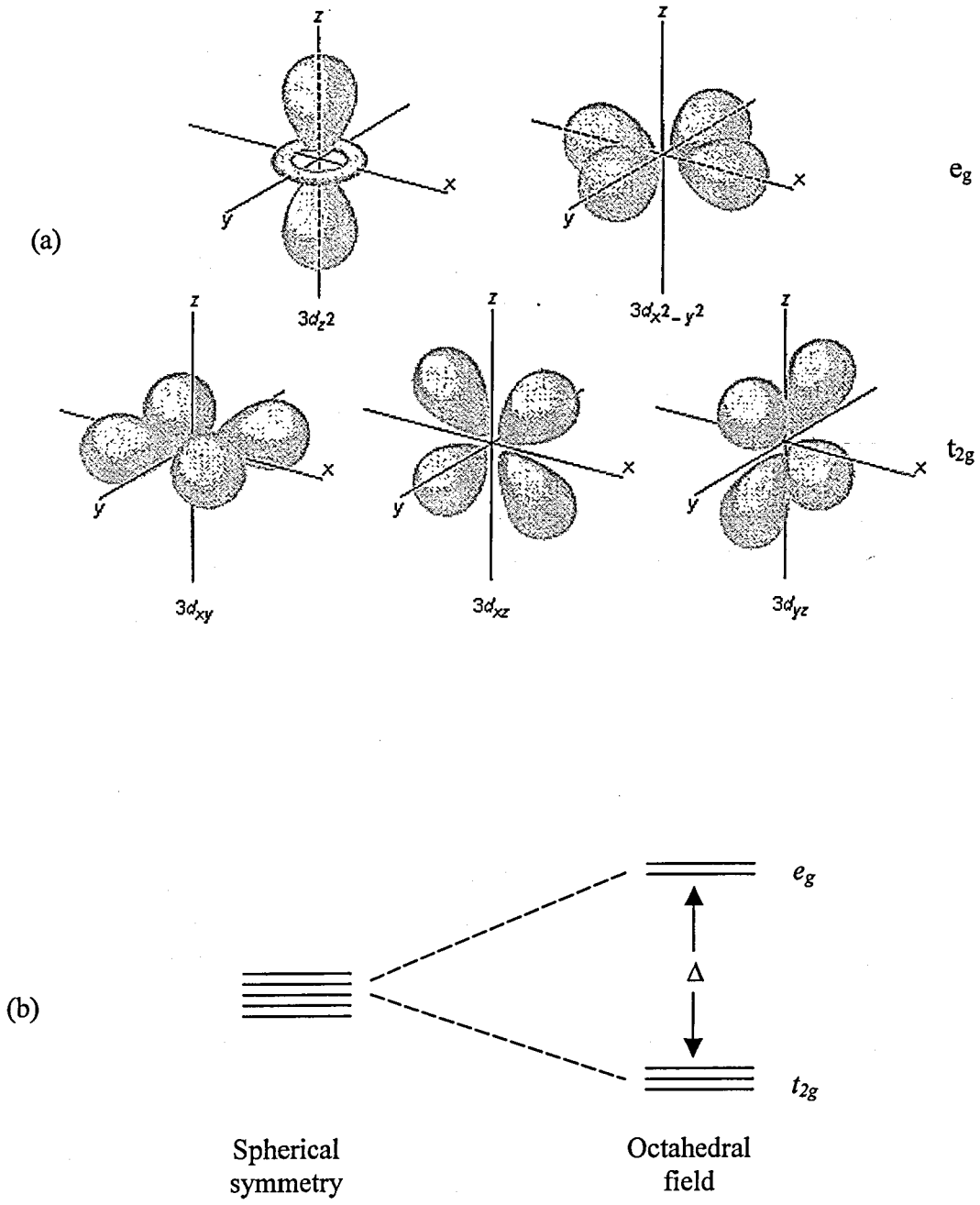

Figure 2.3.5: The d orbitals of a transition metal ion located at a site with octahedral symmetry, showing (a) the different orientation of the e_g and t_{2g} sets, and (b) the resulting orbital energies with the crystal field splitting.

For a transition metal ion like Ru in the $Sr_{(1-x)}Ca_xRuO_3$ or Sr_2RuO_4 compounds with the octahedral coordination, the five *d* orbitals are seen to divide into two sets (figure 2.3.5-

b): two orbitals have lobes of maximum probability pointing directly at the near neighbour oxygens, whereas the other three have nodal planes in these directions. These distinct sets of orbitals are conventionally denoted e_g and t_{2g} respectively, according to their symmetry. Figure 2.3.5-b also shows how the octahedral environment gives rise to a *crystal field splitting* (Δ) between lower lying t_{2g} and higher energy e_g orbitals.

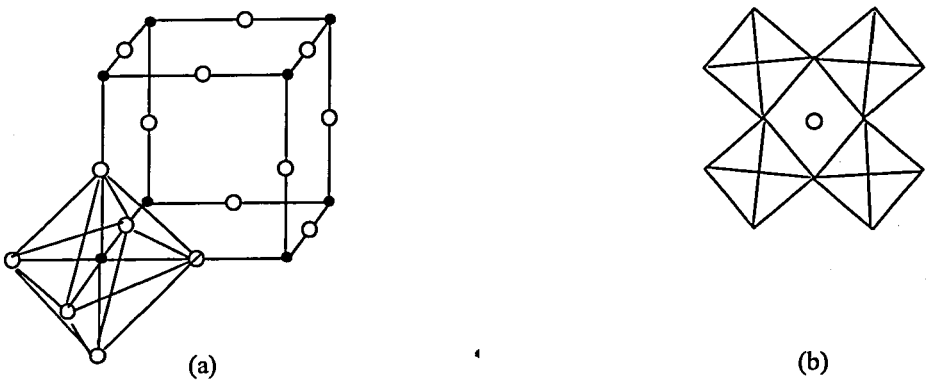

Figure 2.3.6: View of the a)cubic, b) distorted cubic structure of $Sr_{(1-x)}Ca_xRuO_3$ illustrating the RuO_6 octahedra [17, 18]

The electron configurations for ions on octahedral sites are obtained using a CF model by arranging the electrons in the t_{2g} *and* e_g orbitals in accordance with the Pauli Exclusion Principle. The ground state of the free ion satisfies Hund's first rule: i.e. the electrostatic repulsion between electrons is minimised by placing them, as far as possible, with parallel spins into different orbitals. In crystal fields, different possibilities can often arise according to the relative magnitude of the splitting, Δ, and the exchange energy: if the former is large the lowest energy is obtained by complete filling of orbitals from the bottom up, whereas more favourable exchange energies are found with single filling of orbitals so that spins can be parallel. The resulting alternative *low-* and *high-spin* configurations are shown in table 2.3.1. This table shows the term symbol giving the spin and overall symmetry behaviour of the ground state, and the *crystal field stabilisation energy (CFSE)* appropriate to the configuration. The CFSE values represent the stabilisation expected for the particular configuration in the units of the splitting, Δ, and assigned an energy -3/2Δ to the t_{2g} and +3/2Δ to the e_g orbitals.

	High spin			Low spin		
n	Configuration	State	CFSE/Δ	Configuration	State	CFSE/Δ
1	t_{2g}^1	$^2T_{2g}$	2/5	-	-	-
2	t_{2g}^2	$^3T_{1g}$	4/5	-	-	-
3	t_{2g}^3	$^4A_{2g}$	6/5	-	-	-
4	$t_{2g}^3 e_g^1$	^5E_g	3/5	t_{2g}^4	$^3T_{1g}$	8/5
5	$t_{2g}^3 e_g^2$	$^6A_{1g}$	0	t_{2g}^5	$^2T_{2g}$	2
6	$t_{2g}^4 e_g^2$	$^5T_{2g}$	2/5	t_{2g}^6	$^1A_{1g}$	12/5
7	$t_{2g}^5 e_g^2$	$^4T_{1g}$	4/5	$t_{2g}^6 e_g^1$	^2E_g	9/5
8	$t_{2g}^6 e_g^2$	$^3A_{2g}$	6/5	-	-	-
9	$t_{2g}^6 e_g^3$	^2E_g	3/5	-	-	-
10	$t_{2g}^6 e_g^4$	$^1A_{1g}$	0	-	-	-

Table 2.3.1: High- and low-spin states for d^n ions on octahedral sites.
n=4 in a low spin state represents the value of Ru^4

Certain electron configurations have a notable tendency to occupy distorted environments. d^4 (high spin) and d^9 ions in non-metallic solids invariably seem to give a tetragonal distortion of an otherwise octahedral site, with two lengthened M-O bonds, or occasionally a square planar coordination. The distortion is often regarded as a consequence of the *Jahn-Teller* theorem, according to which a non-linear molecule in an electronic state with orbital degeneracy will distort so as to lower its symmetry and remove the degeneracy.

There are two types of Jahn-Teller effects. The spontaneous Jahn-Teller effect is the spontaneous distortion of the lattice geometry (fig 2.3.6-b) in an electronically excited state which results when levels are split to reduce the energy of the overall system. The other Jahn-Teller effect is the static Jahn-Teller effect. The static Jahn-Teller effect occurs if the lowest energy level is degenerate, in which case the lattice will distort spontaneously so as remove the degeneracy and make one energy level more stable comparing to the other [19].

References

[1] Woolfson, M. M., *An Introduction to X-ray Crystallography,* Cambridge Univ. Press, (1974)

[2] Ladd, M., Palmer, R., *Structure determinations by X-ray Crystallography,* Kluwer Academic / Plenum Publishers, (2003)

[3] Ashcroft, N. W., Mermin, M. D., *Solid State Physics,* Saunders College Publishing, (1976)

[4] Kittel, C., *Introduction to Solid State Physics,* John Wiley and Sons, (1996)

[5] Lovesey, S. W., *Theory of Neutron Scattering from Condensed Matters, Vol.1,* Clarendon Press, Oxford, (1984)

[6] Squires, G. L., *Introduction to the Theory of Thermal Neutron Scattering,* Cambridge Univ. Press, (1978)

[7] Smith, T. J., *PhD Thesis,* Loughborough Univ., (1999)

[8] Bacon, G. E., *Neutron Diffraction,* Clarendon Press, Oxford, (1962)

[9] Moon, R. M., Riste, T., Koehler, W. C., *Phys. Rev.,* **181**, 920, (1969)

[10] Schärpf, O., Capellmann, H., *Phys. Stat. Sol., (a)* **135**, 359, (1993)

[11] Murphy, H. M., *PhD Thesis,* Loughborough Univ., (1993)

[12] Crangle, J., *Solid State Magnetism,* Edward Arnold, (1991)

[13] Bushow, K. H. J., de Boer, F. R., *Physics of Magnetism and Magnetic Materials,* Kluwer Academic / Plenum Publishers, (2003)

[14] Aygün, E., Zengin. M., *Atom ve Molekül Fiziği,* Yüksel Matbaası, Ankara, (1995)

[15] SQUID users guide

[16] Cox, P. A., *Transition Metal Oxides,* Clarendon Press, (1995)

[17] Kiyamata, T., *et al., Phys. Rev., 54,* R756 *(1996)*

[18] Kennedy, B. J., *et al., Phys. Rev., 58,* 653 *(1998)*

[19] Jahn, H. A., Teller, E., *Proc. R. Soc. London A, 161,* 220, (1937).

[20] Guinier, A., *X-ray diffraction in crystals, imperfect crystals, and amorphous bodies*, W.H. Freeman and Company, San Francisco, (1963)

Chapter 3

Experimental Investigations

3.1 Sample Preparation and Characterisation using X-rays

a) Preparation

Ruthenium (IV) Oxide (RuO_2), Strontium Carbonate ($SrCO_3$) and Calcium Carbonate ($CaCO_3$) were the starting material for the compounds which have been investigated for this thesis. Samples of $SrRuO_3$, Sr_2RuO_4, $CaRuO_3$, $Sr_{0.5}Ca_{0.5}RuO_3$ and $Sr_{0.75}Ca_{02.5}RuO_3$ have been prepared. $SrCO_3$ (strontianite or strontium carbonate), $CaCO_3$ (calcium carbonate) and RuO_2 (ruthenium (IV) oxide, hydrate) were bought from Alfa Aesar, Johnsons Matthey PLC, Ochard Road, Royston, Herts., England. All the materials and compounds were stored in evacuated glass containers. All glass containers were mechanically cleaned before preparation.

All $SrRuO_3$, Sr_2RuO_4, $CaRuO_3$, $Sr_{0.5}Ca_{0.5}RuO_3$, $Sr_{0.75}Ca_{0.25}RuO_3$ compounds have been prepared in the Department of Physics at Loughborough University. A characterisation of the atomic structure and sample quality is necessary before starting a more detailed investigation. These investigations have been done by X-ray diffraction experiments in Loughborough University and neutron scattering experiments at the ILL, Grenoble, France.

b) Characterisation

In order to obtain the crystallographic properties, the diffraction patterns are analysed using FullProf [5], a computer program for structure profile refinement. This program refines a calculated diffraction pattern and fits it to the observed spectrum. The refined parameters included:

- Zero point offset
- Overall scale factor
- Lattice parameters
- Atomic positions
- Occupation numbers

- Peak shape parameters, half width parameters for the determination of the width of peaks.

The process of refinement is an iterative one and is done over a number of cycles as defined by the user. The level of agreement between the observed and calculated patterns is evaluate at every point of the powder pattern and expressed by means of a difference plot and by the following agreement factors:

$$R_{Bragg} = \frac{\sum_i \left| I_{O_i} - I_{C_i} \right|}{\sum_i I_{Oi}} \tag{3.1.1}$$

$$R_P = 100 \times \frac{\sum_i \left| y_{O_i} - y_{C_i} \right|}{\sum_i y_{O_i}} \tag{3.1.2}$$

$$R_W = 100 \times \left[\frac{\sum_i w_i (y_{O_i} - y_{C_i})^2}{w_i y_{O_i}^2} \right]^{1/2} \tag{3.1.3}$$

$$R_E = 100 \times \left[\frac{N - P - C}{\sum_i w_i y_{O_i}^2} \right]^{1/2} \tag{3.1.4}$$

These are printed at the end of each cycle. In these expressions, indices *o* stands for observed value, *c* stands for calculated value, and, *i* is the number of data points. *N* is the number of independent observations, *P* is the number of refined parameters, *C* is the number of constraints, y_i is the intensity at angular position θ_i, I is the Bragg intensity and *w* is the statistical weight. R_{Bragg} is the agreement factor based upon observed and calculated integrated Bragg intensities, R_p is the profile agreement factor, R_W is the

weighted profile agreement factor and the R_E expressed theoretical agreement expected from counting statistics alone. The ratio R_W/R_E yields the statistical quantity "*chi* (χ)", a value close to 1 indicates perfect agreement of model calculation and observation. In practise some systematic deviations of the calculated and observed pattern occur. Therefore the χ^2 will be larger. For observed patterns and depending on the complexity of the structure and the number of parameters a $\chi^2 \leq 10$ can be considered very satisfactory.

3.1.1 Preparation and Characterisation of Starting Materials using X-ray Diffraction

$SrCO_3$, $CaCO_3$ and RuO_2 were the starting materials for the preparation of the compounds $SrRuO_3$, $CaRuO_3$, $Sr_{(1-x)}Ca_xRuO_3$ and Sr_2RuO_4.

The RuO_2 obtained commercially was quoted as being Ruthenium Oxide-hydrate. This indicates that it does contain some water. No precise value of the water content was given. Thus, before any further measurements could be made the water had to be removed. For a Ruthenium content of 54%, the water content corresponds to $3xH_2O$ [1]. Figure 3.1.2 shows the X-ray diffraction pattern of Ruthenium Oxide–hydrate in the "purchased" form.

In order to remove the water, the sample was heated in air for 1h at 200°C, then for 24h to 600°C and was subsequently cooled to 100°C within 1 hour. This heat treatment is believed to give rise to the following chemical reaction

$$RuO_2(H_2O)_x \xrightarrow{heat} RuO_2 + X(H_2O)$$

After heating it is observed that the weight loss was approximately 30%. The dried RuO_2 was checked using X-ray diffraction. A refined pattern of RuO_2 at room temperature is shown in figure 3.1.3. The structure agrees with the one proposed in the literature [2]. This agreement can bee seen in figure 3.1.3 and table 3.1.1

The investigations of $SrCO_3$ and $CaCO_3$ indicated that these compounds did not have any appreciable amount of water in it. The diffraction pattern and the subsequent refinements are shown in figure 3.1.5 and table 3.1.3 for $SrCO_3$ and figure 3.1.7 and table 3.1.4 for $CaCO_3$.

In addition an aluminium (Al) holder was used to hold the powders for the X-ray experiments. In order to identify possible contributions arising from the aluminium holder in the X-ray diffraction pattern of the materials investigated, a scan of the empty sample holder was performed. A comparison of sample holder peaks in figure 3.1.1 and diffraction patterns of samples indicates that there are no observed aluminium peaks in the X-ray patterns of any of the samples.

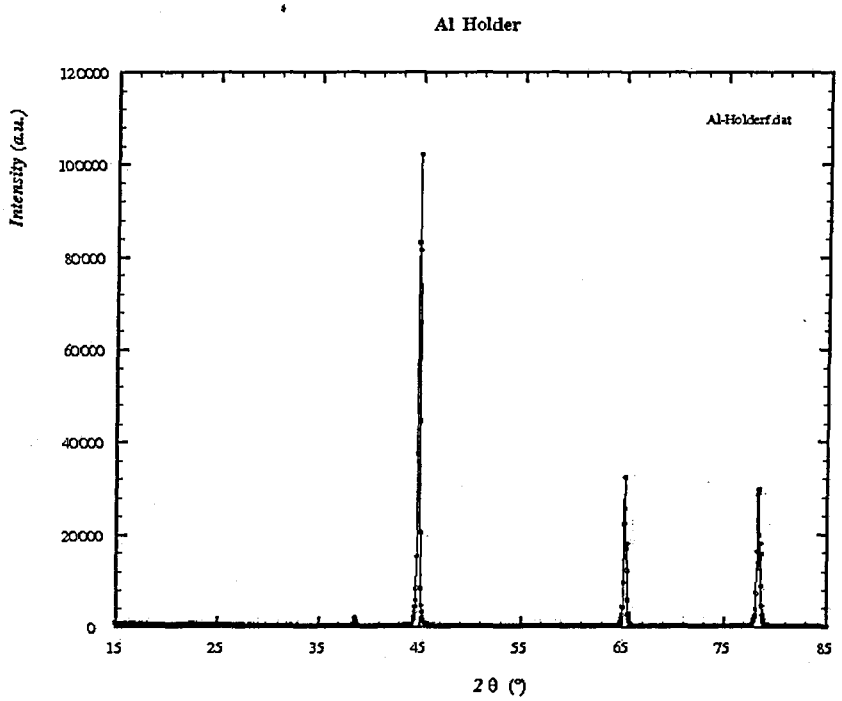

Figure 3.1.1: X-ray diffraction pattern of the Aluminium sample holder

a) RuO_2

RuO_2 belongs to the tetragonal structure type. Its space group is reported to be $P4_2/mnm$ (space group No. 136, [3]), [2, 4]. An X-ray investigation of RuO_2 has been carried out before (figure 3.1.2) and after heat treatment (figure 3.1.3). Table 3.1.1 shows the crystallographic data of reference [2] and the refined data.

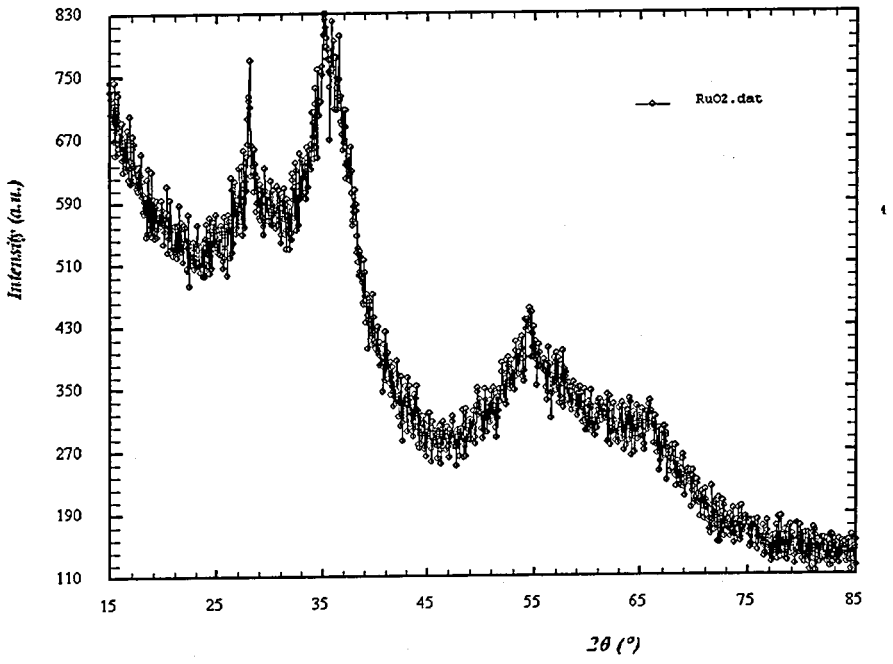

Figure 3.1.2: RuO_2 before heat treatment

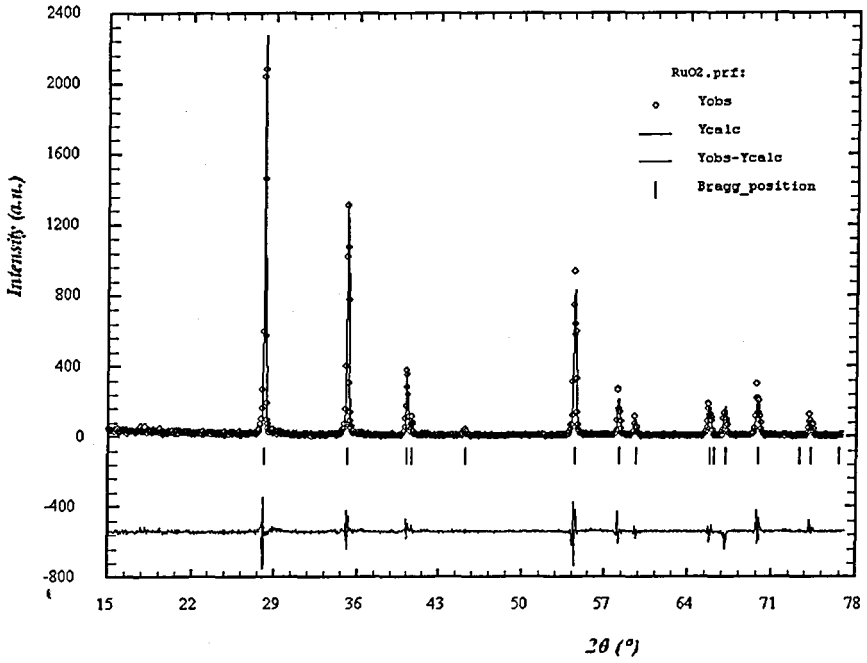

Figure 3.1.3: X-ray observations and fit of RuO_2 after heat treatment

Atom	Wyckoff Notation	Atomic positions for the tetragonal structure of RuO_2 using space group $P4_2/mnm$ [2].			Atomic positions for the tetragonal structure of RuO_2 using space group $P4_2/mnm$ after refinement using FullProf [5]		
		x	y	z	x (z)	y (x)	z (y)
Ru	2a	0	0	0	0	0	0
O	4f	0.305 (2)	0.305 (2)	0	0.307 (4)	0.307 (4)	0
Lattice Parameters					Lattice Parameters		
a (Å)		b (Å)		c (Å)	a (Å)	b (Å)	c (Å)
4.4919 (8)		4.4919 (8)		3.1066 (7)	4.487 (1)	4.487 (1)	3.1044 (6)
χ^2=1.8					χ^2=2.02		

Table 3.1.1: Refined parameters of RuO_2

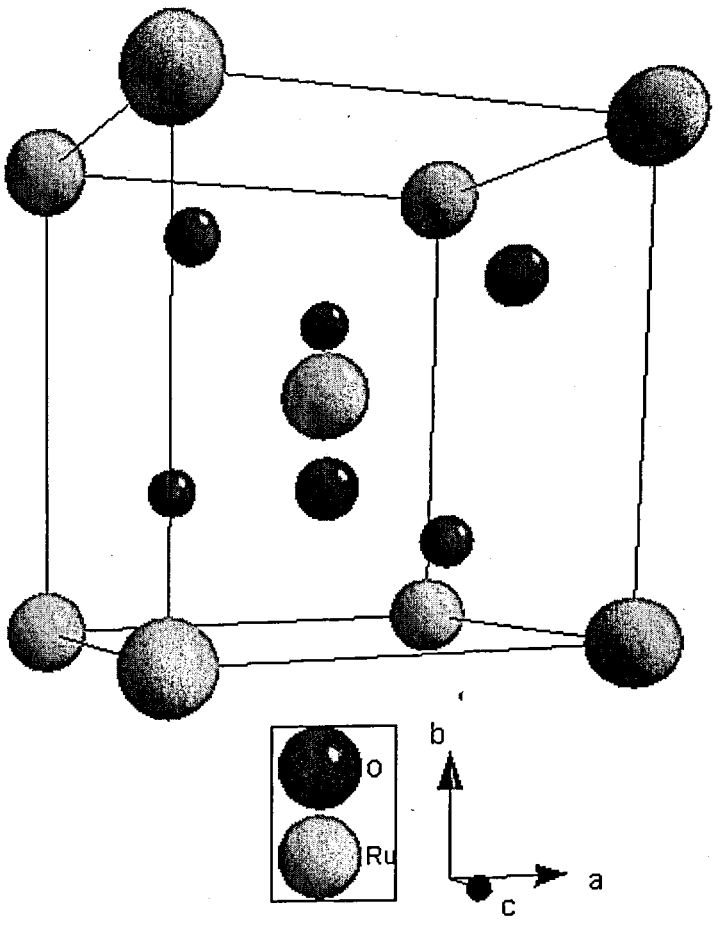

Figure 3.14: The crystallographic structure plot of RuO_2

Table 3.1.1 shows the final refined crystallographic data of RuO_2. The refined model parameters and literature data agree well, with the refinement having a small χ^2 value of 2.02. All the parameters agree within the error bars. This is also an indication for the success of the heat treatment.

b) $SrCO_3$

$SrCO_3$ is also called strontianite or strontium carbonate. It has a perovskite structure, with general formula ABO_3 [6, 7, 8, 9]. It belongs to the orthorhombic structure type of aragonite [10]. The strontianite that was used had a purity of 99.99%. In the literature the space group of $SrCO_3$ is reported to be *Pmcn* [9, 10]. This is an unconventional setting

which is converted to the space group *Pnma* (space group No. 62 of the International Tables of Crystallography [3]) (table 3.1.2).

No. of Space group	Schoenflies symbol	Standard full symbol *a b c*		
			a b c	***b c a***
62	$D_{2h}^{16} = V_h^{16}$	$p\frac{2_1}{n}\frac{2_1}{m}\frac{2_1}{a}$	*Pnma*	*Pmcn*

Table 3.1.2: Three dimensional space-group symbols for various settings [11]

After the conversion, the lattice parameters change as follows:

$$a \rightarrow b \qquad b \rightarrow c \qquad c \rightarrow a$$

The positions of atoms are changed accordingly:

$$x \rightarrow y \qquad y \rightarrow z \qquad z \rightarrow x$$

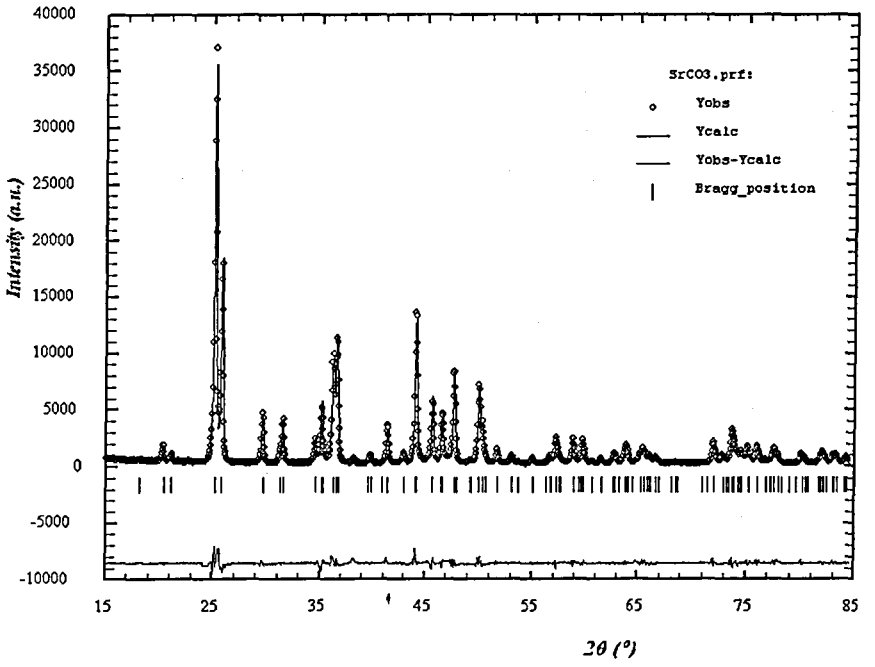

Figure 3.1.5: Observation and fit of the X-ray pattern of $SrCO_3$

Atom	Wyckoff Notation	Atomic positions for the orthorhombic structure of $SrCO_3$ using space group *Pmcn* [9]			Atomic positions for the orthorhombic structure of $SrCO_3$ using space group *Pnma* after conversion and refined with FullProf [5]		
		x	y	z	x (z)	y (x)	z (y)
Sr	4c	¼	0.4160 (1)	0.7569 (3)	0.7562 (5)	¼	0.4161 (2)
C	4c	¼	0.760 (1)	-0.086 (2)	-0.082 (3)	¼	0.728 (2)
O1	4c	¼	0.9119 (9)	-0.95 (2)	-0.91 (2)	¼	0.912 (1)
O2	8d	0.4694 (5)	0.6821 (8)	-0.84 (1)	-0.90 (1)	0.4689 (3)	0.6821 (9)
Lattice Parameters					Lattice Parameters		
a (Å)		b (Å)		c (Å)	a (c) (Å)	b (a) (Å)	c (b) (Å)
5.090 (2)		8.358 (2)		5.997 (4)	6.0251 (5)	5.1039 (5)	8.4158 (7)
$\chi^2 = 1.8$					$\chi^2 = 11.6$		

Table 3.1.3: Atomic positions and lattice parameters from the model and refined parameters of $SrCO_3$ in the space group Pmcn and in Pnma (after conversion from Pmcn to Pmna)

The refined data (figure 3.1.5 and table 3.1.3) are fairly close to the literature data. The χ^2 value of the refinement of 11.6 is larger than the literature χ^2 value. Most of the deviation of the literature model and the refined model parameters are within one error bar, but all values are within 3 times the error bars of the quoted values given. There are no additional peaks observed in the plot. The crystallographic structure can be seen in figure 3.1.6.

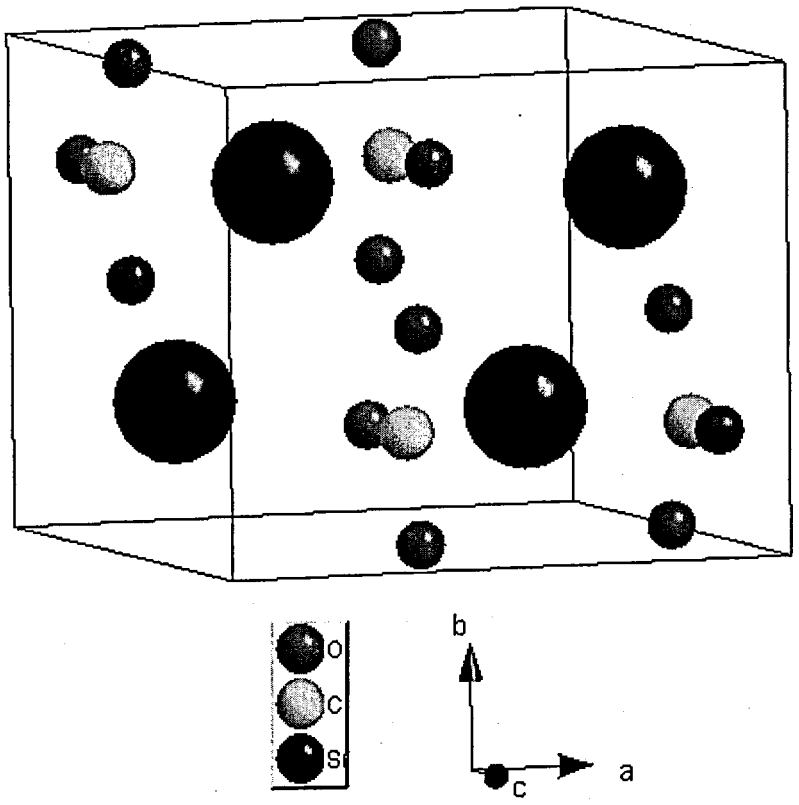

Figure 3.1.6: The crystallographic structure of $SrCO_3$

c) $CaCO_3$

Two different structures are reported for $CaCO_3$. One is the tetragonal structure with space group *Pnma* similar to $SrCO_3$ [9, 10] and the other is a trigonal-rhombohedral structure with space group *R-3c* [9, 24, 25]. Both structures were used to model the X-ray diffraction observed for $CaCO_3$. While the tetragonal structure does not represent the data

well the rhombohedral structure is a good model. Thus, the investigation of the structure of $CaCO_3$ is focused on the rhombohedral structure.

A heat treatment was applied to $CaCO_3$. The weight loss was approximately 44% which indicates that this weight loss is due to a loss of CO_2 gas rather than water. This can be taken as confirmation that the compound is free of water. As a result, the unheated $CaCO_3$ had been used for the preparation of all Ca containing compounds.

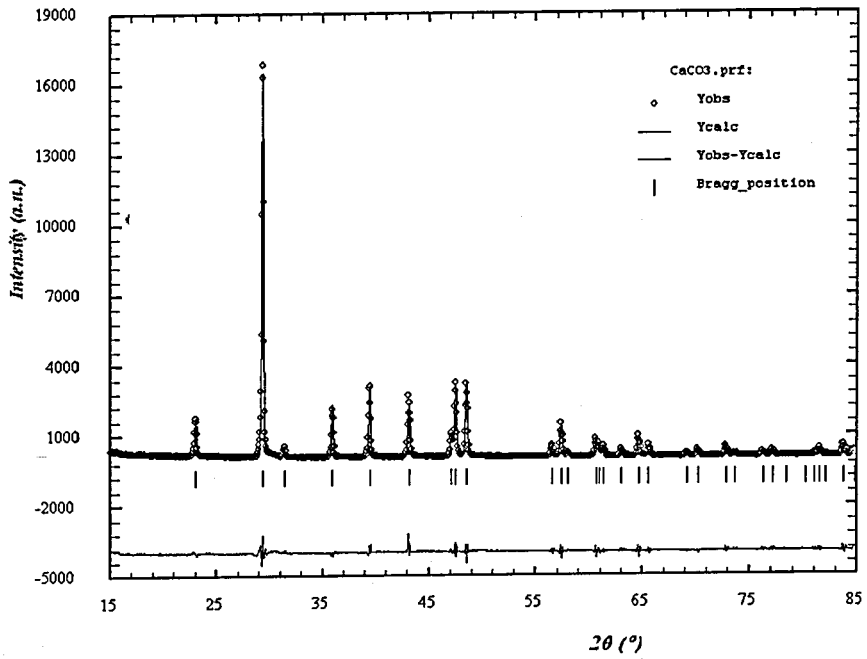

Figure 3.1.7: Observed and refined X-ray pattern of $CaCO_3$

Atom	Wyckoff Notation	Atomic positions for the orthorhombic structure of $CaCO_3$ using space group *R-3c* [25]			Atomic positions for the orthorhombic structure of $CaCO_3$ using space group *R-3c* after refinement with FullProf [5]		
		x	y	z	x (z)	y (x)	z (y)
Ca	6b	0	0	0	0	0	0
C	6a	0	0	¼	0	0	¼
O	18e	0.2570(1)	0	¼	0.2576 (8)	0	¼

Lattice Parameters and Angles			Lattice Parameters (Å) and Angles (°)		
a (Å)	b (Å)	c (Å)	a (Å)	b (Å)	c (Å)
4.9887 (1)	4.9887 (1)	17.0529 (8)	4.9895 (6)	4.9895 (6)	17.0661 (7)
α (°)	β (°)	γ (°)	α (°)	β (°)	γ (°)
90	90	120	90	90	120
$\chi^2 = 3.62$			$\chi^2 = 6.03$		

Table 3.1.4: Atomic positions and lattice parameters of the model and refined parameters of $CaCO_3$ using space group R-3c

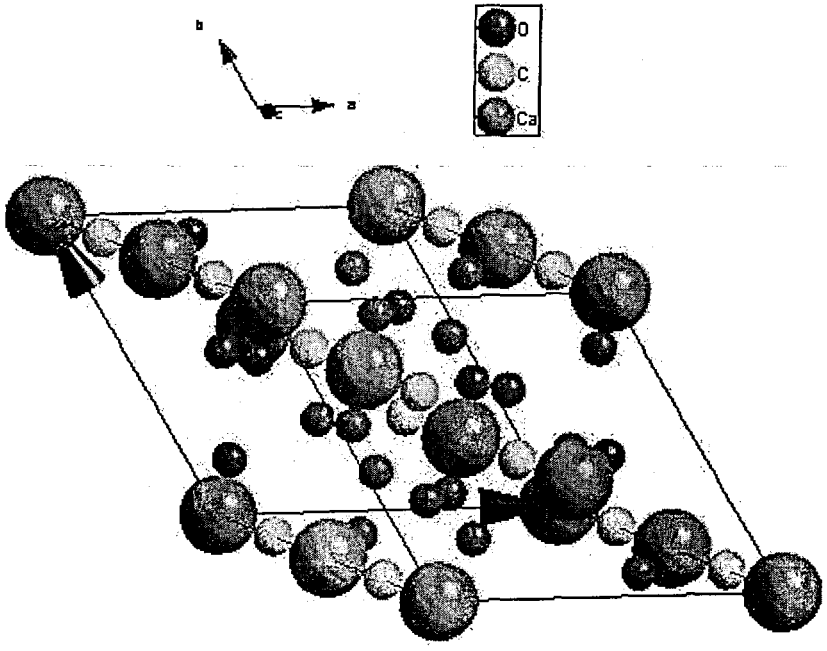

Figure 3.1.8: The crystallographic structure plot of $CaCO_3$

The refined model and crystallographic data of $CaRuO_3$ can be seen in figure 3.1.7 and table 3.1.4. The deviation of the model and the deviation of the refined parameters are

within the error bars and quite close to each other with a value of χ^2=6.03. The rhombohedral shape of the $CaCO_3$ unit cell is shown in figure 3.8. The angles have not been refined and are kept constant at $\alpha=\beta=90°$ and $\gamma=120°$.

3.1.2 Preparation of $SrRuO_3$, $CaRuO_3$, $Sr_{(1-x)}Ca_xRuO_3$ and Sr_2RuO_4

The dried Ruthenium (IV) Oxide (RuO_2) was mixed with the correct stoichiometric quantity of Strontium Carbonate ($SrCO_3$) for strontium compounds $SrRuO_3$ and Sr_2RuO_4, mixed with calcium carbonate ($CaCO_3$) for the calcium containing compound $CaRuO_3$ and the strontianite dopped with Calcium Carbonate to obtain $Sr_{0.5}Ca_{0.5}RuO_3$ and $Sr_{0.75}Ca_{02.5}RuO_3$. The formulae for the chemical reactions of these compounds are given below. The homogeneous powder mixtures were compressed into pellets to ensure that all grains are tightly packed. The pellets were fired in air at 800°C for 20h and then at 1100°C for 72h. After cooling the pellets were reground for an X-ray diffraction investigation in order to check the composition of the final product [12, 13, 14, 15, 16]. This process was repeated 3 times and includes the following reactions:

$$SrCO_3 + RuO_2 \rightarrow SrRuO_3 + CO_2$$
$$2SrCO_3 + RuO_2 \rightarrow Sr_2RuO_4 + 2CO_2$$
$$CaCO_3 + RuO_2 \rightarrow CaRuO_3 + CO_2$$
$$\tfrac{1}{2}SrCO_3 + \tfrac{1}{2}CaCO_3 + RuO_2 \rightarrow Sr_{0.5}Ca_{0.5}RuO_3 + CO_2$$
$$\tfrac{3}{4}SrCO_3 + \tfrac{1}{4}CaCO_3 + RuO_2 \rightarrow Sr_{0.75}Ca_{0.25}RuO_3 + CO_2$$

3.1.3 Structural Characterisation using X-rays

3.1.3.1 Structural characterisation of $SrRuO_3$ using X-ray diffraction

The $SrRuO_3$ has an orthorhombic structure at room temperature. It is similar to the structure of many ABO_3 perovskite compounds. In the literature its space group has been reported as *Pbnm* [12, 13], while in other publications it is quoted as *Pnma* [18, 19, 20] (space group No. 62 of the International Tables of Crystallography [3]). *Pbnm* is a Hermann-Mauguin symbol for various settings of the same unit cell of *Pnma*. Thus,

Pbnm can be converted to the space group *Pnma* [11] in a similar manner as has been done for $SrCO_3$. This is explained in detail in appendix 1.

In the quoted papers the main difference arises from the coordinates chosen for the Ru atom. A Ru atom might be placed in one of three different positions: These are *4a (0, 0, 0)*, *4b (0, 0, 0.5)* or *4c (0, 0.25, 0)*. The positions of other atoms (Sr, O1 and O2) are changing in accordance with the chosen position of Ru. Thus, not the size of the unit cell but the coordinates of atoms in the unit cell vary according to the different choices made by various authors. The conventional space group setting of *Pnma* has been chosen for this refinement with the Ru position at *4b (0, 0, 0.5)*. The refined data and plots are shown in figure 3.1.9 and table 3.1.5

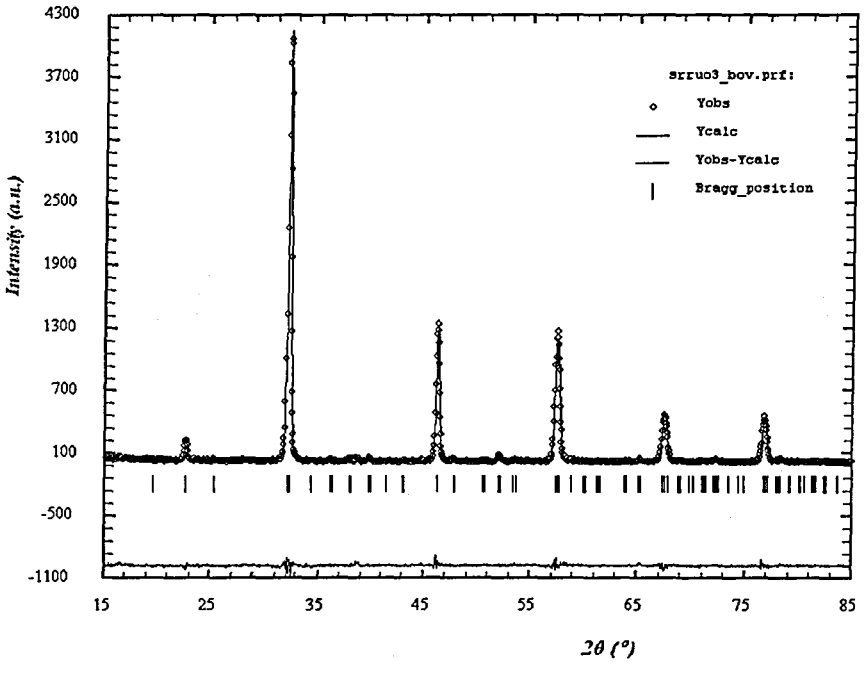

Figure 3.1.9: The observed and refined X-ray diffraction pattern of $SrRuO_3$

Atom	Wyckoff Notation	Atomic position for orthorhombic structure of $SrRuO_3$ using space group *Pnma* [13,20]			Atomic position for orthorhombic structure of $SrRuO_3$ using space group *Pnma* after refinement with FullProf [11]		
		x	y	z	x (z)	y (x)	z (y)
Sr	4c	0.0157(4)	¼	-0.0027(3)	0.0176 (8)	¼	-0.007 (1)
Ru	4b	0	0	½	0	0	½
O1	4c	0.4966(5)	¼	0.0532(4)	0.522 (6)	¼	0.078 (7)
O2	8d	0.2764(2)	0.0278(2)	0.7248(2)	0.226 (8)	0.03 (7)	0.785 (6)

Lattice Parameters [13,20]			Lattice Parameters		
a (Å)	b (Å)	c (Å)	a (Å)	b (Å)	c (Å)
5.5304 (1)	7.8446 (2)	5.5670 (1)	5.552 (1)	7.843 (2)	5.560 (1)
χ^2=1.57			χ^2=1.63		

Table 3.1.5: Atomic positions and lattice parameters of $SrRuO_3$ using space group Pnma

The calculated X-ray diffraction agrees well with the observed pattern. This is reflected in the value of χ^2=1.63 obtained for this fit. The model parameters agree well with those of references [13, 20]. All refined values deviate slightly from the values given in [13, 20]. There is no evidence of any additional phases or unidentified peaks within the pattern. Figure 3.1.10 and 3.1.11 show the crystallographic structure of $SrRuO_3$.

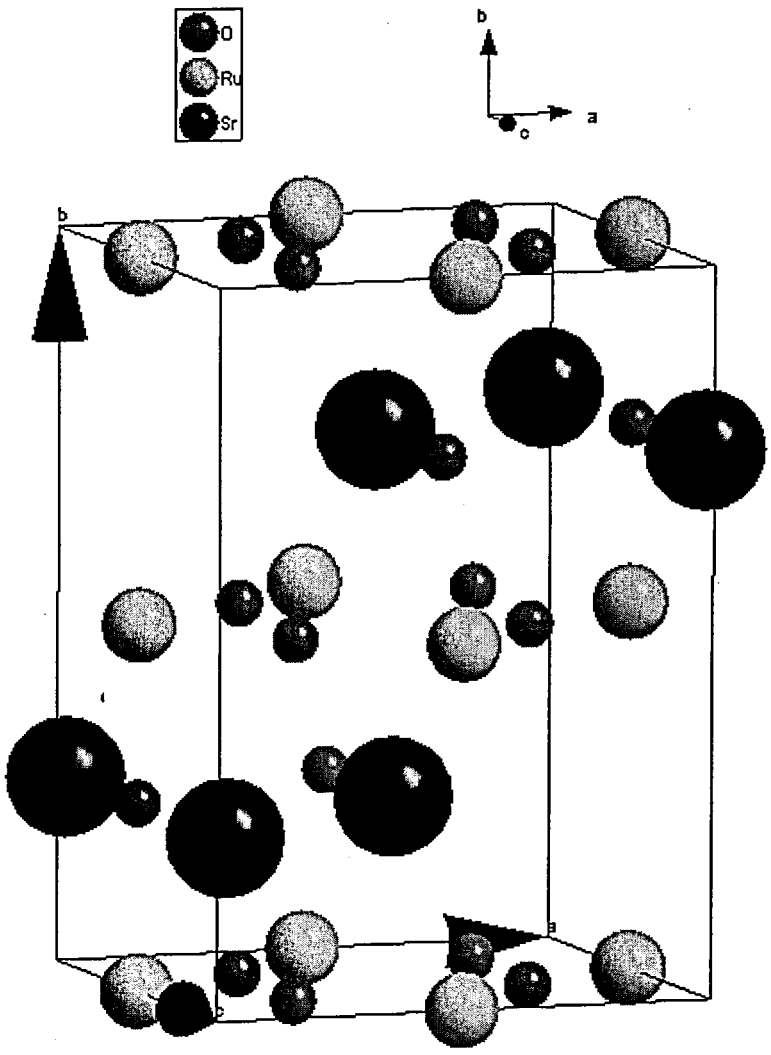

Figure 3.1.10: The crystallographic structure of $SrRuO_3$

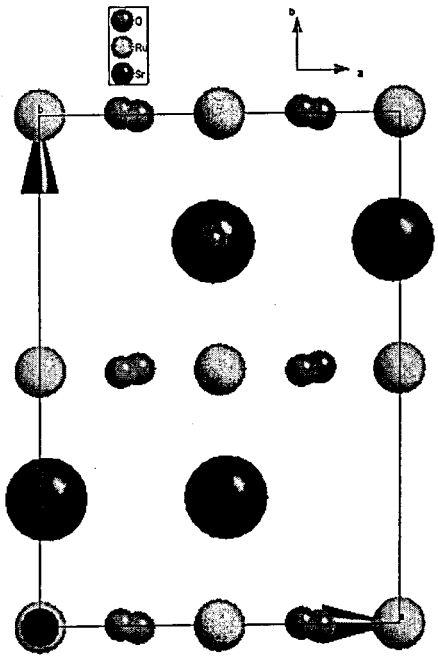

Figure 3.1.11-a

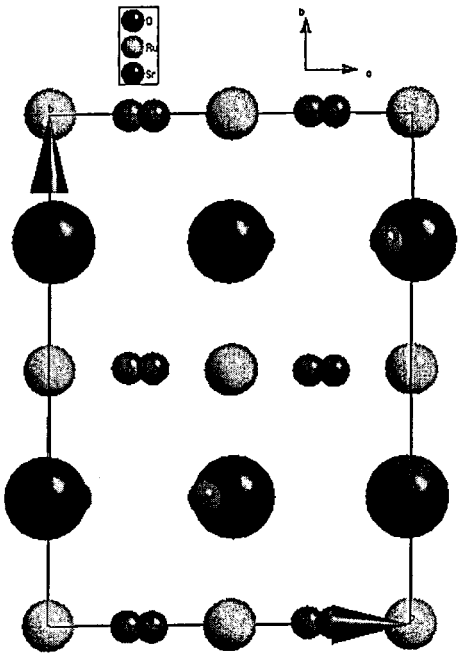

Figure 3.1.11-b

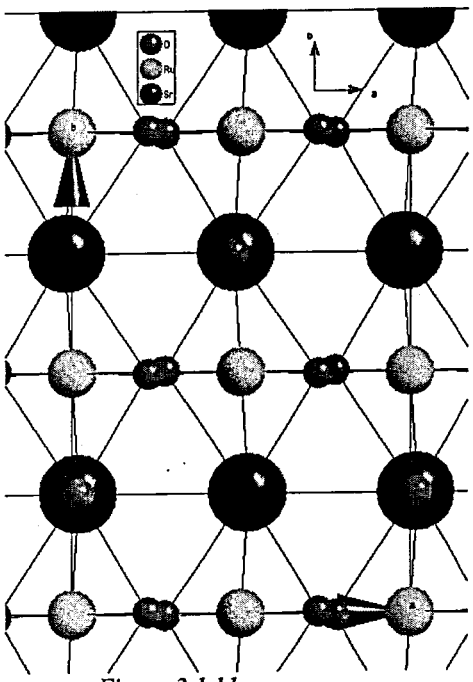

Figure 3.1.11-c

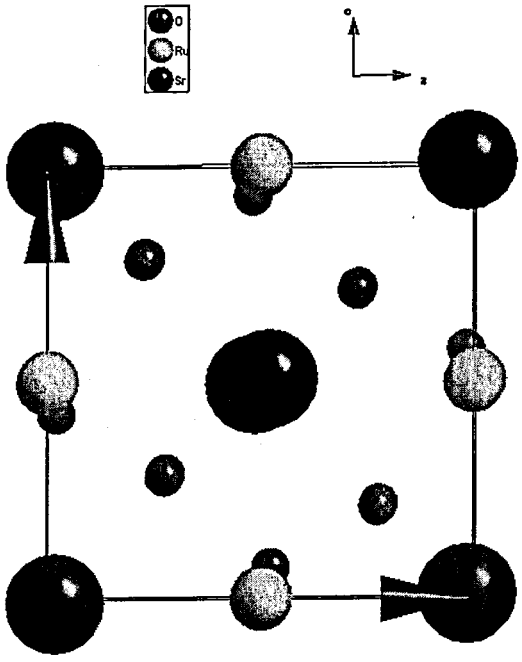

Figure 3.1.11-d

Figure 3.1.11: The crystallographic structure plots from different planes of $SrRuO_3$. a) b-a plane (001), b) b-c plane (100), c) bonds between the atoms, d) c-a plane (010)

It is claimed in the literatures [12, 20, 26] that $SrRuO_3$ has a cubic structure with the space group of *Pm-3* (#200. [11]) at high temperatures. This cubic structure has also been included in the refinement at room temperature. However no cubic component was observed even as a second phase. The $SrRuO_3$ sample has been found to be in the distorted cubic structure which is deformed to an orthorhombic crystal as reported in [13, 20]. As a consequence, $SrRuO_3$ is a tilted perovskite with an orthorhombic structure. This tilted perovskite can be easily seen with the three dimensional structure plots of $SrRuO_3$ especially in figure 3.1.11c.

3.1.3.2 Structural characterisation of Sr_2RuO_4 using X-ray diffraction

The crystal structure of Sr_2RuO_4 is of the K_2NiF_4 type with space group *I4/mmm* (#139 in the International Tables for Crystallography [3]) [21]. The atom positions and lattice parameters have been refined using FullProf [5] and using the model of reference [22] as a starting point.

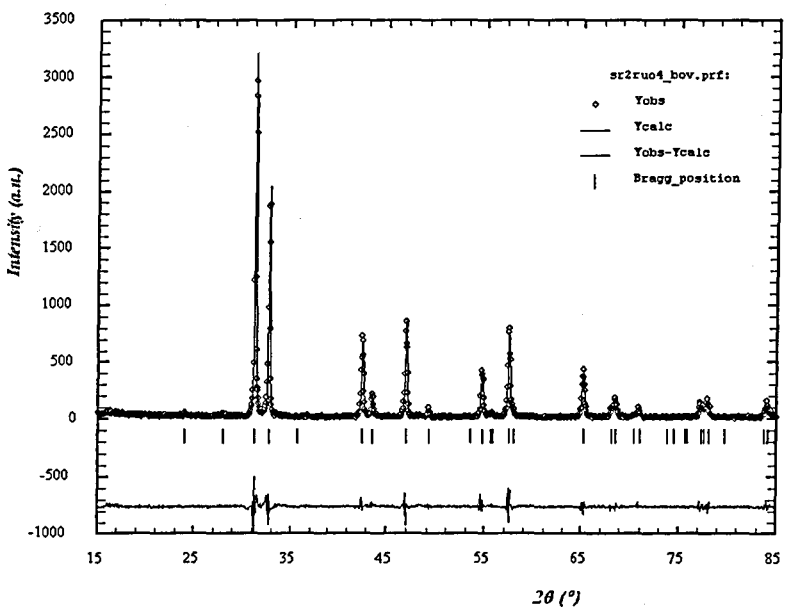

Figure 3.1.12: Observed and refined X-ray diffraction pattern of Sr_2RuO_4

Atom	Wyckoff Notation	Atomic position for tetragonal structure of Sr_2RuO_4 using space group *I4/mmm* [25]			Atomic position for tetragonal structure of Sr_2RuO_4 using space group *I4/mmm* after refinement using FullProf		
		x	y	z	x (z)	y (x)	z (y)
Sr	4e	0	0	0.14684 (2)	0	0	0.1465 (4)
Ru	2b	0	0	½	0	0	½
O1	4c	0	½	0	0	½	0
O2	4e	0	0	0.3381 (1)	0	0	0.339 (2)

Lattice Parameters			Lattice Parameters		
a (Å)	b (Å)	c (Å)	a (Å)	b (Å)	c (Å)
3.8603 (1)	3.8603 (1)	12.729 (2)	3.8703 (6)	3.8703 (6)	12.730 (2)
χ^2=1.96			χ^2=2.12		

Table 3.1.6: Model and refined parameters of Sr_2RuO_4

As seen in figure 3.1.12 and table 3.1.6, there is excellent agreement between the parameters of reference [22] and the values obtained in the refinement. The sample is of high quality with no additional phases or impurities. Figure 3.1.13 and 3.1.14 illustrate the crystallographic structure of Sr_2RuO_4.

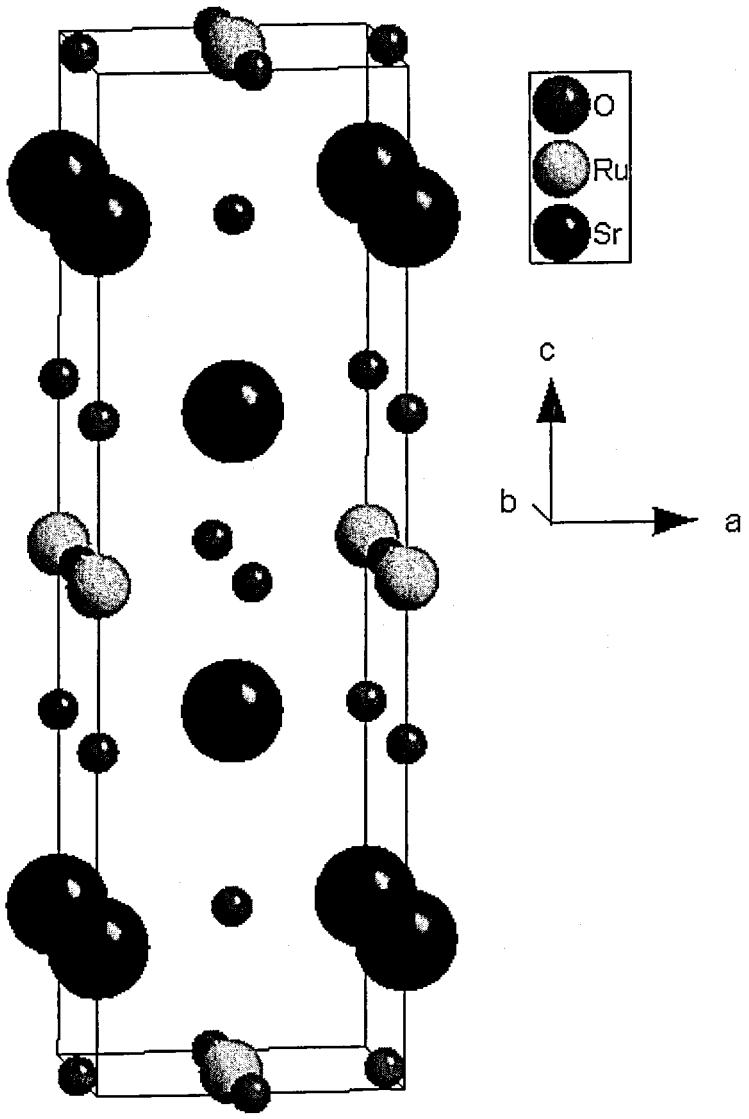

Figure 3.1.13: The crystallographic structure of Sr_2RuO_4

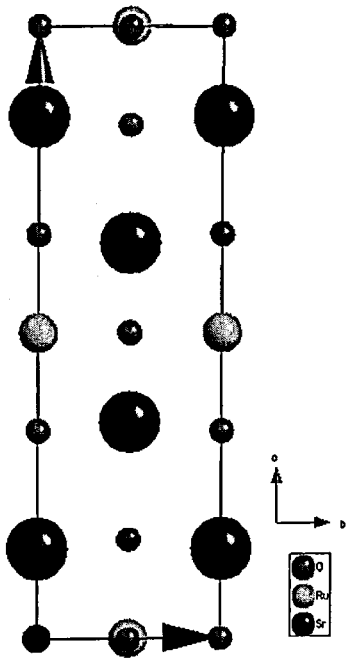

Figure 3.1.14-a

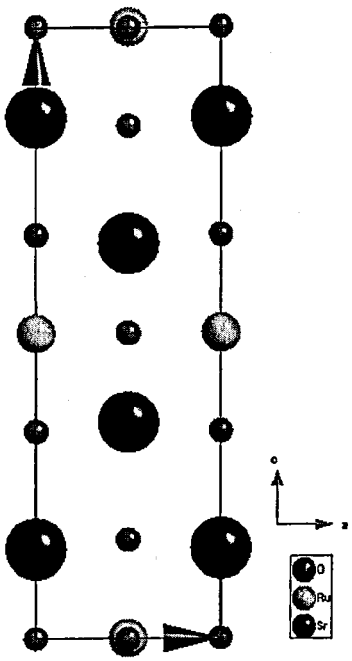

Figure 3.1.14-b

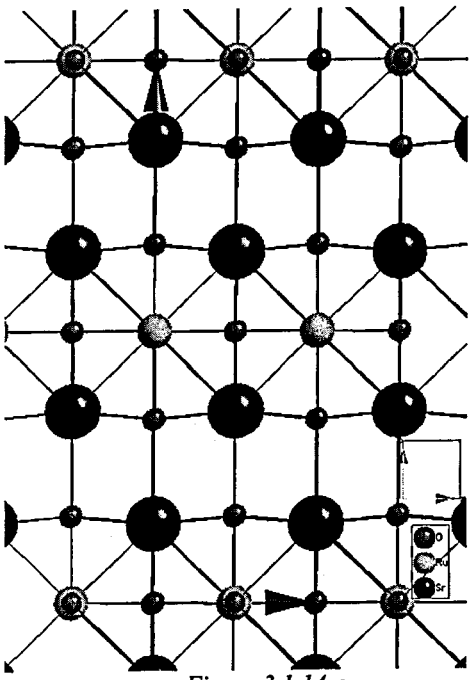

Figure 3.1.14-c

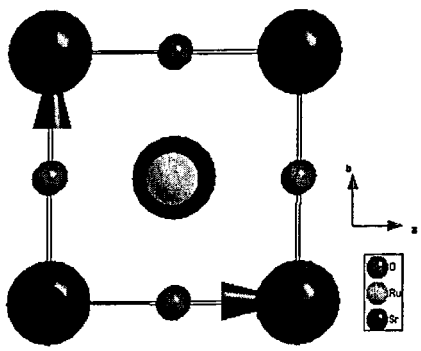

Figure 3.1.14-d

Figure 3.1.14: The crystallographic structure plots for different planes of Sr_2RuO_4. a) c-b plane (100), b) c-a plane (010), c) Bonds between the atoms d) b-a plane (001)

As mentioned above, Sr_2RuO_4 crystallizes in the K_2NiF_4 type structure which is realized for a considerable number of compounds with general composition A_2BX_4. The structure of Sr_2RuO_4 can be built up theoretically by three perovskite monolayers stacked along the resulting *c* axis where layers 1 and 3 are AXB_3 perovskite cells centred on *B* atoms [27]. Similar to the structure of $SrRuO_3$ in figure 3.1.11, the three dimensional perovskite structure of Sr_2RuO_4 can be appreciated from figure 3.1.13.

3.1.3.3 Structural characterisation of $CaRuO_3$ using X-ray diffraction

The perovskite $CaRuO_3$ has similar crystallographic properties compared to $SrRuO_3$. However, they show different electrical and magnetic properties. $CaRuO_3$ crystallises in the same space group as $SrRuO_3$ namely *Pnma*. Results in [19] indicate that $CaRuO_3$ has a smaller unit cell volume compared to $SrRuO_3$.

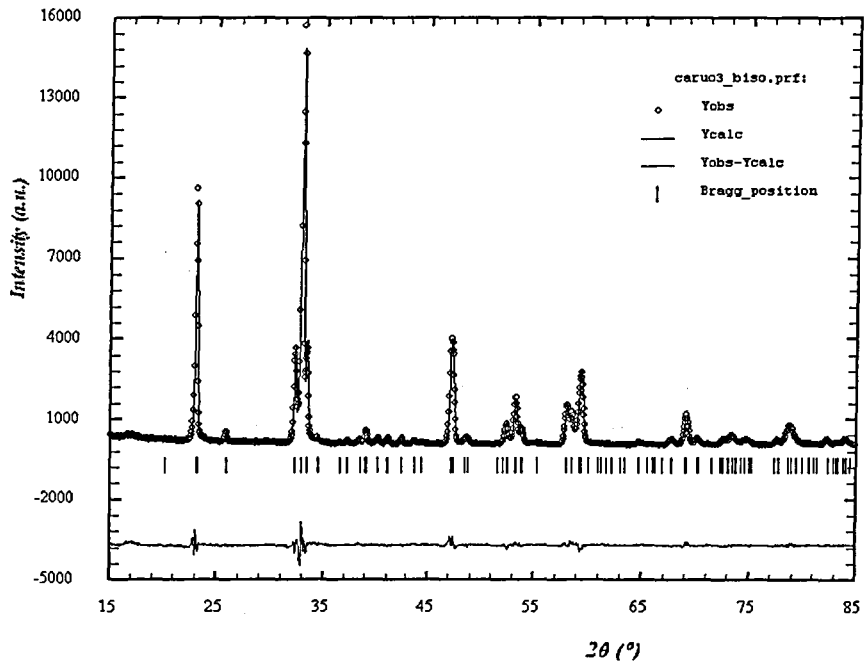

Figure 3.1.15: Observed and refined X-ray diffraction pattern of $CaRuO_3$

Atom	Wyckoff Notation	Atomic position for orthorhombic structure of $CaRuO_3$ using space group *Pnma* [13,20]			Atomic position for orthorhombic structure of $CaRuO_3$ using space group *Pnma* after refinement with FullProf [11]		
		x	y	z	x (z)	y (x)	z (y)
Ca	4c	0.0552 (4)	¼	-0.0139 (2)	0.0583 (7)	¼	-0.015 (1)
Ru	4b	0	0	½	0	0	½
O1	4c	0.4742 (5)	¼	0.0920 (4)	0.484 (3)	¼	0.095 (2)
O2	8d	0.2979 (2)	0.0482 (2)	0.6973 (2)	0.292 (2)	0.052 (2)	0.700 (2)

Lattice Parameters [13,20]			Lattice Parameters		
a (Å)	b (Å)	c (Å)	a (Å)	b (Å)	c (Å)
5.5304 (1)	7.8446 (2)	5.5670 (1)	5.552 (2)	7.843 (2)	5.560 (1)
χ^2=2.2			χ^2=2.04		

Table 3.1.7: Model and refined parameters of $CaRuO_3$

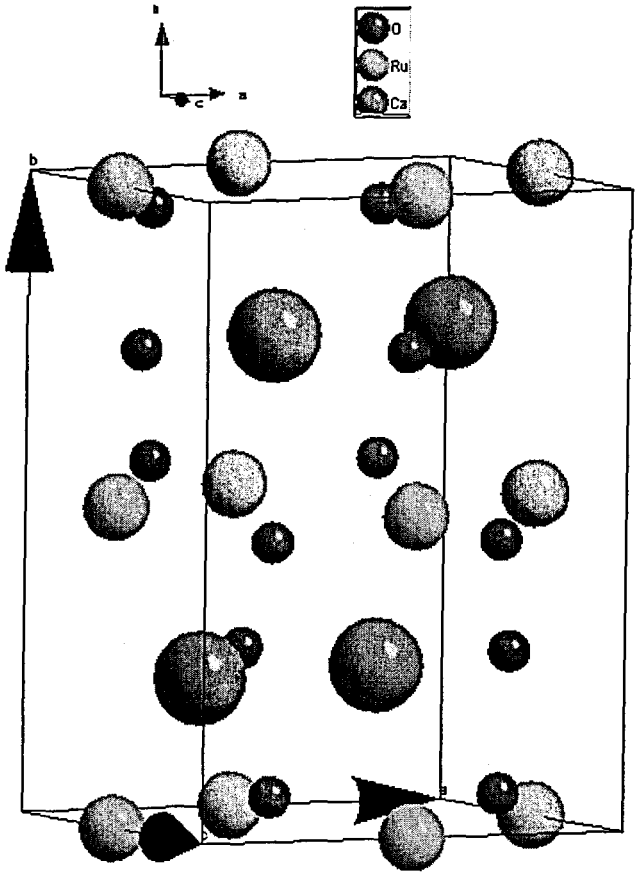

Figure 3.1.16: The crystallographic structure plot of $CaRuO_3$

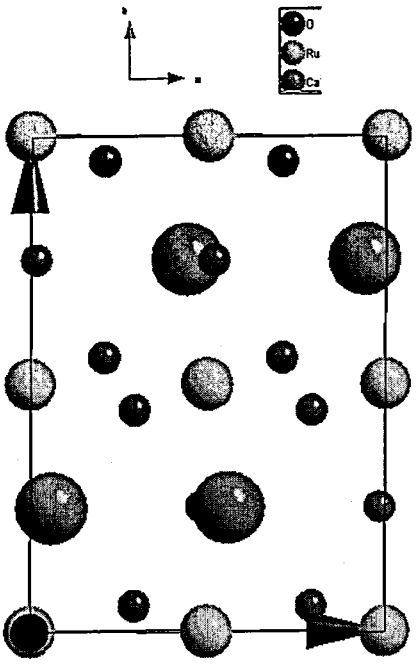

Figure 3.1.17-a

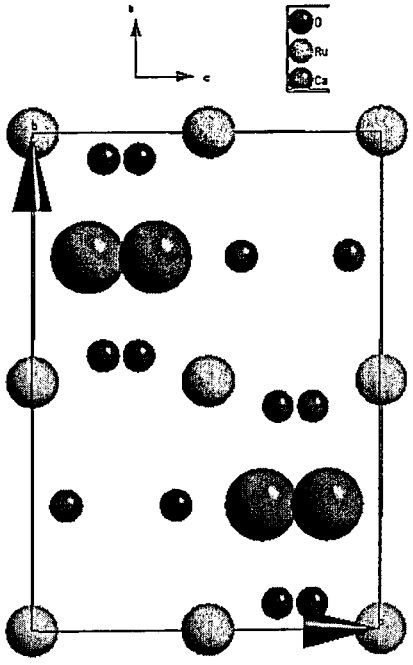

Figure 3.1.17-b

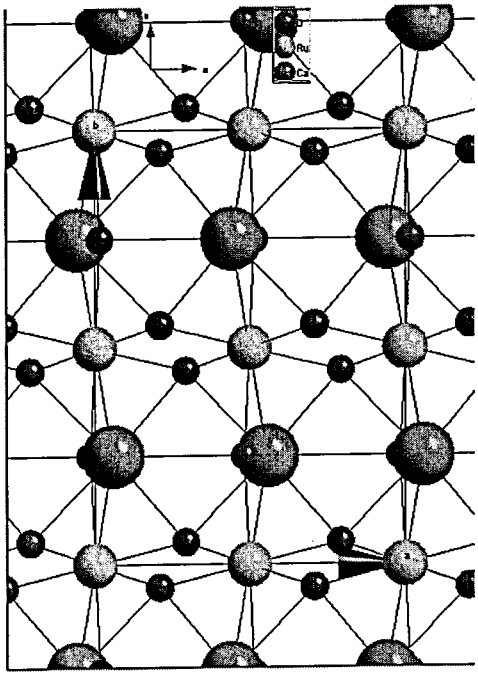

Figure 3.1.17-c

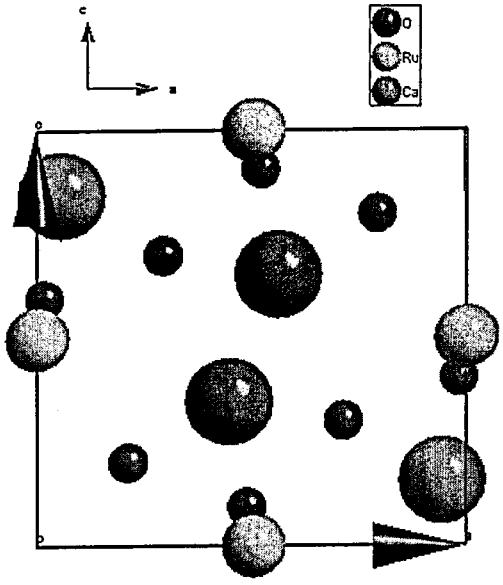

Figure 3.1.17-d

Figure 3.1.17: The crystallographic structure plots for different planes of $CaRuO_3$. a) b-a plane (001), b) b-c plane (100), c)Bonds between the atoms, d) c-a plane (010)

All the values which are refined using FullProf [5] are shown to be similar to the parameter of model [13, 20], with a value of χ^2=2.04 (figure 3.1.15, table 3.1.7). Similar to $SrRuO_3$, $CaRuO_3$ also has a distorted cubic structure. The orthorhombic structure is due to this distortion. The Ru atom is surrounded by 6 O atoms. These O atoms are tilted due to the presence of Ca or Sr atoms. This is clearly shown in figures 3.1.17-c and 3.1.11-c.

3.1.3.5 Structural characterisation of $Sr_{(1-x)}Ca_xRuO_3$ with X-ray diffraction

Two different calcium doped strontium ruthenates ($Sr_{(1-x)}Ca_xRuO_3$, x= 0.75, 0.5) have been prepared to obtain more detailed information about the magnetic structure of ruthenates. As reported before, the calcium doped ruthenates crystallise in the same space group (*Pnma*, #62) as $SrRuO_3$ [20, 28, 29]. The graphs of the X-ray diffraction pattern and crystal structures can be seen below.

a) $Sr_{0.75}Ca_{0.25}RuO_3$

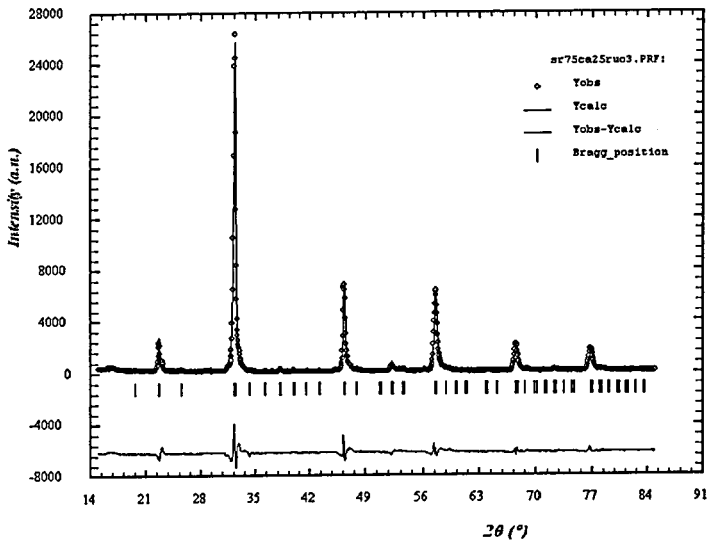

Figure 3.1.18: Observed and refined X-ray diffraction pattern of $Sr_{0.75}Ca_{0.25}RuO_3$

Atom	Wyckoff Notation	Atomic position for orthorhombic structure of $Sr_{0.75}Ca_{0.25}RuO_3$ using space group *Pnma* [20]			Atomic position for orthorhombic structure of $Sr_{0.75}Ca_{0.25}RuO_3$ using space group *Pnma* after refinement with FullProf [11]		
		x	y	z	x (z)	y (x)	z (y)
Sr	4c	0.0400 (5)	0.25000	-0.009 (1)	0.025 (1)	0.25000	-0.001 (4)
Ca	4c	0.0400 (5)	0.25000	-0.009 (1)	0.025 (1)	0.25000	-0.001 (4)
Ru	4b	0	0	½	0	0	½
O1	4c	0.480 (3)	0.25000	0.079 (4)	0.533 (8)	0.25000	0.08 (1)
O2	8d	0.296 (2)	0.0427 (9)	0.705 (9)	0.208 (6)	0.023 (6)	0.75 (1)

Lattice Parameters [13,20]			Lattice Parameters		
a (Å)	b (Å)	c (Å)	a (Å)	b (Å)	c (Å)
5.5127 (9)	7.7392 (3)	5.444 (2)	5.553 (7)	7.8486 (6)	5.524 (1)
χ^2=5.9			χ^2=17.2		

Table 3.1.8: Model and refined parameters of $Sr_{0.75}Ca_{0.25}RuO_3$

The parameters obtained for $Sr_{0.75}Ca_{0.25}RuO_3$ (Fig 3.1.18, table 3.1.8) are similar to the model ones of [20]. The refinement yields χ^2 =17.2. No additional phases or impurities have been detected.

b) $Sr_{0.5}Ca_{0.5}RuO_3$

While analysing the $Sr_{0.5}Ca_{0.5}RuO_3$ data a model which only uses one phase does not give the best fit. Thus, a second phase, $CaRuO_3$ has been added to the model in order to obtain a better fit. Results are shown below in figure 3.1.19 and tables 3.1.9, 3.10.

Atom	Wyckoff Notation	Atomic position for orthorhombic structure of $Sr_{0.5}Ca_{0.5}RuO_3$ in space group *Pnma* [20]			Atomic position for orthorhombic structure of $Sr_{0.5}Ca_{0.5}RuO_3$ in space group *Pnma* after refinement with FullProf [11]		
		x	y	z	x (z)	y (x)	z (y)
Sr	4c	0.0337 (7)	0.25000	-0.006 (2)	0.014 (2)	0.25000	0.1 (1)
Ca	4c	0.0337 (7)	0.25000	-0.006 (2)	0.014 (2)	0.25000	0.1 (1)
Ru	4b	0	0	½	0	0	½
O1	4c	0.488 (4)	0.25000	0.084 (9)	0.527 (1)	0.25000	0.48 (6)
O2	8d	0.294 (3)	0.031 (4)	0.711 (5)	0.215 (8)	0.022 (5)	0.73 (2)

Lattice Parameters [13,20]			Lattice Parameters		
a (Å)	b (Å)	c (Å)	a (Å)	b (Å)	c (Å)
5.5136(4)	7.7921(6)	5.4932(4)	5.556 (1)	7.858 (2)	5.513 (2)
χ^2=5.9			χ^2=6.67		

Table 3.1.9: Model and refined parameters of the first phase of $Sr_{0.5}Ca_{0.5}RuO_3$

Atom	Wyckoff Notation	Atomic position for orthorhombic structure of $CaRuO_3$ using space group *Pnma* [13,20]			Atomic position for orthorhombic structure of $CaRuO_3$ using space group *Pnma* after refinement with FullProf [11]		
		x	y	z	x (z)	y (x)	z (y)
Ca	4c	0.0552 (4)	¼	-0.0139 (2)	0.039 (3)	¼	0.003 (7)
Ru	4b	0	0	½	0	0	½
O1	4c	0.4742 (5)	¼	0.0920 (4)	0.48 (1)	¼	0.067 (8)
O2	8d	0.2979 (2)	0.0482 (2)	0.6973 (2)	0.294 (8)	0.0748 (4)	0.703 (7)

Lattice Parameters [13,20]			Lattice Parameters		
a (Å)	b (Å)	c (Å)	a (Å)	b (Å)	c (Å)
5.5304 (1)	7.8446 (2)	5.5670 (1)	5.531 (3)	7.719 (3)	5.406 (2)
χ^2=2.2			χ^2=6.67		

Table 3.1.10: Model and refined parameters of the second phase of $Sr_{0.5}Ca_{0.5}RuO_3$

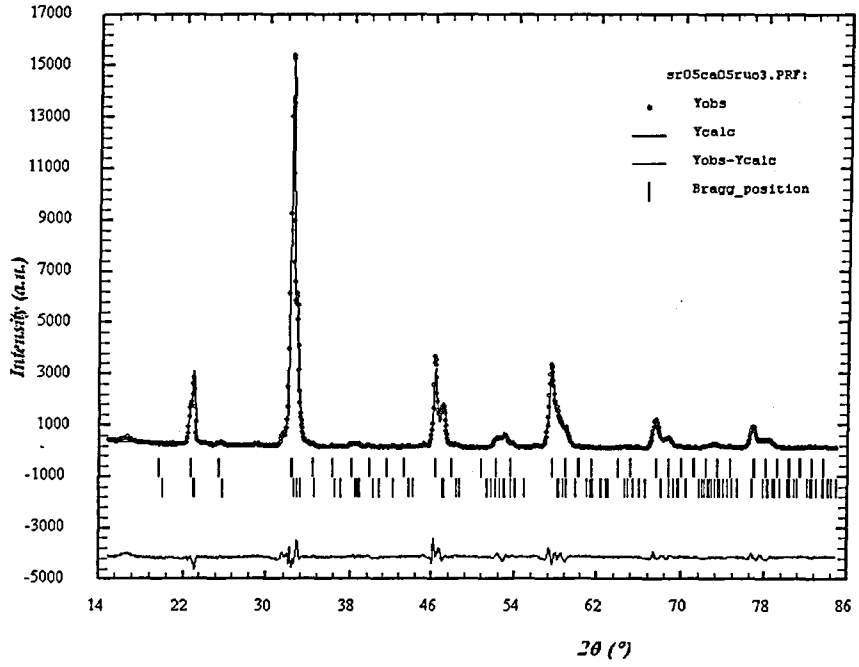

Figure 3.1.19: Observed and refined X-ray diffraction pattern of $Sr_{0.5}Ca_{0.5}RuO_3$

Despite $Sr_{0.75}Ca_{0.25}RuO_3$ being single phase, $Sr_{0.5}Ca_{0.5}RuO_3$ possesses a second phases of $CaRuO_3$ (figure 3.1.19 and tables 3.1.9 and 3.1.10). The ratio between $Sr_{0.5}Ca_{0.5}RuO_3$ and

$CaRuO_3$ has been calculated using the scale factors and the ratio of $Sr_{0.5}Ca_{0.5}RuO_3$ / $CaRuO_3$ and a value of 0.7504 has been found. After adding the second phase to the model, χ^2=6.67 was obtained. A more detailed investigation of the crystallographic characterisation has been carried out using neutron diffraction.

3.2 Structural Characterisation using Neutrons

To further characterise the samples $SrRuO_3$, $Sr_{(1-x)}Ca_xRuO_3$ and $CaRuO_3$ neutron diffraction experiments have been performed on D2B and D20 at the ILL. Neutrons can penetrate much more deeply than X-rays into the crystals. As a result, more detailed information of structure and the magnetic state can be obtained using neutron diffraction.

The neutron diffraction experiments were carried out at various temperatures. Temperature variations help to identify the intensity of magnetic peaks and to calculate the ordered magnetic moment in Bohr magneton per ruthenium atom. It also enables to plot a graph of the temperature scan of the lattice constants and helps in determinating the thermal expansion of the sample.

The models and references for the neutron diffraction investigations are the same as the ones used for X-ray diffraction. Thus, only graphs, refined data and brief comments are given as written in this section.

a) Structural characterisation of $SrRuO_3$ using neutron diffraction

A polycrystalline SrRuO3 neutron diffraction experiment has been carried out on D2B at 2K and 200K. SrRuO3 shows ferromagnetism below 160K. Using the program FullProf [5] the ordered moment measured in Bohr magneton per ruthenium atom is calculated and obtained with a value of 0.6600(±0.0001) μ_B/Ru at 2K for $SrRuO_3$.

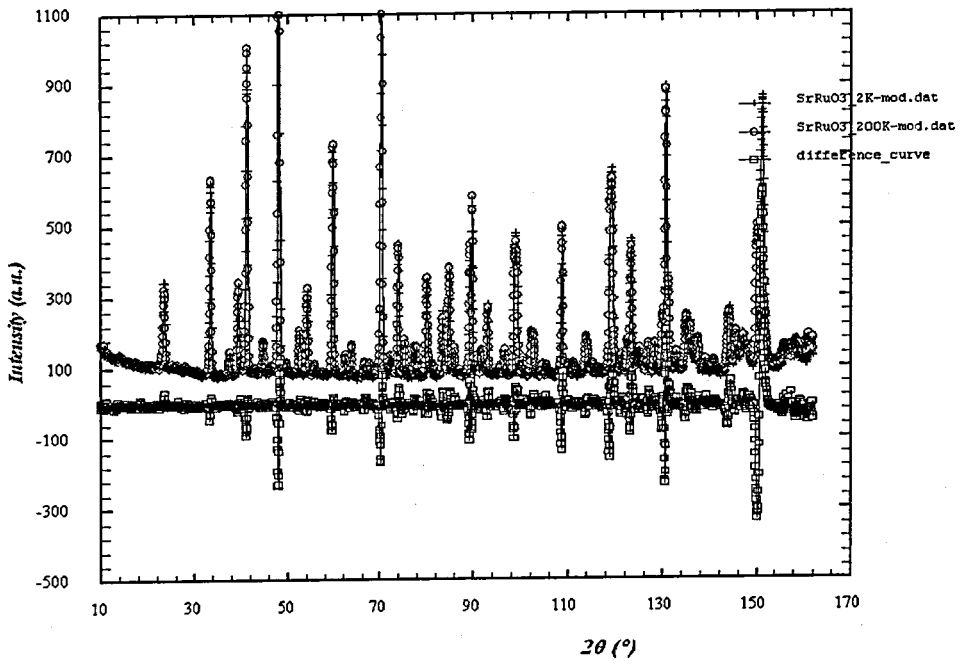

Figure 3.2.1: Intensity differences ($I_{2K}-I_{200K}$) for $SrRuO_3$

Figure 3.2.1 illustrates the intensity difference between 2K and 200K for $SrRuO_3$. The change in intensity at low angles around Bragg peaks is due to magnetic alignment at low temperature. Magnetically ordered moments cause a change in the intensity and this is reflected in the intensity of Bragg peaks at low angles. The changes in high angles reveal the change in unit cell lattice parameters as a result of the thermal expansion or shrinking.

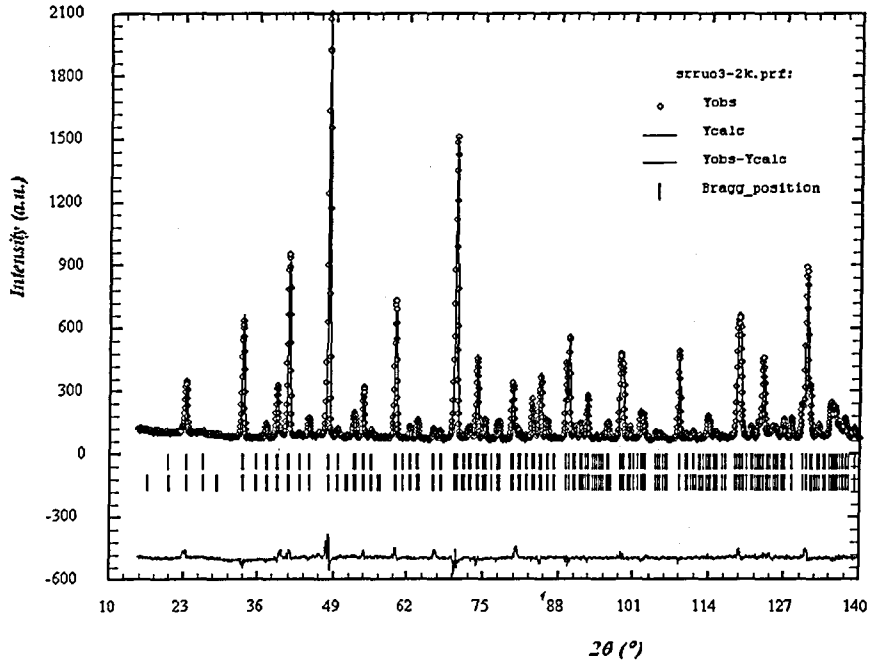

Figure 3.2.2: Refined neutron diffraction pattern of $SrRuO_3$ at 2K. The second phase presents the magnetic refinement.

Atom	Wyckoff Notation	Atomic positions for the orthorhombic structure of $SrRuO_3$ using space group *Pnma* [13,20]			Atomic positions for the orthorhombic structure of $SrRuO_3$ at 2K using space group *Pnma* after refinement using FullProf [11]		
		x	y	z	x (z)	y (x)	z (y)
Sr	4c	0.0157 (4)	¼	-0.0027 (3)	0.0188 (4)	¼	-0.0014 (5)
Ru	4b	0	0	½	0	0	½
O1	4c	0.4966 (5)	¼	0.0532 (4)	0.4948 (5)	¼	0.0543 (5)
O2	8d	0.2764 (2)	0.0278 (2)	0.7248 (2)	0.2793 (3)	0.0285 (2)	0.7218 (3)

Lattice Parameters [13,20]			Lattice Parameters		
a (Å)	b (Å)	c (Å)	a (Å)	b (Å)	c (Å)
5.5304 (1)	7.8446 (2)	5.5670 (1)	5.5302 (1)	7.8439 (1)	5.5652 (1)
χ^2=1.57			χ^2=6.6		
Magnetic Moment: 0.72(1) μ_B/Ru			Magnetic Moment: 0.66(1) μ_B/Ru		

Table 3.2.1: Observed and refined neutron parameters of $SrRuO_3$ at 2K

The refined patterns of $SrRuO_3$ for T=2K and 200K are shown in figure 3.2.2, figure 3.2.3 and table 3.2.1, table 3.2.2 respectively. At 200K the model has only taken into account nuclear scattering.

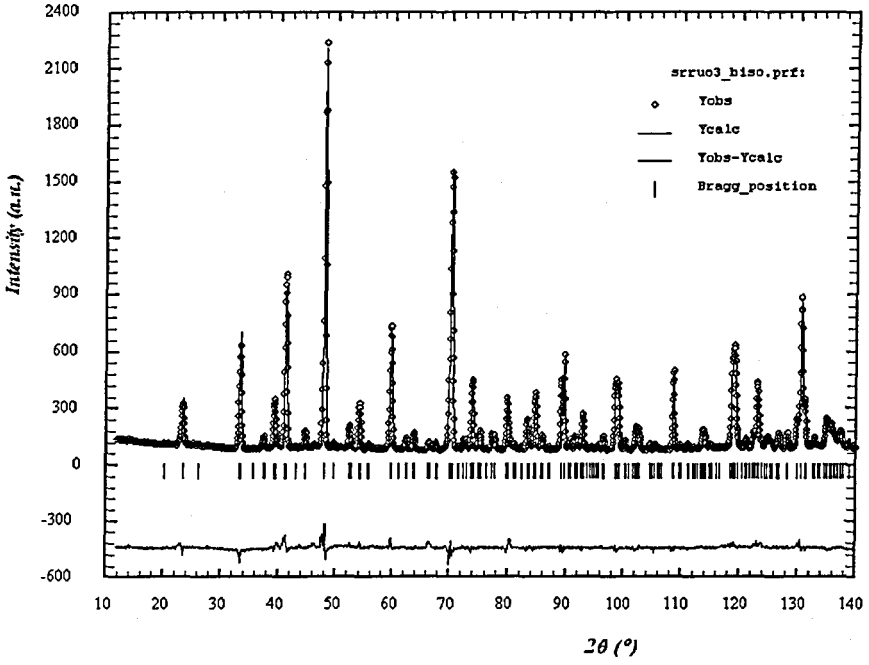

Figure 3.2.3: Observed and refined neutron diffraction pattern of $SrRuO_3$ at 200K

Atom	Wyckoff Notation	Atomic position in orthorhombic structure of $SrRuO_3$ in the space group *Pnma* [13,20]			Atomic position in orthorhombic structure of $SrRuO_3$ at 200K in the space group *Pnma* after refinement using FullProf [11]		
		x	y	z	x (z)	y (x)	z (y)
Sr	4c	0.0157 (4)	¼	-0.0027 (3)	0.0172 (4)	¼	-0.0016 (5)
Ru	4b	0	0	½	0	0	½
O1	4c	0.4966 (5)	¼	0.0532 (4)	0.4962 (5)	¼	0.0539 (4)
O2	8d	0.2764 (2)	0.0278 (2)	0.7248 (2)	0.2786 (3)	0.0277 (2)	0.7228 (3)

Lattice Parameters [13,20]			Lattice Parameters		
a (Å)	b (Å)	c (Å)	a (Å)	b (Å)	c (Å)
5.5304 (1)	7.8446 (2)	5.5670 (1)	5.5315 (9)	7.8462 (1)	5.5685 (9)
χ^2=1.57			χ^2=6.1		

Table 3.2.2: Model and Refined neutron parameters of $SrRuO_3$ at 200K

As seen in the graphs and tables (figure 3.2.2, 3.2.3 and table 3.2.1, 3.2.2) the refined parameters agree well with the model proposed in [13, 20]. This indicates that the sample preparing procedure was successful and both neutron diffraction and X-ray diffraction experiments are consistent. The unit cell volume for $SrRuO_3$ is 241.411424(116) $Å^3$ at 2K and, 241.680166(193) $Å^3$ at 200K. A larger cell volume at high temperatures is meaningful from a physical point of view due to thermal expansion. However, the magnitude of the expansion is small.

b) Structural Characterisation of Sr_2RuO_4 using Neutron Diffraction

The experimental data for Sr_2RuO_4 was collected at two different temperatures (2K and 300K) using the instrument D20 at the ILL, Grenoble, France. The compound Sr_2RuO_4 becomes superconducting at ~1K [31]. While decreasing the temperature from 300K to 2K the cooling data have also been recorded. This temperature scan helps to see the thermal expansion of the unit cell (figure 3.2.6).

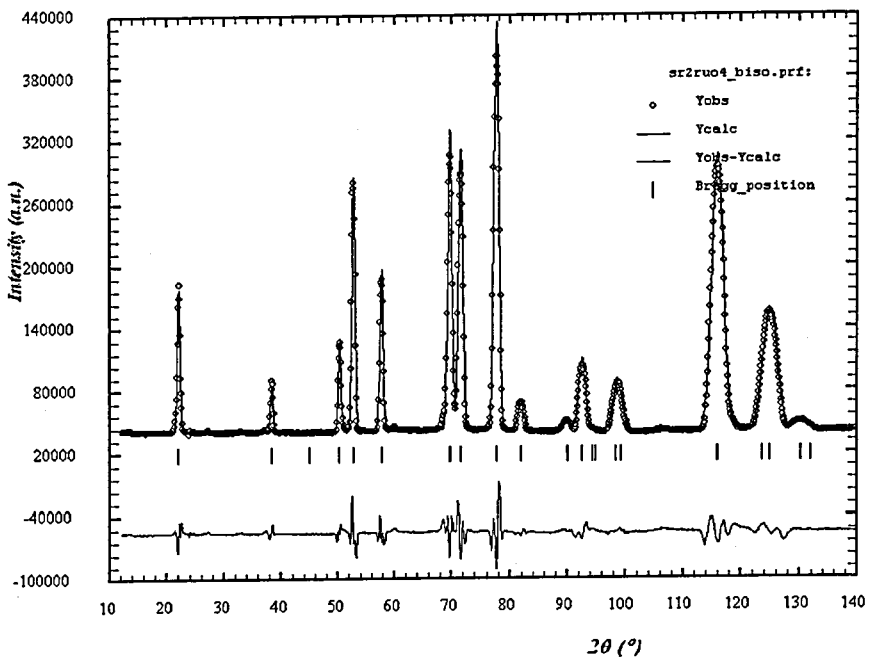

Figure 3.2.4: Observed and refined neutron diffraction pattern of Sr_2RuO_4 at 2K

Atom	Wyckoff Notation	Atomic positions for the tetragonal structure of Sr_2RuO_4 using space group *I4/mmm* [25]			Atomic position for tetragonal structure of Sr_2RuO_4 at 2K using space group *I4/mmm* after refinement with FullProf[5]		
		x	y	z	x (z)	y (x)	z (y)
Sr	4e	0	0	0.14684 (2)	0	0	0.1466 (3)
Ru	2b	0	0	½	0	0	½
O1	4c	0	½	0	0	½	0
O2	4e	0	0	0.3381 (3)	0	0	0.3378 (3)

Lattice Parameters			Lattice Parameters		
a (Å)	b (Å)	c (Å)	a (Å)	b (Å)	c (Å)
3.8603 (1)	3.8603 (1)	12.729 (2)	3.8267 (2)	3.8267 (2)	12.6017 (9)
χ^2=1.96			χ^2=530		

Table 3.2.3: Refined structural parameters of Sr_2RuO_4 at 2K

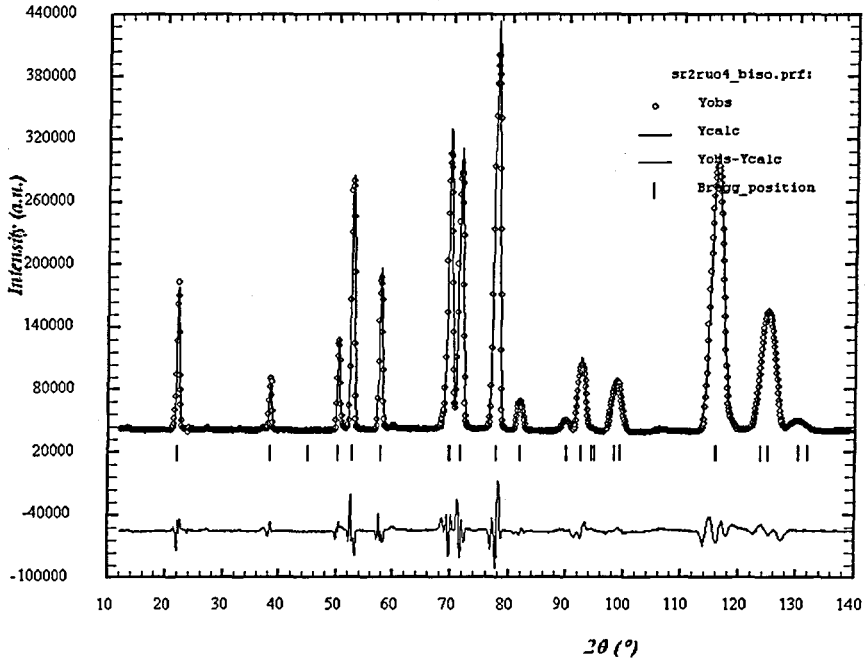

Figure 3.2.5: Observed and refined neutron diffraction pattern of Sr_2RuO_4 at 300K

Atom	Wyckoff Notation	Atomic Position for tetragonal structure of Sr_2RuO_4 using space group *I4/mmm* [25]			Atomic Position for tetragonal structure of Sr_2RuO_4 at 300K using space group *I4/mmm* after refined with FullProf [5]		
		x	y	z	x (z)	y (x)	z (y)
Sr	4e	0	0	0.14684 (2)	0	0	0.1461 (3)
Ru	2b	0	0	½	0	0	½
O1	4c	0	½	0	0	½	0
O2	4e	0	0	0.3381 (3)	0	0	0.3380 (4)

Lattice Parameters			Lattice Parameters		
a (Å)	b (Å)	c (Å)	a (Å)	b (Å)	c (Å)
3.8603 (1)	3.8603 (1)	12.729 (2)	3.8363 (2)	3.8363 (2)	12.619 (1)
χ^2=1.96			χ^2=1180		

Table 3.2.4: Refined neutron data of Sr_2RuO_4 at 300K

The refined data (table 3.2.3 and table 3.2.4) and plots (figure 3.2.4 and figure 3.2.5) of Sr_2RuO_4 at 2K and 300K agree well with references [25, 27]. The χ^2 value is large for both temperatures. The reason for this is due to the huge number of neutrons. The χ^2 is related to the number of independent observations and intensities at angular position θ_i as described in the characterisation section in this chapter and also in the reference number [32]. In practise due to systematic variations and the low statistical error (high count numbers) the systematic errors are more prominent in this analysis than the statistical errors due to counting statistic. As a result, the χ^2 values are high. These are not fully taken into account by the simplified model implemented here. The goodness of fit is believed to be very satisfactory despite the high χ^2 value.

The temperature scans (figure 3.2.6) show the thermal expansion of the lattice parameters and the unit cell of Sr_2RuO_4. The values of a, b and c increase with increasing temperature as expected. This increase is reflected in the volume of Sr_2RuO_4 as shown in figure 3.2.6-c. The temperature variation of the unit cell agrees with [27].

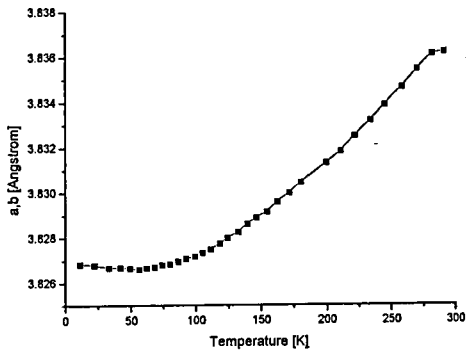

Figure 3.2.6-a

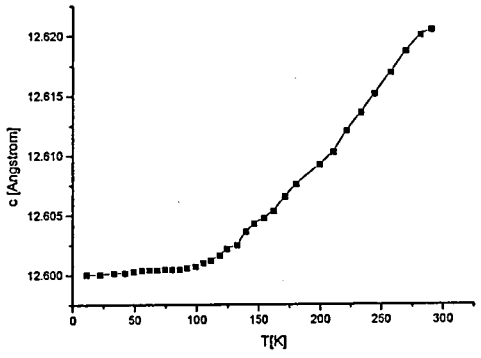

Figure 3.2.6-b

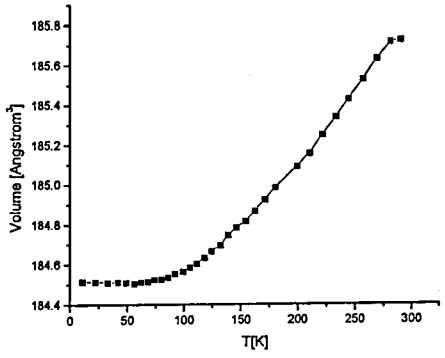

Figure 3.2.6-c

Figure 3.2.6: Temperature variations of the unit cell parameters a) a, b, and b) c axes and c) volume of the Sr_2RuO_4.

c) Structural Characterisation of $CaRuO_3$ with Neutron Diffraction

Neutron data for $CaRuO_3$ has been collected at 2K and 200K at the ILL using the instrument D20. The temperature scans were carried out between 200K and 2K. The same references apply and the same crystallographic models have been used for neutron diffraction refinements as for the X-ray refinements. The results are shown below.

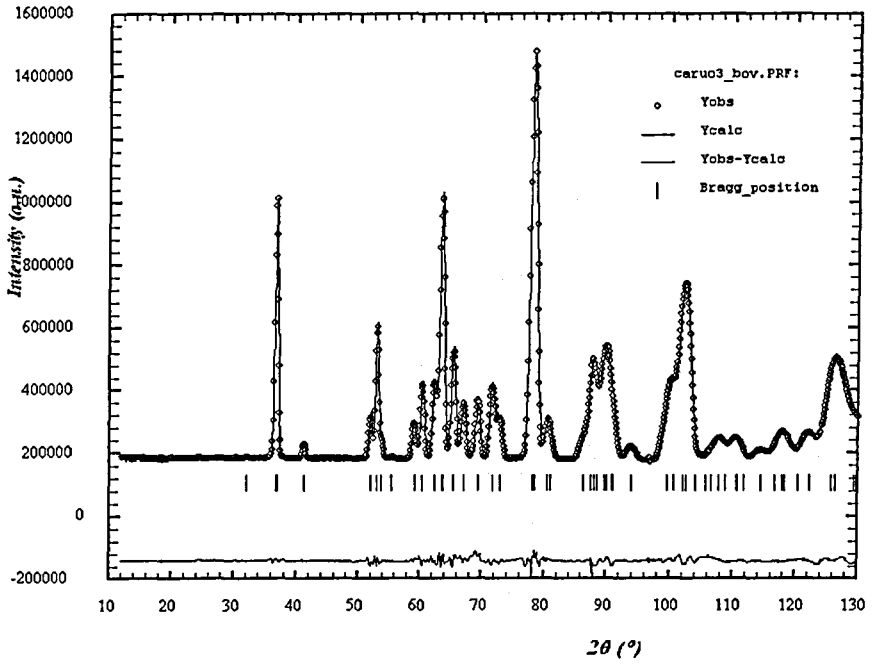

Figure 3.2.7: Observed and refined neutron diffraction patterns of $CaRuO_3$ at 2K

Atom	Wyckoff Notation	Atomic positions for the orthorhombic structure of $CaRuO_3$ using space group *Pnma* [13,20]			Atomic positions the orthorhombic structure of $CaRuO_3$ at 2K using space group *Pnma* after refinement with FullProf [11]		
		x	y	z	x (z)	y (x)	z (y)
Ca	4c	0.0552 (4)	¼	-0.0139 (2)	0.0570 (3)	¼	-0.0154 (6)
Ru	4b	0	0	½	0	0	½
O1	4c	0.4742 (5)	¼	0.0920 (4)	0.4728 (3)	¼	0.0947 (3)
O2	8d	0.2979 (2)	0.0482 (2)	0.6973 (2)	0.2981 (2)	0.0479 (2)	0.6973 (2)

Lattice Parameters [13,20]			Lattice Parameters		
a (Å)	b (Å)	c (Å)	a (Å)	b (Å)	c (Å)
5.5304 (1)	7.8446 (2)	5.5670 (1)	5.4878 (3)	7.5962 (5)	5.3082 (3)
χ^2=2.2			χ^2=103		

Table 3.2.5: Model and refined neutron parameters of $CaRuO_3$ at 2K

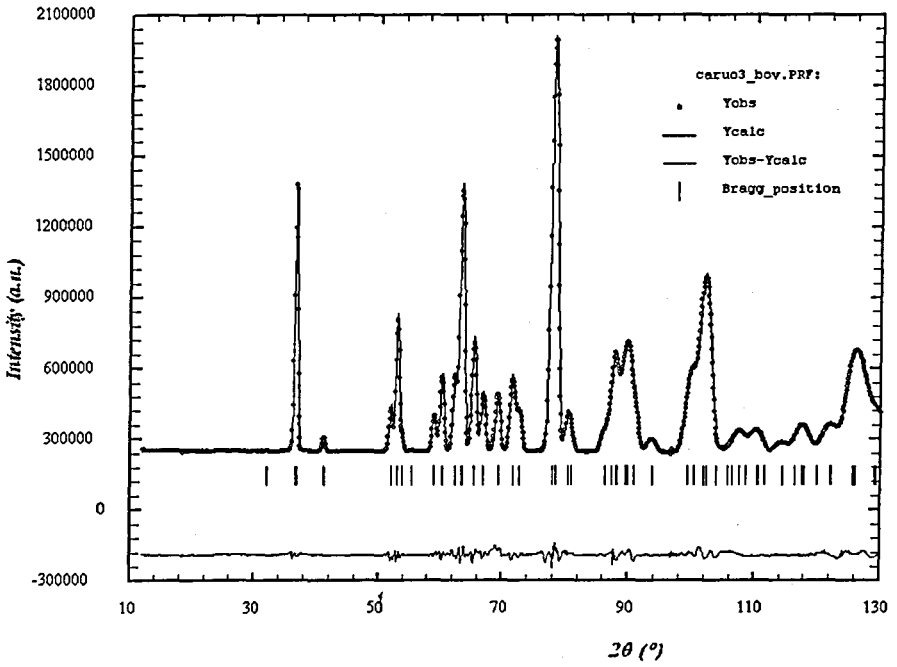

Figure 3.2.8: Observed and refined neutron diffraction patterns of $CaRuO_3$ at 200K

Atom	Wyckoff Notation	Atomic positions for the orthorhombic structure of $CaRuO_3$ using space group *Pnma* [13,20]			Atomic positions for the orthorhombic structure of $CaRuO_3$ at 2K using space group *Pnma* after refinement with FullProf [11]		
		x	y	z	x (z)	y (x)	z (y)
Ca	4c	0.0552 (4)	¼	-0.0139 (2)	0.0553 (3)	¼	-0.0148 (5)
Ru	4b	0	0	½	0	0	½
O1	4c	0.4742 (5)	¼	0.0920 (4)	0.4730 (3)	¼	0.0935 (3)
O2	8d	0.2979 (2)	0.0482 (2)	0.6973 (2)	0.2979 (2)	0.0475 (2)	0.6979 (2)

Lattice Parameters [13,20]			Lattice Parameters		
a (Å)	b (Å)	c (Å)	a (Å)	b (Å)	c (Å)
5.5304 (1)	7.8446 (2)	5.5670 (1)	5.4847 (3)	7.6008 (4)	5.3150 (3)
χ^2=2.2			χ^2=140		

Table 3.2.6: Model and refined neutron parameters of $CaRuO_3$ at 200K

Although the model and the refined parameters (figures 3.2.7, 3.2.8 and tables 3.2.5, 3.2.6) look quite reasonable and the deviations are within the error bars, the obtained χ^2 is large. Systematic errors and the huge counting numbers of observed neutrons affect the value of χ^2. However, the crystallographic data agree well with the model of references [13, 20].

Temperature scans of $CaRuO_3$ were performed between 2K and 200K. The graphs below (figure 3.2.9) show the change of the unit cell parameters against temperature.

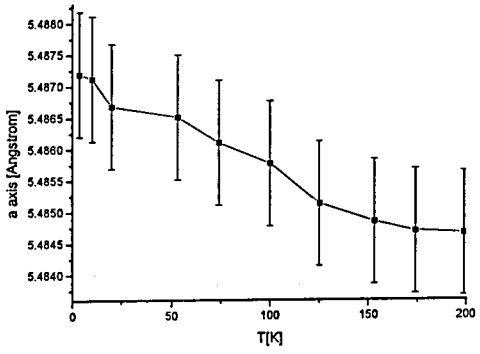

Figure 3.2.9-a

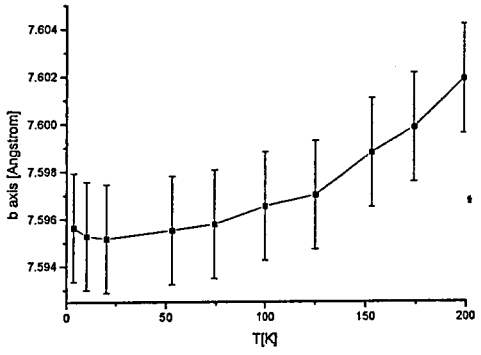

Figure 3.2.9-b

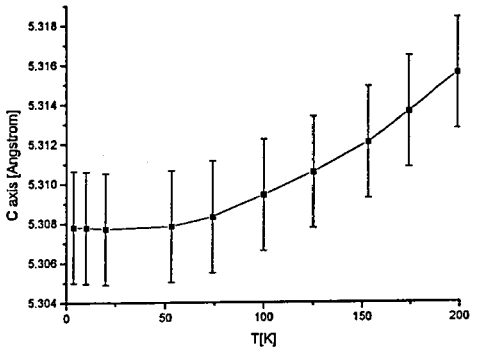

Figure 3.2.9-c

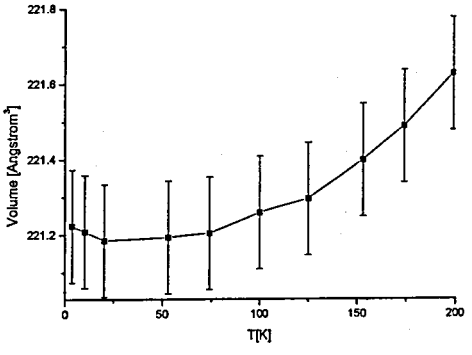

Figure 3.2.9-d

Figure 3.2.9*: Temperature variations of the unit cell parameters a) a-axis, b) b-axis, c) c-axis, and d) volume of the $CaRuO_3$.*

As shown in the figure 3.2.9 the length of the *a*-axis is decreasing while the length of *b* and *c*-axes are increasing (figure 3.2.9-b and 3.2.9-c). Figure 3.2.9-d represents the

change in volume as a function of temperature. These results agree well with those of reference [19]. In the entire temperature range, $CaRuO_3$ has the same crystalline structure, and no discontinuity or anomaly was observed. No evidence has been found for magnetic ordering in these temperature scans.

d) Structural Characterisation of $Sr_xCa_{(1-x)}RuO_3$ using Neutron Diffraction

The compounds $Sr_xCa_{(1-x)}RuO_3$ with x=0.5 and 0.75 have been investigated using the instrument D20 at the ILL within the temperature of 2K to 200K. The thermal expansion of the unit cells of both compounds can be seen in the figures 3.2.12 and 3.1.15. There was no second phase in $Sr_{0.75}Ca_{0.25}RuO_3$. However, $CaRuO_3$ has been detected as a second phase in the compound $Sr_{0.5}Ca_{0.5}RuO_3$. The same crystallographic model was used as for the X-ray refinements. Results are as shown below.

i) $Sr_{0.75}Ca_{0.25}RuO_3$

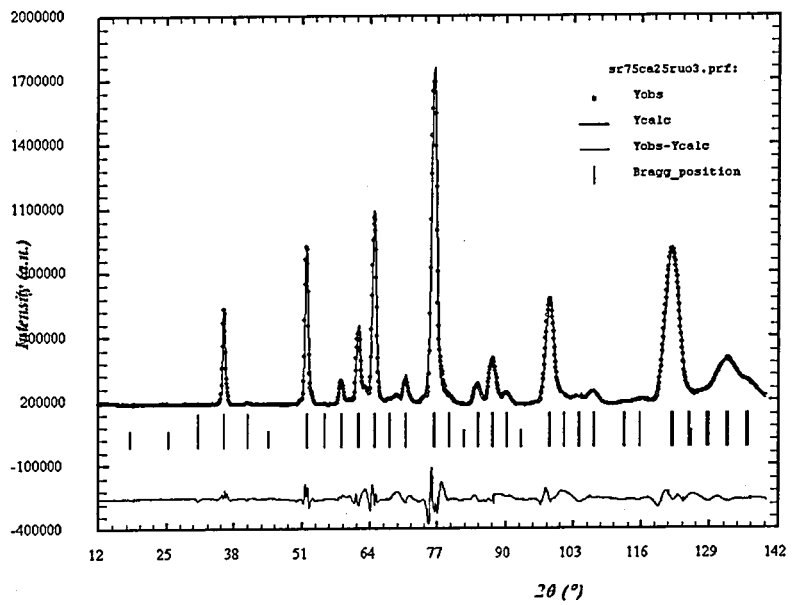

Figure 3.2.10: Observed and refined neutron diffraction pattern of $Sr_{0.75}Ca_{0.25}RuO_3$ at 2K.

Atom	Wyckoff Notation	Atomic positions for the orthorhombic structure of $Sr_{0.75}Ca_{0.25}RuO_3$ using space group *Pnma* [20]			Atomic positions for the orthorhombic structure of $Sr_{0.75}Ca_{0.25}RuO_3$ at 2K using space group *Pnma* after refinement with FullProf [11]		
		x	y	z	x (z)	y (x)	z (y)
Sr	4c	0.0400 (5)	0.25000	-0.009 (1)	0.03 (1)	0.25000	-0.002 (4)
Ca	4c	0.0400 (5)	0.25000	-0.009 (1)	0.03 (1)	0.25000	-0.002 (4)
Ru	4b	0	0	½	0	0	½
O1	4c	0.480 (3)	0.25000	0.0790 (4)	0.488 (2)	0.25000	0.082 (3)
O2	8d	0.296 (2)	0.043 (2)	0.7050 (9)	0.288 (3)	0.023 (1)	0.726 (5)

Lattice Parameters [13,20]			Lattice Parameters		
a (Å)	b (Å)	c (Å)	a (Å)	b (Å)	c (Å)
5.5128 (2)	7.7392 (3)	5.4444 (2)	5.495 (1)	7.769 (2)	5.485 (2)
χ^2=2.2			χ^2=800		

Table 3.2.7: Refined parameters of $Sr_{0.75}Ca_{0.25}RuO_3$ at 2K

The refined parameters (table 3.2.7) and fit (figure 3.2.10) agree well with the model of reference [20]. Although the χ^2 looks high with a value of 800, the Bragg R-Factor and the RF-Factor is quite small with the values of 2.75 and 2.029 respectively. The obtained magnetisation with FullProf is 0.086(±0.254) μ_B/Ru. The value of the deviation (0.254) is about 3 times higher than the observed value of 0.086. In this case, it is not possible to talk about magnetic ordering for the $Sr_{0.75}Ca_{0.25}RuO_3$ at 2K. A detailed investigation will be performed in the magnetic investigation section to see whether there is magnetic ordering or not.

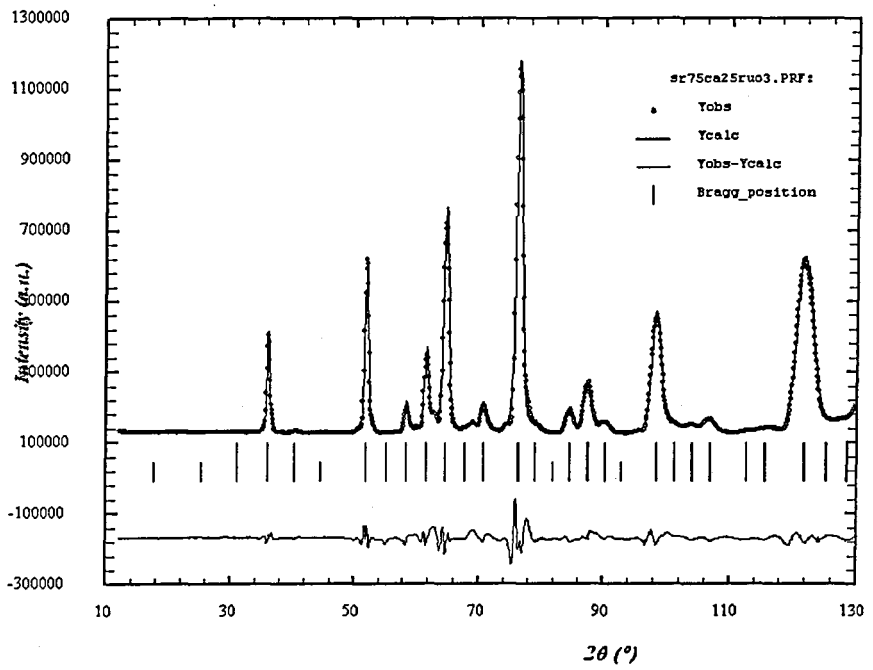

Figure 3.2.11: Observed and refined neutron diffraction pattern of $Sr_{0.75}Ca_{0.25}RuO_3$ at 200K

Atom	Wyckoff Notation	Atomic positions for the orthorhombic structure of $Sr_{0.75}Ca_{0.25}RuO_3$ using space group *Pnma* [20]			Atomic positions for the orthorhombic structure of $Sr_{0.75}Ca_{0.25}RuO_3$ at 200K using space group *Pnma* after refinement with FullProf [11]		
		x	y	z	x (z)	y (x)	z (y)
Sr	4c	0.0400 (5)	0.25000	-0.009 (1)	0.014 (1)	0.25000	0.029 (3)
Ca	4c	0.0400 (5)	0.25000	-0.009 (1)	0.014 (1)	0.25000	0.029 (3)
Ru	4b	0	0	½	0	0	½
O1	4c	0.480 (3)	0.25000	0.079 (4)	0.476 (2)	0.25000	0.028 (4)
O2	8d	0.296 (2)	0.043 (2)	0.705 (9)	0.297 (1)	0.0394 (7)	0.734 (3)

Lattice Parameters [13,20]			Lattice Parameters		
a (Å)	b (Å)	c (Å)	a (Å)	b (Å)	c (Å)
5.5128 (2)	7.7392 (3)	5.4444 (2)	5.497 (2)	7.765 (2)	5.4951 (3)
χ^2=5.9			χ^2=470		

Table 3.2.8: Refined neutron parameters of $Sr_{0.75}Ca_{0.25}RuO_3$ at 200K

As seen above, figure 3.2.11 represents a good fit and the refined model (table 3.2.8) is very close to the model proposed in the literature [20]. The χ^2 value is a large number, namely 470. However the Brag R-Factor and the RF-Factor are reasonable. No ordered magnetic moment has been found at 200K. This is consistent with magnetisation measurements.

Temperature scan results can be seen below in figure 3.2.12. The temperature dependence of the unit cell parameters shows the thermal expansion of $Sr_{0.75}Ca_{0.25}RuO_3$.

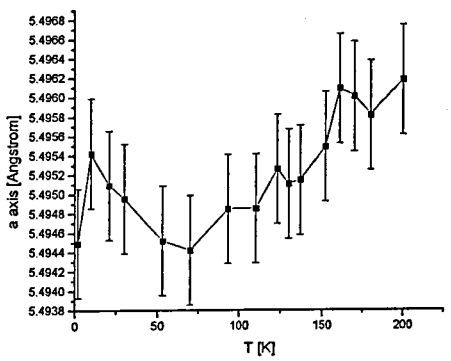

Figure 3.2.12-a

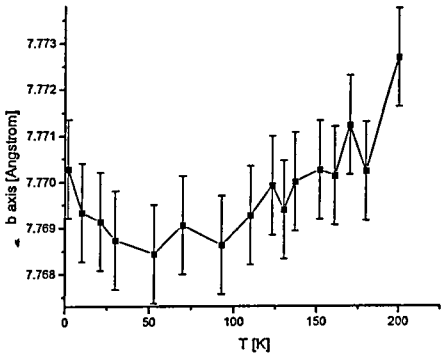

Figure 3.2.12-b

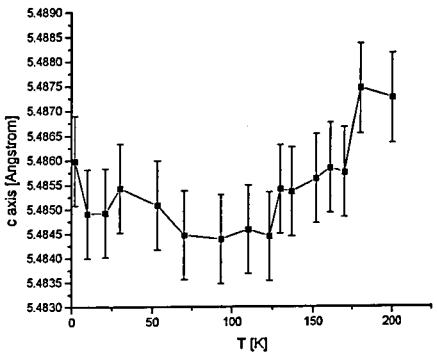

Figure 3.2.12-c

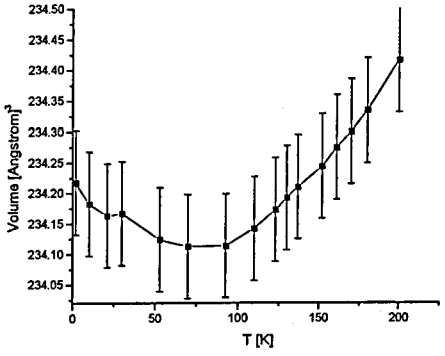

Figure 3.2.12-d

Figure 3.2.12: Unit cell parameters as a function of increasing temperature for $Sr_{0.75}Ca_{0.25}RuO_3$. a) a-axis, b) b-axis, c) c-axis and d) Volume

ii) $Sr_{0.5}Ca_{0.5}RuO_3$

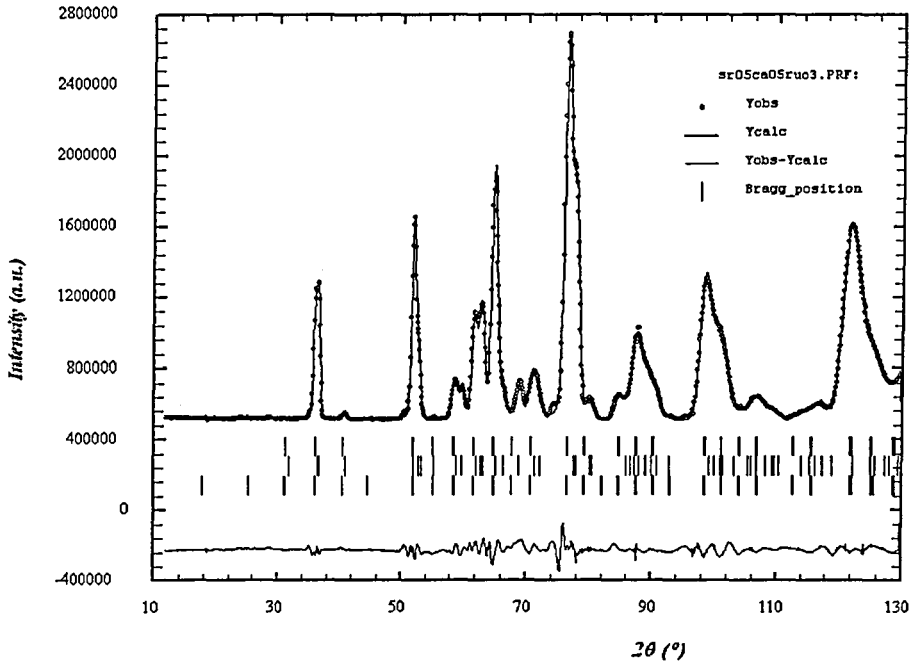

Figure 3.2.13: Observed and refined neutron diffraction patterns of $Sr_{0.5}Ca_{025}RuO_3$ at 2K.

Atom	Wyckoff Notation	Atomic positions for the orthorhombic structure of $Sr_{0.5}Ca_{0.5}RuO_3$ at 2K using space group *Pnma* [20]			Atomic positions for the orthorhombic structure of $Sr_{0.5}Ca_{0.5}RuO_3$ at 2K using space group *Pnma* after refinement with FullProf		
		x	y	z	x (z)	y (x)	z (y)
Sr	4c	0.0337 (7)	0.25000	-0.006 (2)	-0.006 (2)	0.25000	-0.003 (3)
Ca	4c	0.0337 (7)	0.25000	-0.006 (2)	-0.006 (2)	0.25000	-0.003 (3)
Ru	4b	0	0	½	0	0	½
O1	4c	0.488 (4)	0.25000	0.084 (9)	0.510 (2)	0.25000	0.114 (4)
O2	8d	0.294 (3)	0.031 (4)	0.711 (5)	0.2994 (8)	0.0317 (5)	0.792 (3)

Lattice Parameters [13,20]			Lattice Parameters [11]		
a (Å)	b (Å)	c (Å)	a (Å)	b (Å)	c (Å)
5.5136 (4)	7.7921 (6)	5.4932 (4)	5.4947 (7)	7.770 (1)	5.485 (2)
χ^2=5.9			χ^2=418		

Table 3.2.9: Refined neutron parameters of the first phase of $Sr_{0.75}Ca_{0.25}RuO_3$ at 2K

Atom	Wyckoff Notation	Atomic position for the orthorhombic structure of $CaRuO_3$ at 2K using space group *Pnma* [20]			Atomic position for the orthorhombic structure of $CaRuO_3$ using space group *Pnma* after refinement with FullProf [11]		
		x	y	z	x (z)	y (x)	z (y)
Ca	4c	0.0552 (4)	¼	-0.0139 (2)	0.055 (1)	¼	-0.003 (2)
Ru	4b	0	0	½	0	0	½
O1	4c	0.4742 (5)	¼	0.0920 (4)	0.467 (2)	¼	0.081 (2)
O2	8d	0.2979 (2)	0.0482 (2)	0.6973 (2)	0.294 (8)	0.0504 (6)	0.6979 (8)

Lattice Parameters [13,20]			Lattice Parameters		
a (Å)	b (Å)	c (Å)	a (Å)	b (Å)	c (Å)
5.5304 (1)	7.8446 (2)	5.5670 (1)	5.481 (1)	7.644 (2)	5.356 (1)
χ^2=5.9			χ^2=418		

Table 3.2.10: Refined neutron parameters of the second phase of $Sr_{0.75}Ca_{0.25}RuO_3$ at 2K

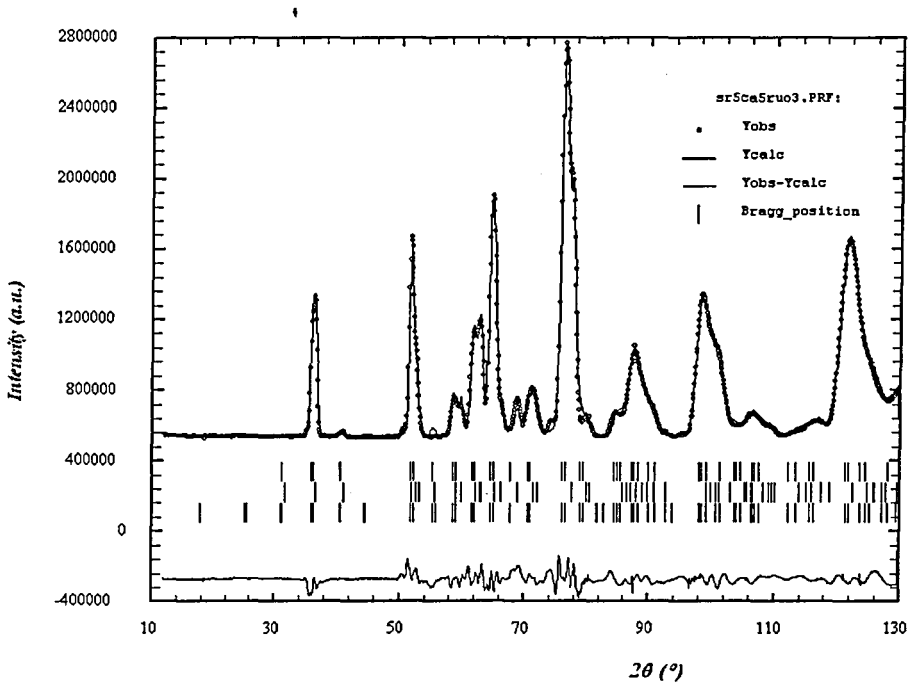

Figure 3.2.14: Observed and refined neutron diffraction pattern of $Sr_{0.5}Ca_{025}RuO_3$ at 200K

Atom	Wyckoff Notation	Atomic positions for the orthorhombic structure of $Sr_{0.5}Ca_{0.5}RuO_3$ at 200K using space group *Pnma* [20]			Atomic positions for the orthorhombic structure of $Sr_{0.5}Ca_{0.5}RuO_3$ at 200K using space group *Pnma* after refinement with FullProf [11]		
		x	y	z	x (z)	y (x)	z (y)
Sr	4c	0.0337 (7)	0.25000	-0.006 (2)	-0.019 (2)	0.25000	-0.007 (2)
Ca	4c	0.0337 (7)	0.25000	-0.006 (2)	-0.019 (2)	0.25000	-0.007 (2)
Ru	4b	0	0	½	0	0	½
O1	4c	0.488 (4)	0.25000	0.084 (9)	0.513 (2)	0.25000	0.073 (3)
O2	8d	0.294 (3)	0.031 (4)	0.711 (5)	0.2980 (8)	0.0343 (6)	0.743 (3)

Lattice Parameters [13,20]			Lattice Parameters		
a (Å)	b (Å)	c (Å)	a (Å)	b (Å)	c (Å)
5.5136(4)	7.7921(6)	5.4932(4)	5.5073 (8)	7.791 (1)	5.446 (2)
χ^2=5.9			χ^2=743		

Table 3.2.11: Refined neutron parameters of the first phase of $Sr_{0.75}Ca_{0.25}RuO_3$ at 200K

Atom	Wyckoff Notation	Atomic position for the orthorhombic structure of $CaRuO_3$ at 200K using space group *Pnma* [13,20]			Atomic position for the orthorhombic structure of $CaRuO_3$ at 200K using space group *Pnma* after refinement with FullProf [11]		
		x	y	z	x (z)	y (x)	z (y)
Ca	4c	0.0552 (4)	¼	-0.0139 (2)	0.045 (2)	¼	-0.011 (3)
Ru	4b	0	0	½	0	0	½
O1	4c	0.4742 (5)	¼	0.0920 (4)	0.466 (2)	¼	0.086 (2)
O2	8d	0.2979 (2)	0.0482 (2)	0.6973 (2)	0.298 (1)	0.0469 (9)	0.695 (1)

Lattice Parameters [13,20]			Lattice Parameters		
a (Å)	b (Å)	c (Å)	a (Å)	b (Å)	c (Å)
5.5304 (1)	7.8446 (2)	5.5670 (1)	5.478 (1)	7.659 (2)	5.365 (3)
χ^2=5.9			χ^2=743		

Table 3.2.12: Refined neutron parameters of the second phase of $Sr_{0.75}Ca_{0.25}RuO_3$ at 2K

The correct crystallographic structure parameters were not obtained with a single phase refinement for $Sr_{0.5}Ca_{0.5}RuO_3$. Due to the problems of refinement different models have been tried to find the best fit. The best fit and best result was obtained when two phases ($Sr_{0.75}Ca_{0.25}RuO_3$ and $CaRuO_3$) were applied to the refinement of the neutron data. According this model, there is a second phase present of composition $CaRuO_3$ accompanying $Sr_{0.5}Ca_{0.5}RuO_3$. The refined data and fitted plots can be seen in figures 3.2.13, 3.2.14 and tables 3.2.9, 3.2.10, 3.2.11, 3.2.12. The ratio of the compounds

$Sr_{0.5}Ca_{0.5}RuO_3$ / $CaRuO_3$ is 0.867. This ratio is close to the one which was obtained using X-ray diffraction. The reason for the impurity might be due to insufficient mixing of the compound when sintering, not enough heat treatment or not applying the right pressure when making pellets.

Although the χ^2 value obtained is high for 2K and 200K (418, 743 respectively) the neutron diffraction patterns give better results than the X-ray diffraction patterns. When the magnetic part is refined, the value of χ^2 starts fluctuating and does not become stable. The reason is the second phase. The space group of second phase compound $CaRuO_3$ and $Sr_{0.75}Ca_{0.75}RuO_3$ are the same as the ones mentioned in X-ray diffraction section and it is *Pnma* (#62). The lattice parameters of the two compounds are close enough for overlap. Thus the two phases render the data not refineable with the magnetic phase.

The figure 3.2.15 below shows the thermal expansion of the unit cell of $Sr_{0.5}Ca_{0.5}RuO_3$. The data of the temperature scan has been collected between 2K and 200K.

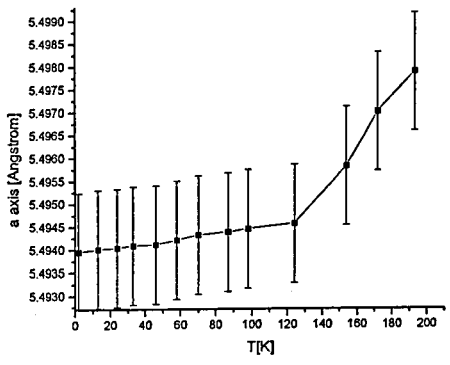

Figure 3.2.15-a

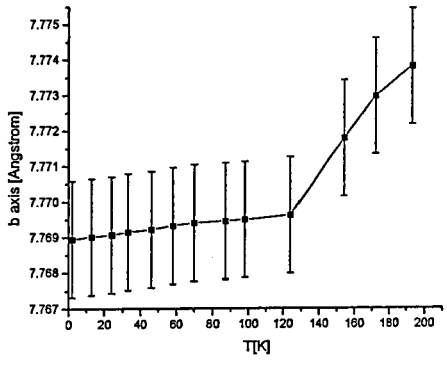

Figure 3.2.155-b

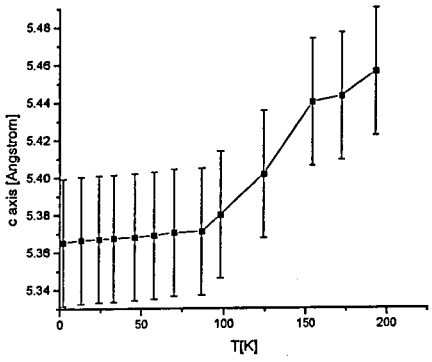

Figure 3.2.15-c

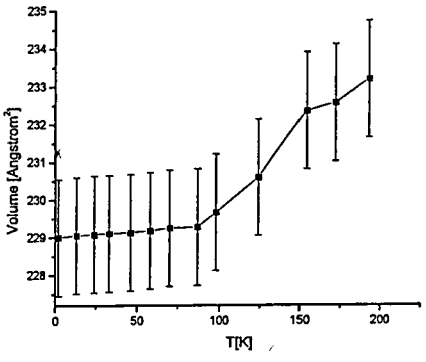

Figure 3.2.15-d

Figure 3.2.15: *Thermal expansion of the unit cells of $Sr_{0.5}Ca_{0.5}RuO_3$ a) a-axis, b) b-axis, c) c-axis and d) unit cell volume of $Sr_{0.5}Ca_{0.5}RuO_3$*

Figure 3.2.15 clearly exhibits the thermal expansion of the unit cell and volume of the $Sr_{0.5}Ca_{0.5}RuO_3$ compound.

3.3 Magnetic Investigation

A superconducting Quantum Interface Device, SQUID for short, was used to measure the magnetic properties of the $Sr_{(1-x)}Ca_xRuO_3$ and Sr_2RuO_4 compounds. The device is widely accepted as the most accurate method of measuring magnetic moments. The resolution of 10^{-8} e.m.u. (10^{-11} JT^{-1}) allows accurate measurements of samples with small magnetic moments. This highly sensitive method was sufficient to investigate the magnetic properties of the Ruthenates.

A small piece of the ruthenate compounds (table 3.3.1) was placed inside a gelatine capsule with a very small amount of cotton wool for fixing the sample into position. The capsule was then placed in a plastic tube and connected to the sample transport mechanism. All samples were cooled down to 5K in zero field.

Samples	Weight [g]	Relative atomic mass [g/mol]	Number of Mole [mole]
$SrRuO_3$	0.00200±0.00001	236.87	(8.4434±0.0001) 10^{-6}
$CaRuO_3$	0.01610±0.00001	189.15	(8.5118±0.0001) 10^{-5}
$Sr_{0.75}Ca_{0.25}RuO_3$	0.00900±0.00001	224.80	(4.0036±0.0001) 10^{-5}
$Sr_{0.5}Ca_{0.5}RuO_3$	0.00795±0.00001	212.92	(3.7338±0.0001) 10^{-5}
Sr_2RuO_4	0.01031±0.00001	308.31	(3.3440±0.0001) 10^{-5}

Table 3.3.1: Weight, relative atomic mass and number of mole of samples used

The magnetisation measurements for the polycrystalline samples were carried out in two different ways. First of all the magnetisation was measured as a function of temperature in various constant external fields. Secondly, the magnetisation was measured as a function of applied field at constant temperature. From the latter measurements Arrott plots were created for different temperatures. The MPMS-SQUID system created a data file including temperature values in Kelvin, applied magnetic field in Gauss, magnetic

moment in e.m.u. and magnetic susceptibility in e.m.u./gauss. These data were converted into SI-units and normalized to the mass of the sample.

3.3.1. $SrRuO_3$

A magnetic measurement in various constant applied magnetic fields of 0.1, 1.25, 2, 5 Tesla has been carried out over the temperature range from 5K to 360K. The results are shown in figure 3.3.1

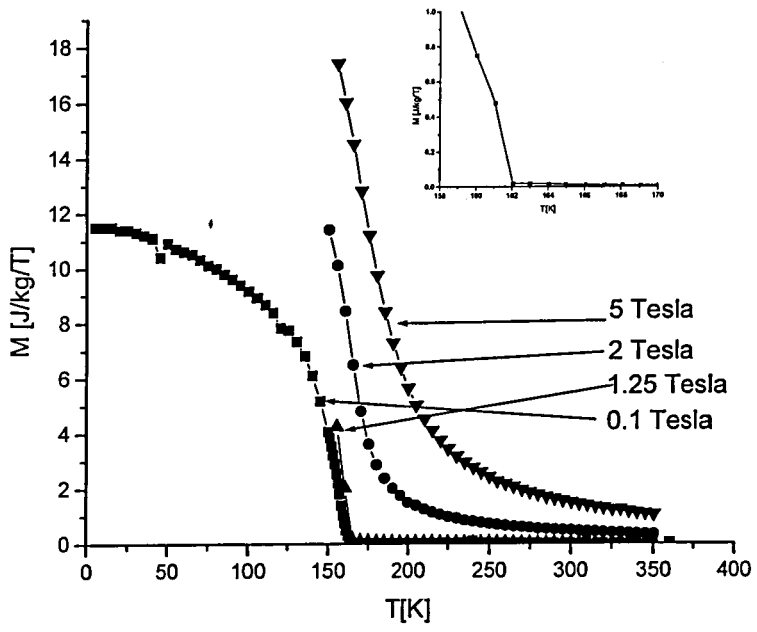

Figure 3.3.1: Magnetisation of $SrRuO_3$ as a function of temperature at an applied magnetic fields of 0.1,1.25, 2, 5 Tesla.

The low field (0.1 and 1.25 Tesla) magnetisation measurements clearly indicate that the $SrRuO_3$ compound is ferromagnetic (figure 3.3.1). The transition temperature for $SrRuO_3$ is 162K as might be seen in the inset figure of figure 3.3.1. In general, the magnetisation increases with increasing magnetic field.

The magnetisation of $SrRuO_3$ was measured as a function of applied field for various temperatures (figure 3.3.2). The ordered magnetic moment is increasing with decreasing

temperature. The magnetisation measurements which are below the Curie temperature have an intersection with the positive *y*-axis (*M*).

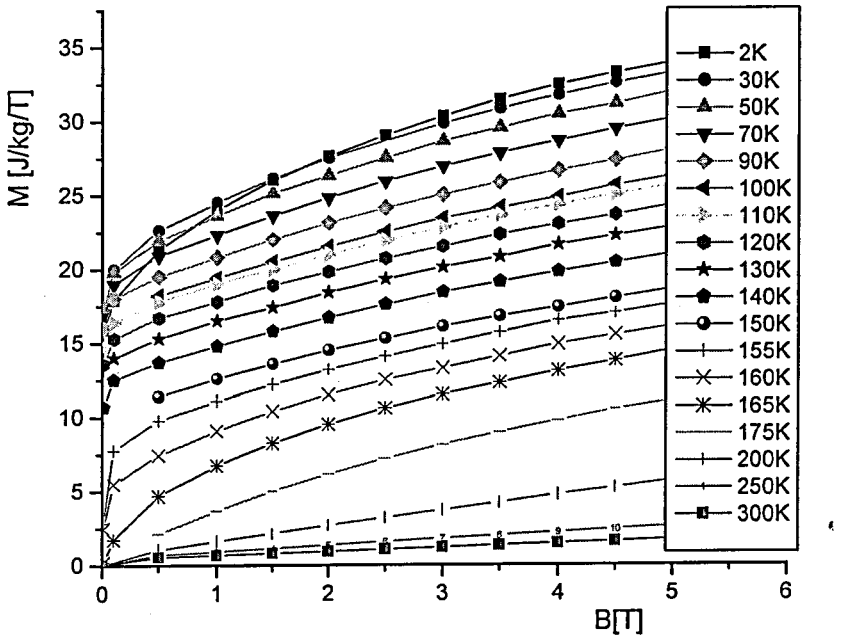

Graph 3.3.2: Magnetisation of $SrRuO_3$ as a function of applied magnetic field at various temperatures.

Arrott plots are more useful for investigating the magnetic properties. Using the data of the magnetic measurements Arrott plots are plotted for various isothermal measurements and the results are represented in figures 3.3.3, 3.3.4, 3.3.5

In figure 3.3.3 Arrott plots of $SrRuO_3$ clearly represent the magnetic phase transition. $SrRuO_3$ shows ferromagnetic behaviour for the temperatures which intersect the y-axis (M^2) and it shows paramagnetic behaviour for the temperatures which intersect with the x-axis (*H/M*). A zoomed view of the Arrott plots can be seen in the figure 3.3.5. In graph 3.3.5, the intersection with the x-axis (*H/M* axis) yields values of the inverse magnetic susceptibility extrapolated to zero applied magnetic fields.

In the figure 3.3.6 the inverse susceptibility is shown as a function of temperature. For temperatures above the transition point of 162 Kelvin the inverse susceptibility versus temperature is in excellent agreement with the Curie Weiss law as shown in graph 3.3.6.

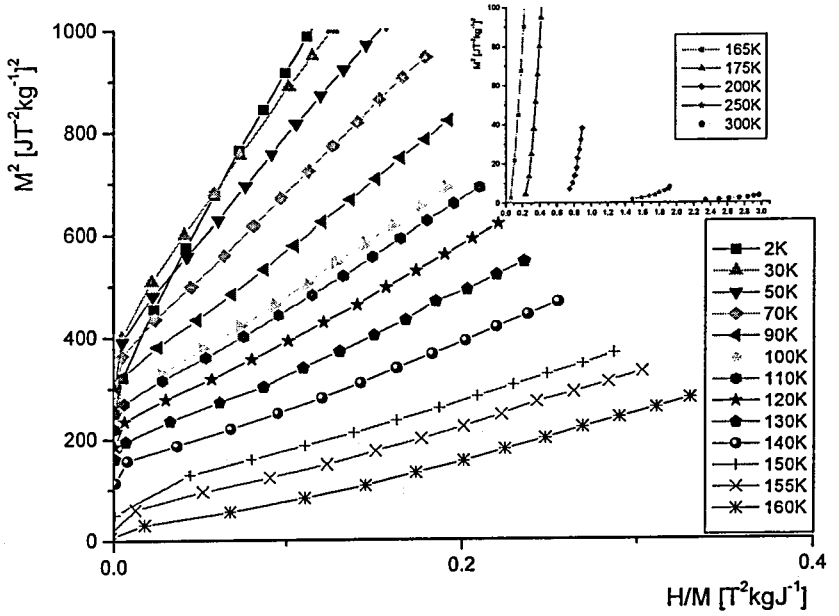

Figure 3.3.3: Arrott plots of $SrRuO_3$. The inset figure shows the Arrott plots for which the linear extrapolations intersect with the x-axis.

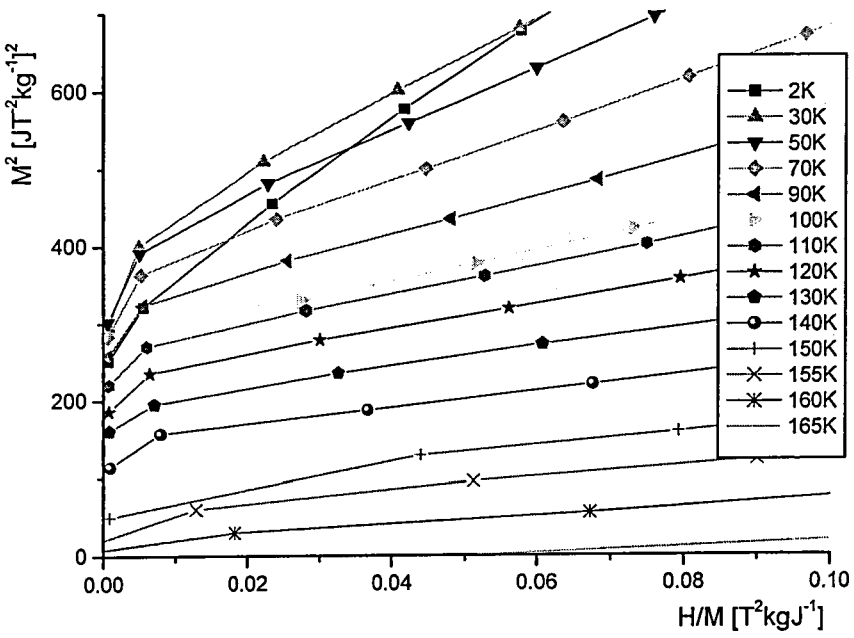

Figure *3.3.4: Zoomed view of Arrott plots of $SrRuO_3$*

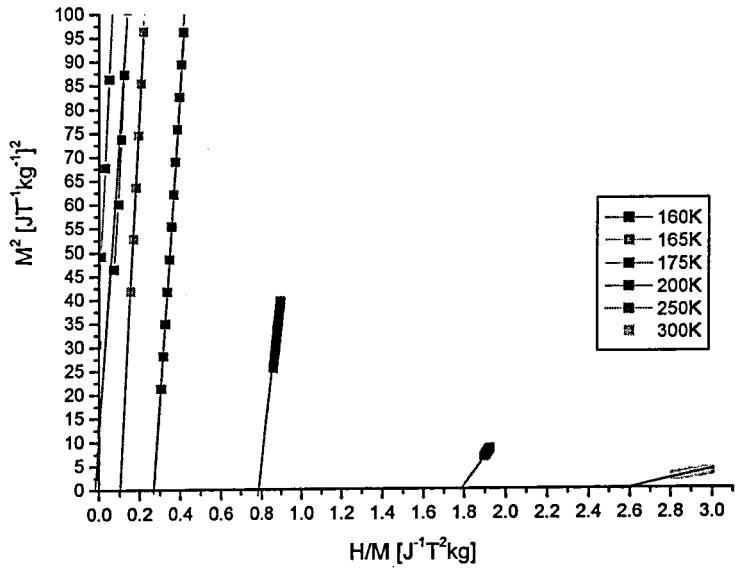

Figure 3.3.5: A more detailed view of the paramagnetic region containing the linear fit of Arrott plots for $SrRuO_3$. All values are interpolated to the x or y axes.

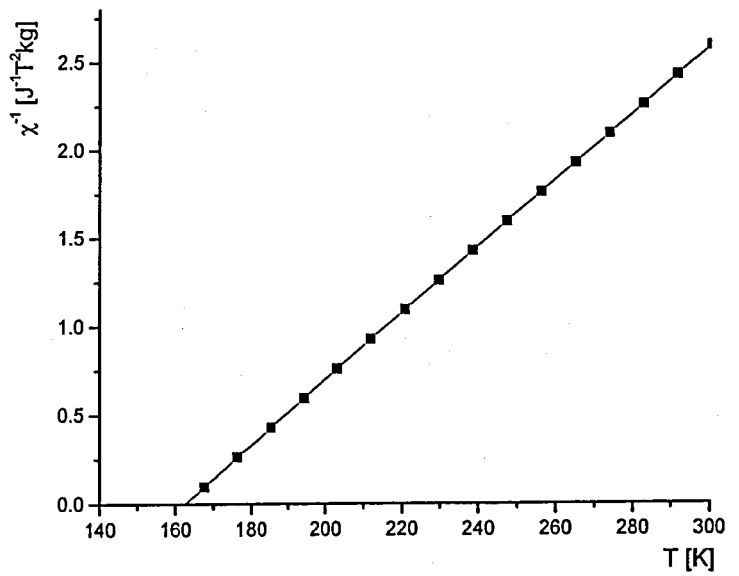

Figure 3.3.6: Inverse mass susceptibility as a function of temperature of $SrRuO_3$. This graph is obtained from Arrott plots.

The intersection point with the x-axis indicates that the paramagnetic Curie temperature for $SrRuO_3$ is 162K.

As described in the theory section 2.3.2, the paramagnetic effective Bohr magneton number per Ru-atom could be calculated from the slope of the inverse susceptibility. According to the calculations the value of paramagnetic effective Bohr magneton number has been found experimentally as 3.17(±0.12) μ_B per Ruthenium. The paramagnetic effective Bohr magneton number for $SrRuO_3$ is calculated 2.81(±0.09) μ_B/Ru in low spin state (s=1) in reference [29]. The obtained value by experiment is slightly higher than the reference value.

3.2.2. $CaRuO_3$

For the compound $CaRuO_3$ magnetisation measurements have been carried out as a function of temperature over a range of 2K to 280K at a field of 0.1 Tesla. The curve obtained is shown in figure 3.3.7

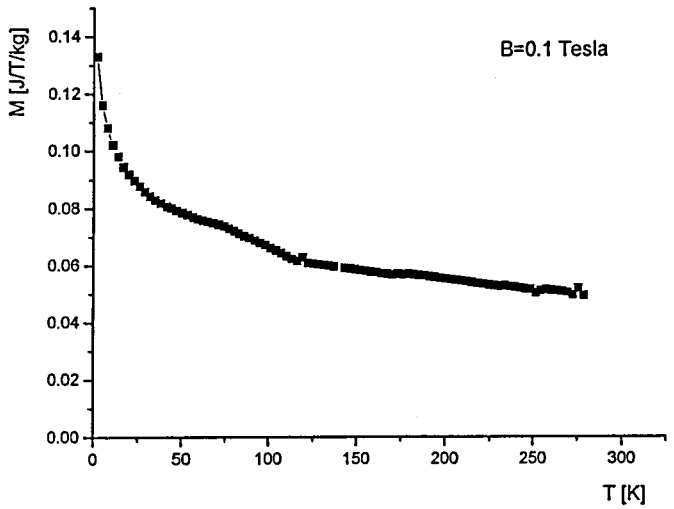

Figure 3.3.7: Magnetisation as a function of temperature at an applied magnetic field of 0.1 Tesla for $CaRuO_3$

As seen in the figure 3.3.7 there is no magnetic anomaly within this temperature range. The magnetisation increases with decreasing temperature in a low field 0.1 Tesla and reaches its maximum value of 0.13 $JT^{-1}kg^{-1}$ at 2K.

Magnetic isotherms of $CaRuO_3$ were measured for various temperatures (figure 3.3.8). All the graphs indicate a linear dependence of the magnetisation on the applied field and all go through the origin of the graph. Again, no magnetic phase transition has been observed over the whole temperature range.

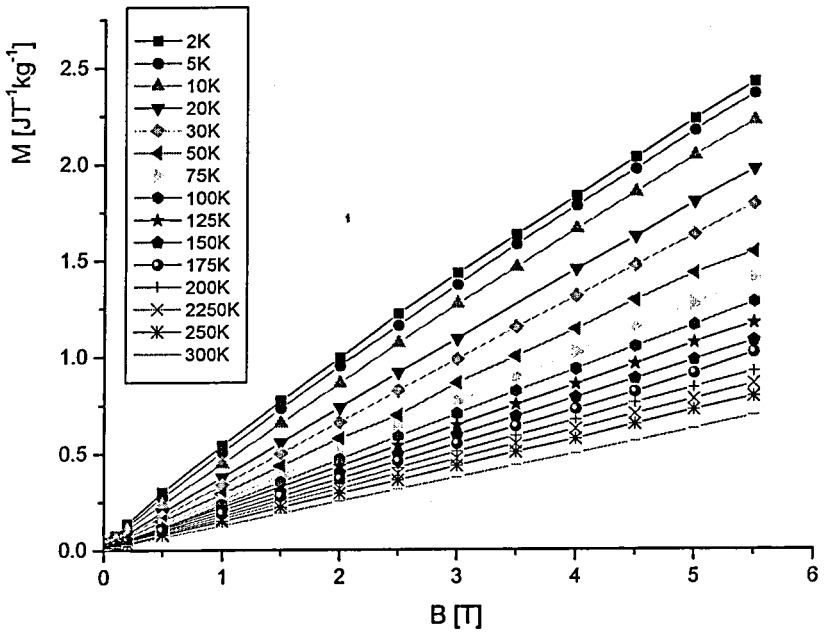

Figure 3.3.8: Magnetisation of $CaRuO_3$ as a function of applied magnetic field at various temperatures

Arrott plots have been obtained for a more detailed magnetic investigation (figure 3.3.9). There is no intersection with the y-axis (M^2 axis) for any temperature. All the fitted values (figure 3.3.10) of Arrott plots intersect with the x-axis (H/M axis). It is pointed out that the compound $CaRuO_3$ is paramagnetic within the whole temperature range of 2K to 300K.

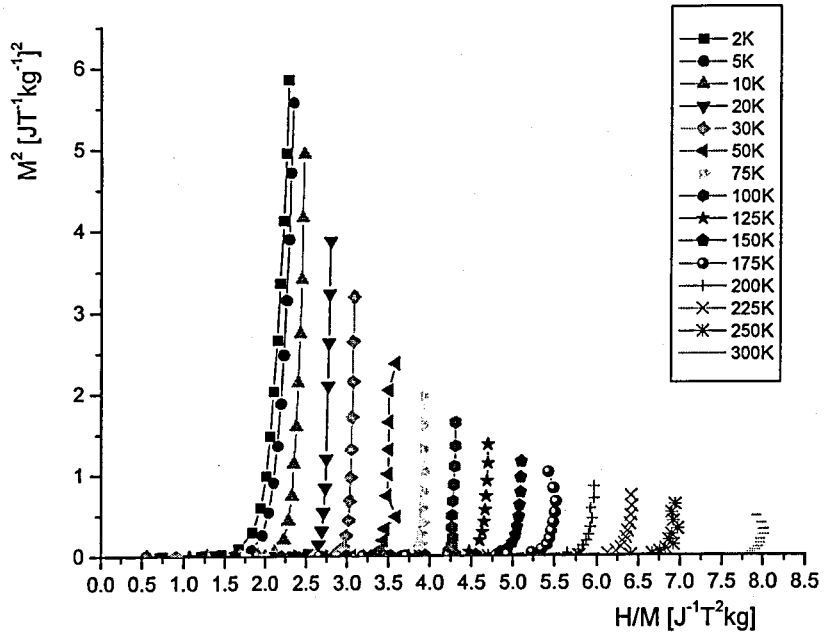

Figure 3.3.9: Arrott plots of $CaRuO_3$ at various temperatures

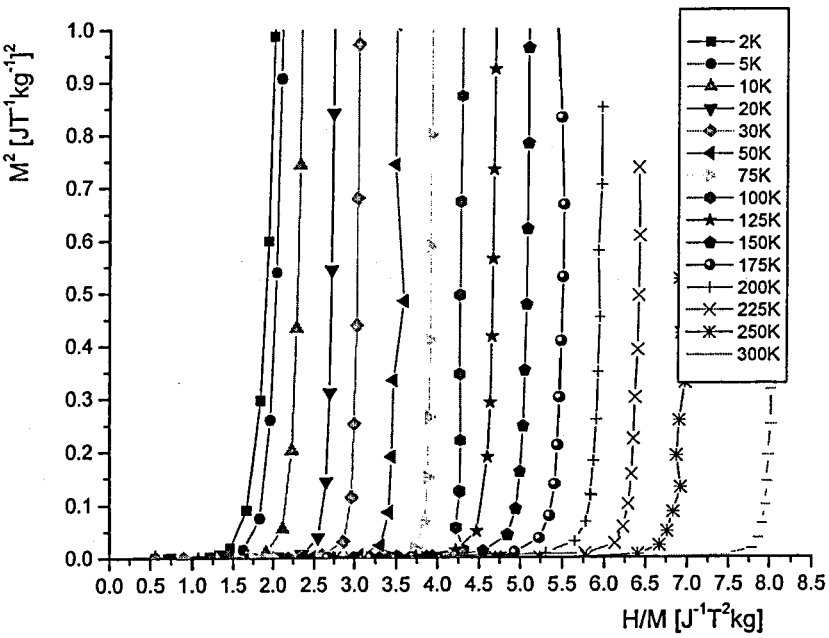

Figure 3.3.10: Zoomed view of Arrott plots of $CaRuO_3$.

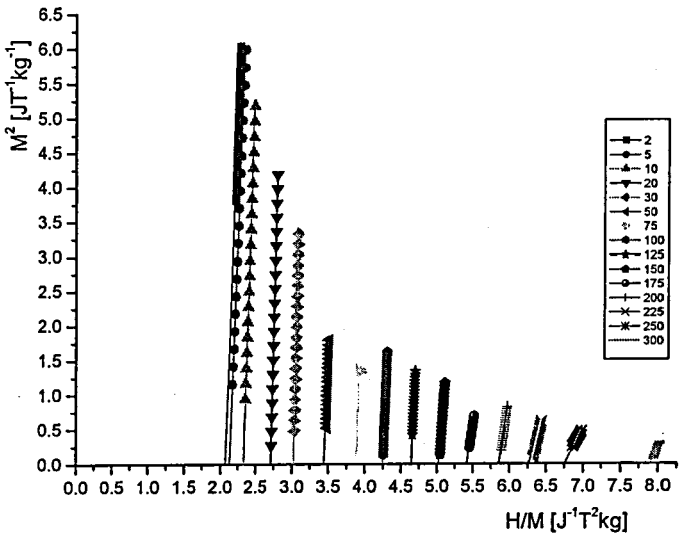

Figure 3.3.11: Linear fit of Arrott plots of $CaRuO_3$. All values intersect the x-axis (H/M axis)

Arrott plots are used to obtain values for the magnetic susceptibility by the fitting of linear lines. The temperature dependence of the inverse susceptibility is plotted in figure 3.3.12.

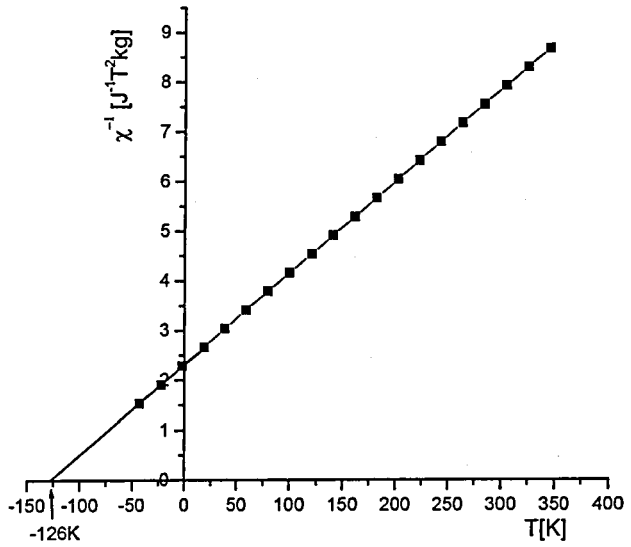

Figure 3.3.12: Inverse magnetic susceptibility as a function of temperature of $CaRuO_3$.

The inverse magnetic susceptibility against temperature graph is in good agreement with the model of a Curie-Weiss law. From figure 3.3.12 it can be seen that the paramagnetic Curie temperature for $CaRuO_3$ is -126(±1.8) K. The slope of this graph yields a paramagnetic effective Bohr magneton value for the paramagnetic moment of $CaRuO_3$ of 2.867(±0.12) μ_B/Ru atom. In reference [29] the paramagnetic effective Bohr magneton is found as 2.66 μ_B/Ru atom. The obtained paramagnetic effective Bohr magneton from SQUID measurements is quite close the one given in reference [29].

3.3.3. Sr_2RuO_4

It is well known that Sr_2RuO_4 is the first noncuprate layered perovskite compound [16, 31]. Magnetisation against temperature has been measured for Sr_2RuO_4 in an applied field of 0.1 Tesla (figure 3.3.13). In the literature [16, 31] it is claimed that the compound does not order magnetically down to 1K but shows superconductivity around ~1.2K. The small magnitude of the magnetisation in figure 3.3.13 arises from an impurity phase $SrRuO_3$. The amount of Sr_2RuO_4 used for this investigation was 3.21×10^{-3} grams and the amount of $SrRuO_3$ has been calculated to be of the order of 10^{-5} grams which is about one per cent compared to the mass of Sr_2RuO_4. This impurity is so small that it cannot be detected in X-ray diffraction or neutron scattering, on the other hand, it is sufficiently large for causing an effect in magnetic measurements. There is no magnetic phase transition or magnetic ordering detected within the measured temperature range.

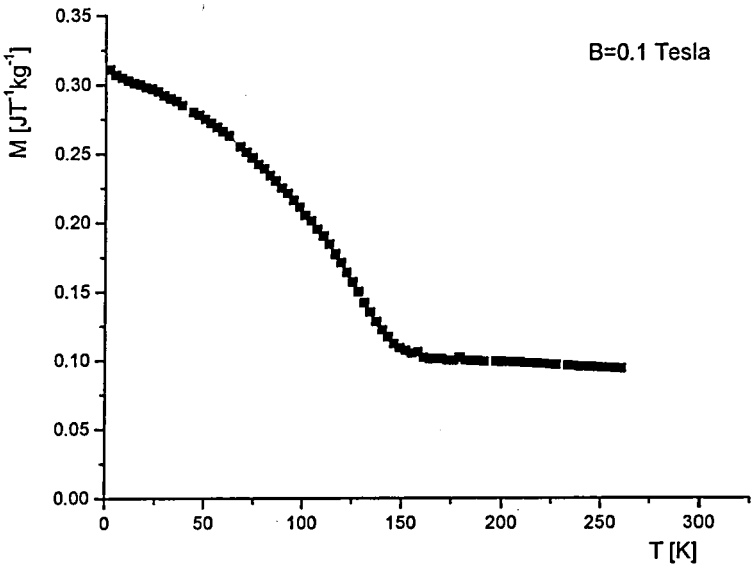

Figure 3.3.13: Magnetisation as a function of temperature at an applied magnetic field of 0.1 Tesla for Sr_2RuO_4

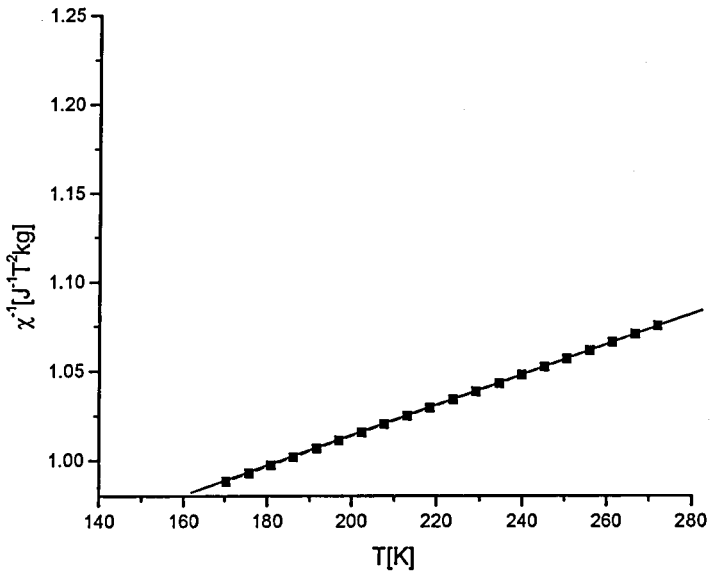

Figure 3.3.14: Inverse mass susceptibility as a function of temperature of Sr_2RuO_4. This graph is obtained from magnetisation against temperature graph.

The inverse mass susceptibility of Sr_2RuO_4 can be seen in graph 3.3.14. However, again, the impurity phase, $SrRuO_3$, plays a role in this graph and due to its presence the graph does not go through the origin and shows a phase transition at $T_C = 162$ K.

3.3.4. $Sr_{(1-x)}Ca_xRuO_3$

a) $Sr_{0.75}Ca_{0.25}RuO_3$

A magnetic measurement in a constant applied magnetic field of 0.1 Tesla has been carried out over the temperature range from 5K to 350K. For $Sr_{0.75}Ca_{0.25}RuO_3$ the results are shown in figure 3.3.15

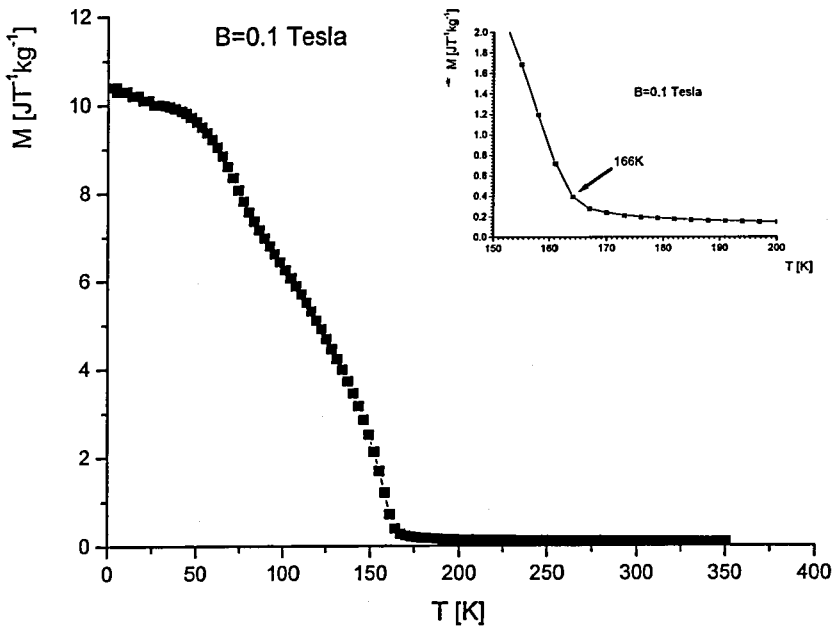

Figure 3.3.15: Magnetisation as a function of temperature at an applied magnetic field of 0.1 Tesla for $Sr_{0.75}Ca_{0.25}RuO_3$

This magnetisation measurement in an applied field of 0.1 Tesla (figure 3.3.15) clearly indicates that $Sr_{0.75}Ca_{0.25}RuO_3$ is ferromagnetic. The inset figure in figure 3.3.15 shows the transition temperature for $Sr_{0.75}Ca_{0.25}RuO_3$ and the magnetic phase transition

temperature for this compound is 166(±1.6)K. This value should be smaller than the value of inverse susceptibility of $SrRuO_3$.

The magnetisation of $Sr_{0.75}Ca_{0.25}RuO_3$ was measured for various temperatures (figure 3.3.16). The magnetisation increases with increasing field and decreasing temperature. For measurements which are below the transition temperatures (T_C) the extrapolations to low fields intersect with the y-axis (M). For measurements at temperatures above the transition temperatures, the graphs pass through the origin.

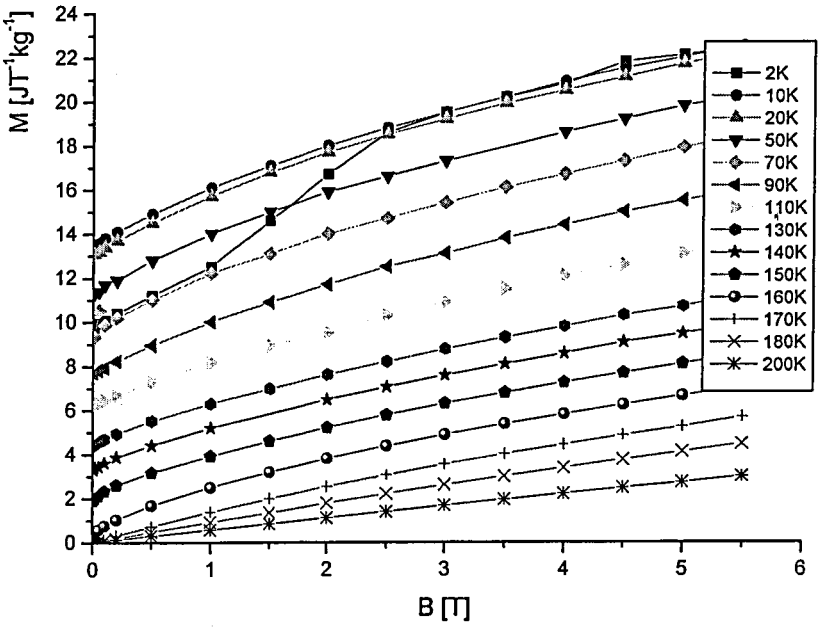

Figure 3.3.16: Magnetisation of $Sr_{0.75}Ca_{0.25}RuO_3$ as a function of applied magnetic field at various temperatures

Again here, Arrott plots have been used for investigating the magnetic properties and also to help to plot the inverse susceptibility against temperature. Using the data of the magnetic isotherm measurements Arrott plots were plotted for various temperatures and the results are represented in figure 3.3.17.

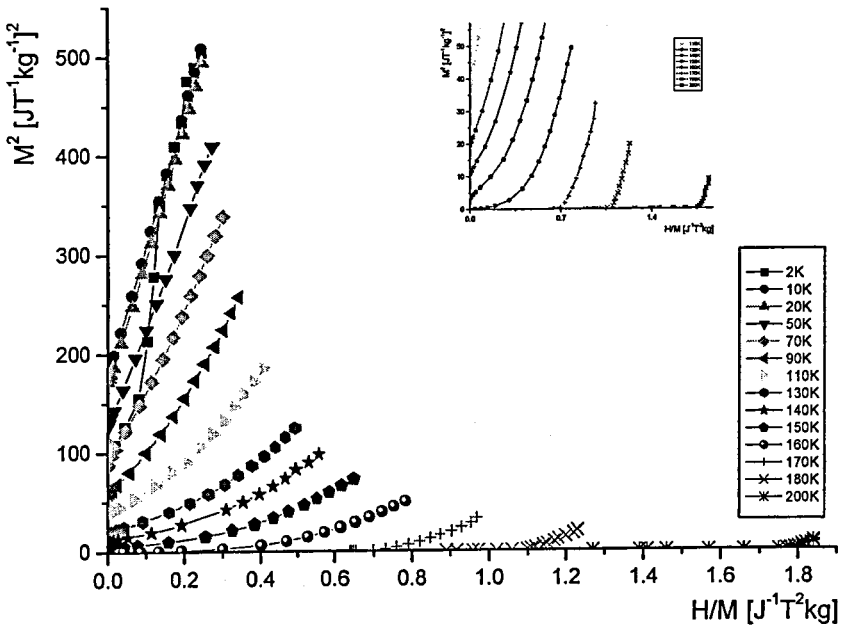

Figure 3.3.17: Arrott plots of $Sr_{0.75}Ca_{0.25}RuO_3$ for various temperatures. Inset figure shows the zoomed view near the transition temperature.

In figure 3.3.17 the Arrott plots of $Sr_{0.75}Ca_{0.25}RuO_3$ are represented. It can be seen that from the inset figure of figure 3.3.17 the plots for T_C<160K intersect the x-axis. These plots will be used to obtain a graph of the inverse magnetic susceptibility and a more precise magnetic phase transition temperature for $Sr_{0.75}Ca_{0.25}RuO_3$.

In figure 3.3.18 the inverse magnetic susceptibility is shown as a function of temperature. An analysis of this plot has been carried out using a linear regression and the data points lie on a straight line. This graph identifies the Curie temperature for $Sr_{0.75}Ca_{0.25}RuO_3$ as 148K (±1.2). The Curie temperature for $Sr_{0.8}Ca_{0.2}RuO_3$ is quoted as 147K in reference [29]. This value agrees well with the one observed in SQUID measurements. This is a more reliable value comparing to one which was obtained from temperature scans at a

finite value of the applied magnetic field. The presence of Ca in the compound should decrease the T_C value compared to the one of $SrRuO_3$ [29].

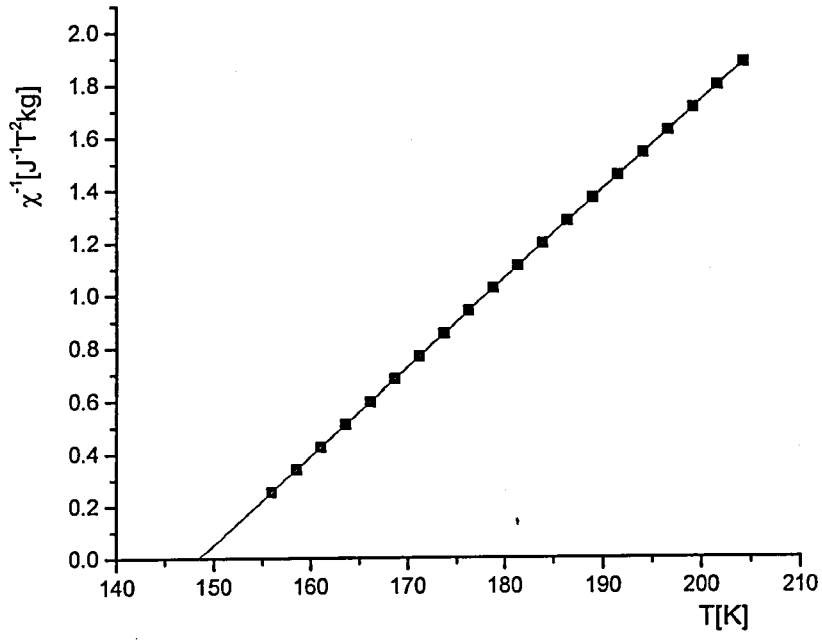

Figure 3.3.18: Inverse magnetic susceptibility as a function of temperature of $Sr_{0.75}Ca_{0.25}RuO_3$. The data points are obtained from Arrott plots.

Further calculation yield a value for the number of the magnetisation per ruthenium atom and the value 2.3(±0.4)μ_B/Ru has been found according to this calculation. The value for paramagnetic effective Bohr magneton in reference [29] is 2.80 μ_B/Ru. The calculated T_C and magnetisation per ruthenium atom from SQUID data agree well with literature values [29].

b) $Sr_{0.5}Ca_{0.5}RuO_3$

A small piece of $Sr_{0.5}Ca_{0.5}RuO_3$ has been measured using the SQUID magnetometer. The magnetisation as a function of temperature is measured at a field of 0.1 Tesla and in the temperature range between 2K and 350K. Figure 3.3.19 represents the results of this measurement.

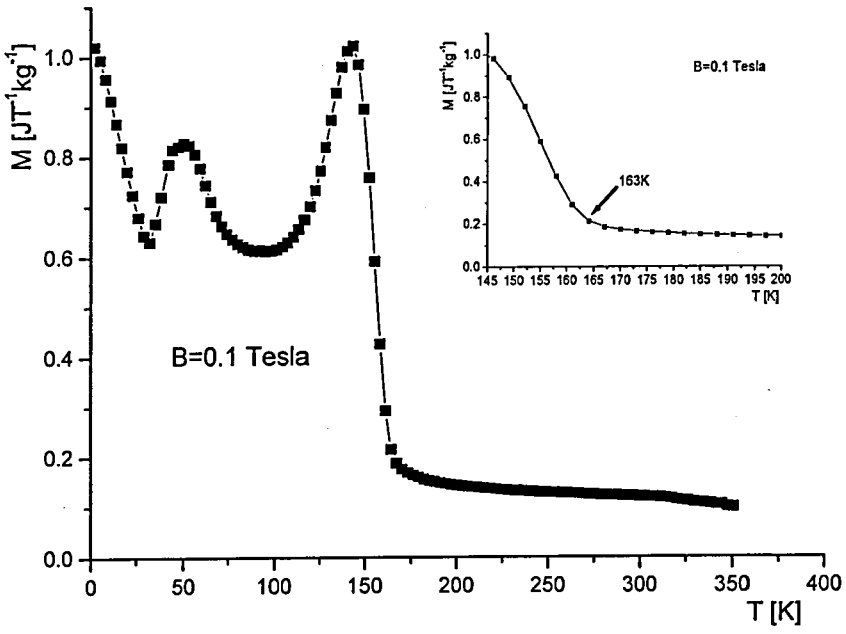

Figure 3.3.19: Magnetisation as a function of temperature at an applied magnetic field of 0.1 Tesla for $Sr_{0.5}Ca_{0.5}RuO_3$.

The low field (0.1 Tesla) magnetisation measurement shows that the $Sr_{0.5}Ca_{0.5}RuO_3$ is a ferromagnetic compound like the other compounds of the $Sr_{(1-x)}Ca_xRuO_3$ family. The transition temperature for $Sr_{0.5}Ca_{0.5}RuO_3$ is 163(±2)K. However, with Arrott plots and inverse susceptibility measurement the Curie temperature will be determined exactly for this compound. The variations below 140(±2)K are caused by the impurity phase $CaRuO_3$ which is mentioned in the section 3.2.4.

The magnetisation of $Sr_{0.5}Ca_{0.5}RuO_3$ was measured for various temperatures (figure 3.3.20). The temperatures above the transition temperature intersect the positive x-axis. The results satisfy the previous works done by I. Felner, *et al* [29]. The variation which has been observed in magnetisation versus temperature graph does not exist here.

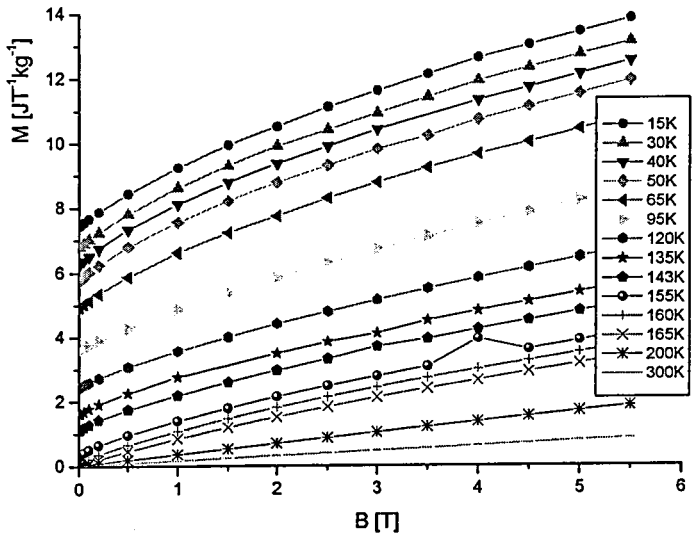

Figure 3.3.20: Magnetisation of $Sr_{0.5}Ca_{0.5}RuO_3$ as a function of applied magnetic field at various temperatures

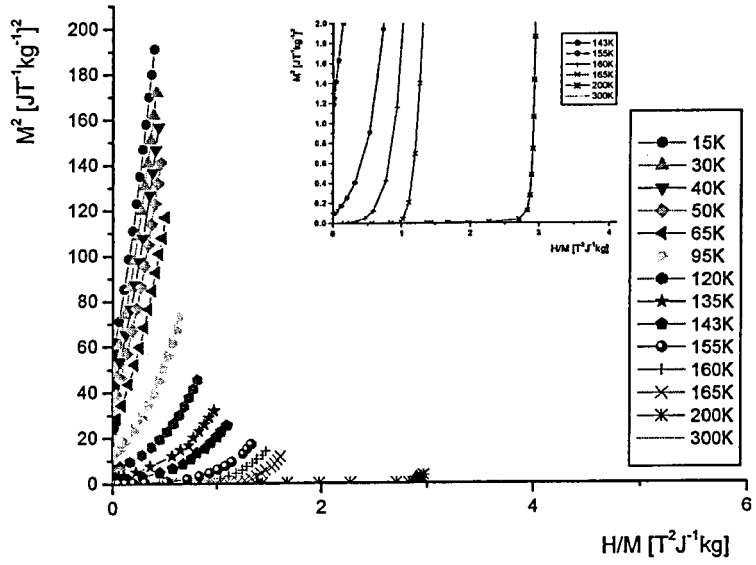

Figure 3.3.21: Arrott plots of $Sr_{0.5}Ca_{0.5}RuO_3$

In graphs 3.3.20 and 3.3.21 Arrott plots of $Sr_{0.5}Ca_{0.5}RuO_3$ clearly represent the magnetic phase transition. $Sr_{0.5}Ca_{0.5}RuO_3$ shows ferromagnetic behaviour in the temperatures lines which intersect the y-axis (M^2) and it shows paramagnetic behaviour for temperatures lines which intersect with the x-axis (H/M). Intersections with the x-axis (H/M axis) yield values of the inverse susceptibility extrapolated to zero magnetic fields.

Further calculation yield a value for the number of the magnetisation per ruthenium atom and the value 2.3(±0.2) μ_B/Ru has been found according to this calculation.

In the figure 3.3.22 the inverse susceptibility is shown as a function of temperature. For temperatures above the transition point of 128(±2)K the inverse susceptibility versus temperature is in excellent agreement with the Curie-Weiss law as shown in figure 3.3.22. The calculation of the values of T_C and magnetisation per ruthenium atom shows good agreement with the literature values [29].

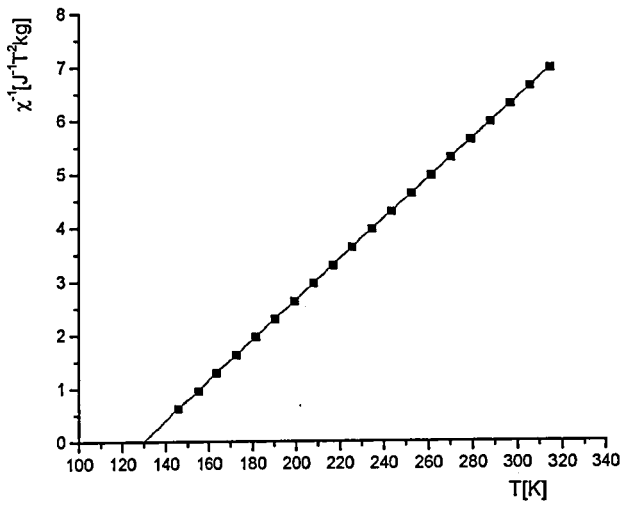

Figure 3.3.22: Inverse susceptibility as a function of temperature of $Sr_{0.5}Ca_{0.5}RuO_3$. This graph is obtained from Arrott plots.

From the inverse susceptibility versus temperature graph, the effective paramagnetic Bohr magneton has been calculated and a value of p_{eff} = 0.98(±0.08) μ_B/Ru has been found.

3.4 Paramagnetic Neutron Scattering

3.4.1 Instrumentation

Paramagnetic neutron scattering experiments have been carried out at the ILL, Grenoble, France using the *Diffuse Scattering Spectrometer, D7.*

D7 is designed to study diffuse scattering arising from disorder phenomena in solids. The diffuse scattering intensity appears between Bragg reflections. It is usually weak and may contain both elastic and inelastic contributions. D7 uses a unique combination of full 3-directional *XYZ*-polarisation analysis using a multi detector setup.

Full 3-directional polarisation analysis enables the experimental separation of nuclear-spin-incoherent, nuclear and magnetic components. Combined with the flexibility of the instrument and the fact that data is collected simultaneously in 64 detectors, this makes D7 a unique instrument. A schematic diagram of D7 can be seen in figure 3.4.1 [33].

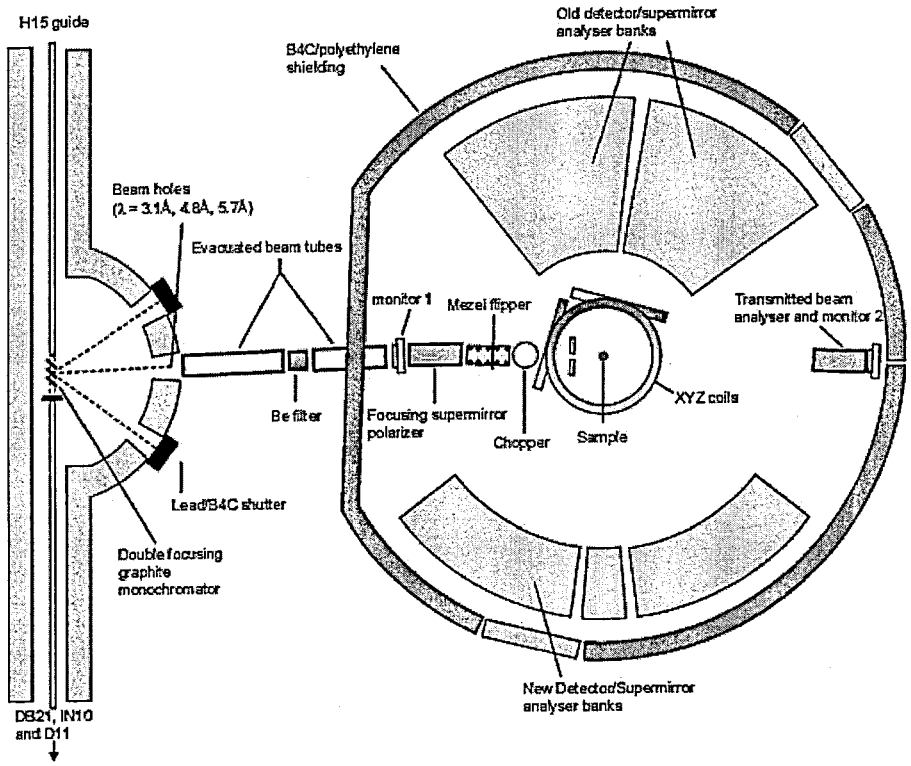

Figure 3.4.1: A schematic diagram of the diffuse scattering instrument D7 [33].

The operation details of D7 instrument have been described in detail in the users manual [33]. The neutron polarizer and analysers can be removed if desired to facilitate conventional neutron diffraction measurements. The inclusion of a neutron disk chopper enables energy analysis of the scattered neutrons by the time-of-flight method. Neutrons from the H15 cold neutron source at the ILL are monochromated by a focusing graphite monochromator crystal array. The take-off angle from the monochromator crystal defines the incident neutron wavelength. The three (nominal) wavelengths available on D7 are 3.1Å, 4.8Å or 5.9Å. For > 3.1Å the neutrons pass through a beryllium filter which removes higher orders of the incident wavelength λ/n where n = 2, 3, ... etc. The neutrons are then polarized by a supermirror bender polarizer and pass through a Mezei π-spin-flipper which is turned on when measuring the Spin-Flip (SF) cross-section and turned off when measuring the Non-Spin-Flip (NSF) cross-section. The neutron polarization, which is in the z-direction, is maintained by a neutron guide field of around 1mT. The neutrons pass through the sample which is placed at the centre of 3 orthogonal coils, known as the spin turn coils. These coils rotate the initial neutron polarization by $\pi/2$ from the z-direction onto the x or y directions before hitting the sample, and then they rotate the scattered neutrons back by $-\pi/2$. This allows the sequential measurement of the SF and NSF cross-sections in each direction.

The neutrons then enter the detector banks, each of which consists of a neutron guide field, 8 removable supermirror analysers and 16 ^{3}He detector tubes (figure 3.4.2). With the supermirror analysers in place only 8 detectors are used in each bank. The 8 detectors are placed 6 degrees apart, each bank subtending an angle of 45 degrees. With four identical banks, there are in total over 5000 supermirrors on D7. The banks can be placed on either side of the instrument and can cover scattering angles from 2θ=7° to 160°.

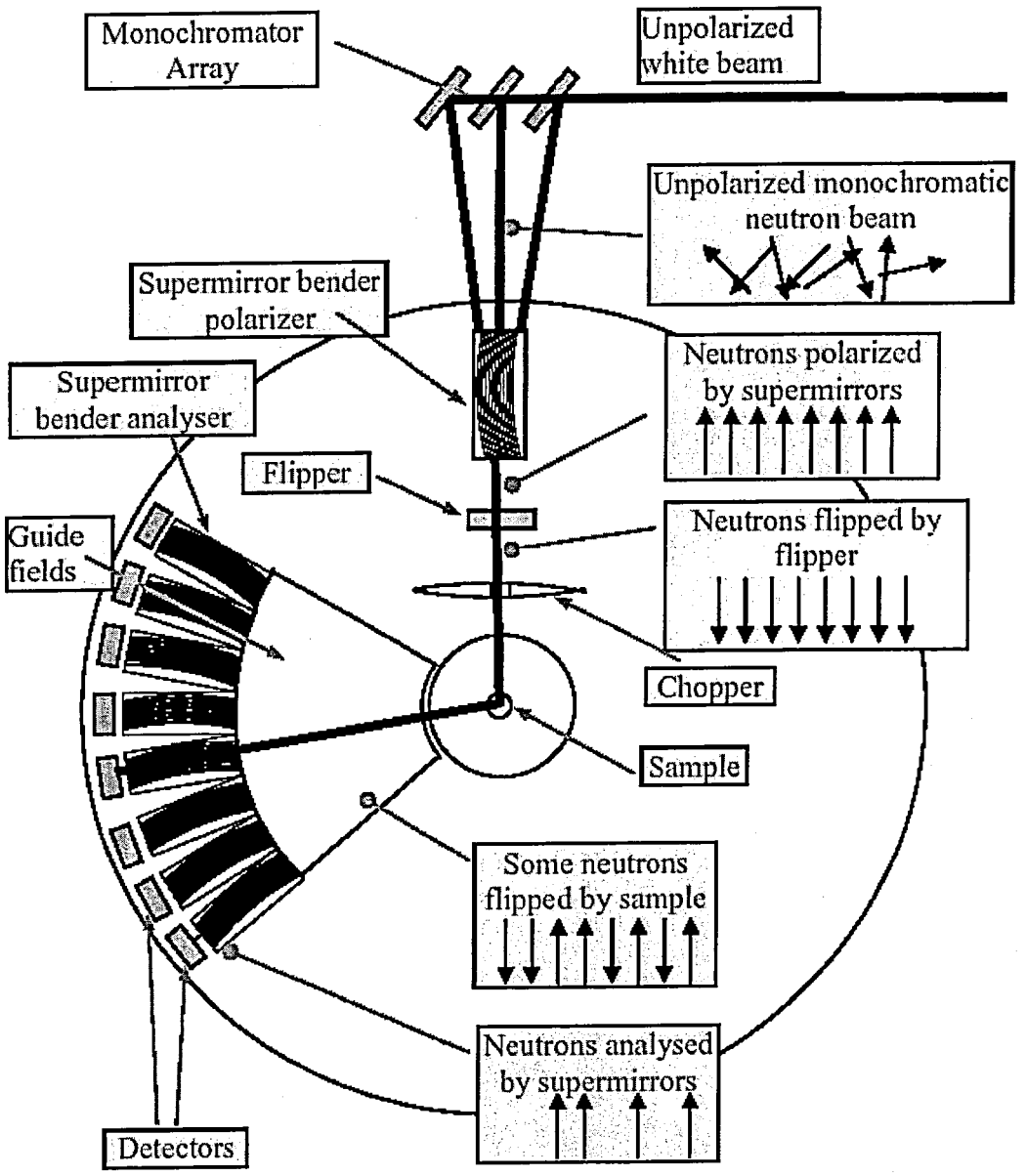

Figure 3.4.2: Aerial view of D7

3.4.2 Data Reduction for Polarisation Analysis

The data reduction for polarisation analysis is described in the D7 manual [33]. According to this manual in order to obtain the absolute cross-section from the raw number of neutron counts, the following corrections must be applied.

- The relative detector efficiency correction
- The spin-dependent analyser transmission correction
- The background scattering correction
- The sample self-attenuation correction
- The absolute scale of cross-section
- Multiple scattering corrections.

All these corrections have been done using the *LAMP* program [33]. Lamp is a computer programs which is written in IDL (Interactive Data Language) and is developed at the ILL. This program helps to reduce and analyse the data which has been obtained from any instrument at the ILL with the help of user supplied macros in IDL. The desired instrument can be chosen via the user friendly interface of Lamp. In this case D7 has been chosen from a drop-down menu. After choosing the instrument and the path for data files the macros should be written. Different macros must be applied for different corrections and than a macro has to be used to reduce an XYZ to an omega scan. All the macros which are used and brief explanations about these macros have been collected in the appendix.

3.4.3 Calculating the Correlation Length from the Polarised Neutron Scattering

The magnetic correlation length can be calculated with the aid of spin polarised neutron scattering and the spin-spin correlation function.

Using the susceptibility data in section 3.3 the expected magnetic scattering at Q=0 can be determined by virtue of the relationship between the spin-spin correlation function and the uniform susceptibility:

$$\sum_j \left\langle \vec{S}_i \cdot \vec{S}_j \right\rangle = 3k_B \chi T \qquad (3.3.1)$$

which in turn is related to the partial differential cross-section by

$$\frac{d\sigma}{d\Omega} = \frac{2}{3}\left\langle \vec{S}_i \cdot \vec{S}_j \right\rangle (r_0\gamma)^2 f^2 \qquad (3.3.2)$$

where $r_0\gamma$ is equal to 0.54×10^{-13} cm and f is the form factor which is unity at Q=0. A more detailed explanation of the relationship between the spin-spin correlation function and the uniform susceptibility is given in the appendix.

3.4.4 Experiments

The investigations were carried out on the instrument D7 at the ILL using a 18.1101g powder sample of $SrRuO_3$ and a 9.5181g powder sample of Sr_2RuO_4 using a neutron wavelength of 5.9Å. The data were collected at 170K, 300K and 535K for $SrRuO_3$ and 2K, 20K, 50K and 450K for Sr_2RuO_4. For all measurements the specimen was contained in a thin walled, aluminium cylinder under a helium atmosphere, located in an orange cryostat. Having optimised the flipper and correction coil current for maximum spin flipper efficiency, calibration measurements were performed. Normalisation to the scattering of a vanadium standard permitted all subsequent sample data to be placed on an absolute scale. The results obtained are as follows:

a) $SrRuO_3$

Lamp [33, 34] has been used for analysing and plotting the graphs for the paramagnetic neutron scattering. When the graphs were extrapolated to the value of the inverse

susceptibility at Q=0, the full width of the maximum yields the correlation length. Figures 3.4.3, 3.4.4 and 3.4.5 give the paramagnetic scattering of the Ruthenium spins in $SrRuO_3$ for various temperatures. The correlation lengths, as obtained from a fit to the peak centred at Q=0, are given table 3.4.1.

Temperature [K]	Uniform Mag. Sus. [barn/sterad]	FWFM [2π/λ]	Corr. Length [Å]
170	10.50	0.075 (5)	83.73 (5)
300	1.05	0.083 (4)	75.66 (4)
535	0.68	0.085 (4)	73.88 (4)

Table 3.4.1: Correlation lengths obtained from a fit to the peak centred at Q=0

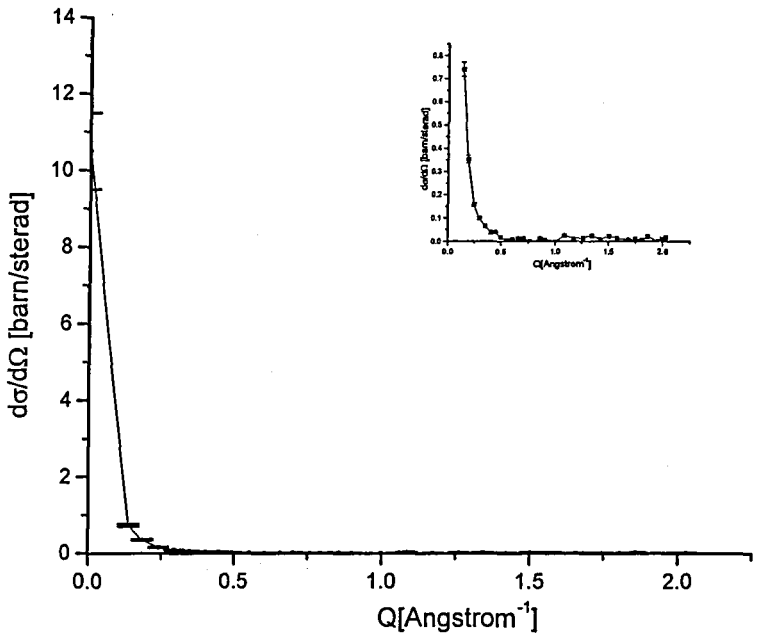

Figure 3.4.3: Paramagnetic neutron scattering of $SrRuO_3$ at 170K.

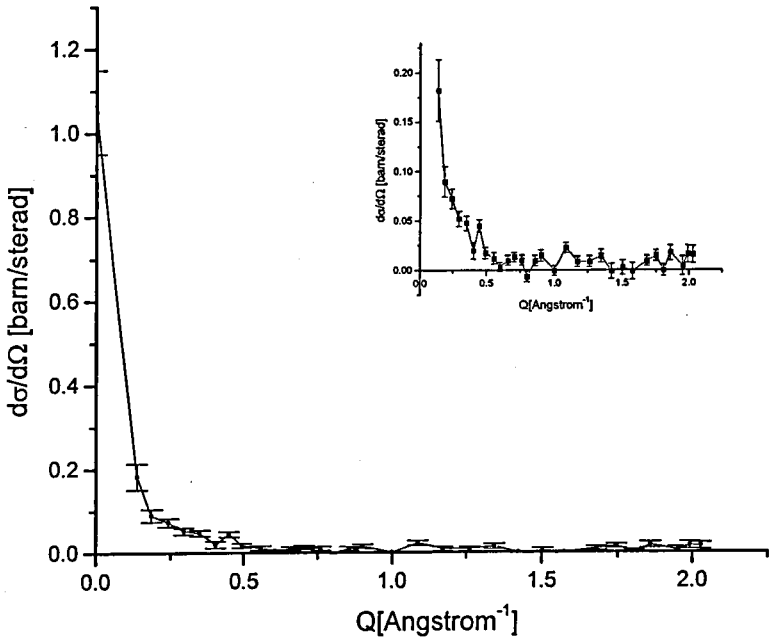

Figure 3.4.4: Paramagnetic neutron scattering of $SrRuO_3$ at 300K

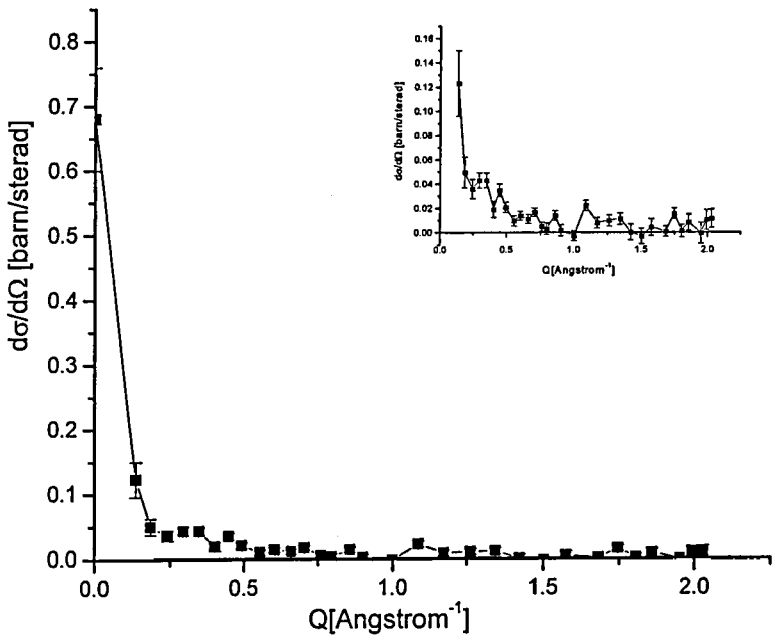

Figure 3.4.5: Paramagnetic neutron scattering of $SrRuO_3$ at 535K

The paramagnetic scattering measured at low temperature is shown in figure 3.4.3 for T=170K. The figures 3.4.4 and 3.4.5 present the paramagnetic scattering at sufficiently high temperatures (300K and 535K respectively) in the paramagnetic regime. From these figures it may be seen that at all temperatures there is a distinguishable scattering at small wave vectors which is strongly enhanced. It is interpreted as evidence for the presence for ferromagnetic correlations. As the temperature decreased the paramagnetic scattering at small wave vectors sharpens. This is due to the magnetic ordering which exists at low temperatures. On increasing the temperature above the transition temperature, strong ferromagnetic correlations persist into the paramagnetic temperature range. For all three figures scattering at large wave vectors does not appear to change as a function of temperature, but rather it remains at the level as observed at low temperatures.

For $SrRuO_3$ the magnetic correlation length at various temperatures for $SrRuO_3$ has been calculated using the forward peak in figures 3.4.3, 3.4.4 and 3.4.5. Near the ferromagnetically ordered region (at 170K, figure 3.4.3) the value of correlation length has been calculated as 83.73Å. With increasing temperature the ferromagnetism vanishes and the correlation length decreases to 71.36Å at 300K. The correlation length at 535K is 72.34Å and it is essentially unchanged compared to the value at 300K.

The reason of why no enhancement of Bragg reflections is observed at higher wave vectors is due to the rapid decrease of the magnetic form factor. The delocalisation of electrons on the ruthenium cause this rapid decrease. Hence no magnetic short range order is seen around Bragg peak positions the correlation length being of the order of ten unit cells.

b) Sr_2RuO_4

Due to the ferromagnetic $SrRuO_3$ impurity in the Sr_2RuO_4 compound which was prepared for magnetic measurements, the correct inverse susceptibility could not be determined. Hence, the lack of inverse susceptibility does not allow the calculation of the magnetic correlation length. The experiment has been done at 2K, 20K, 50K, 450K. The graphs can bee seen in figures 3.4.6, 3.4.7. 3.4.8 and 3.4.9.

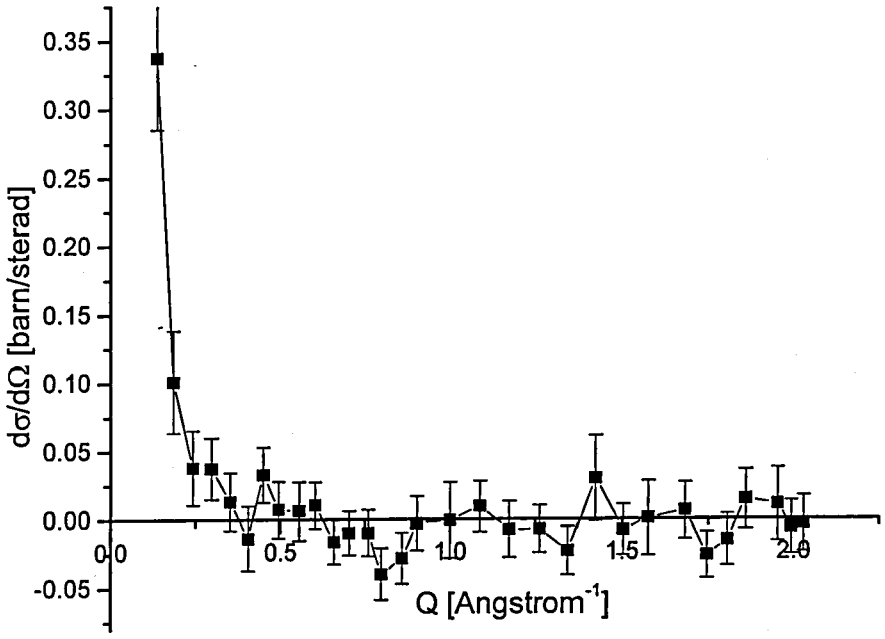

Figure 3.4.6: Paramagnetic neutron scattering of Sr_2RuO_4 at 2K

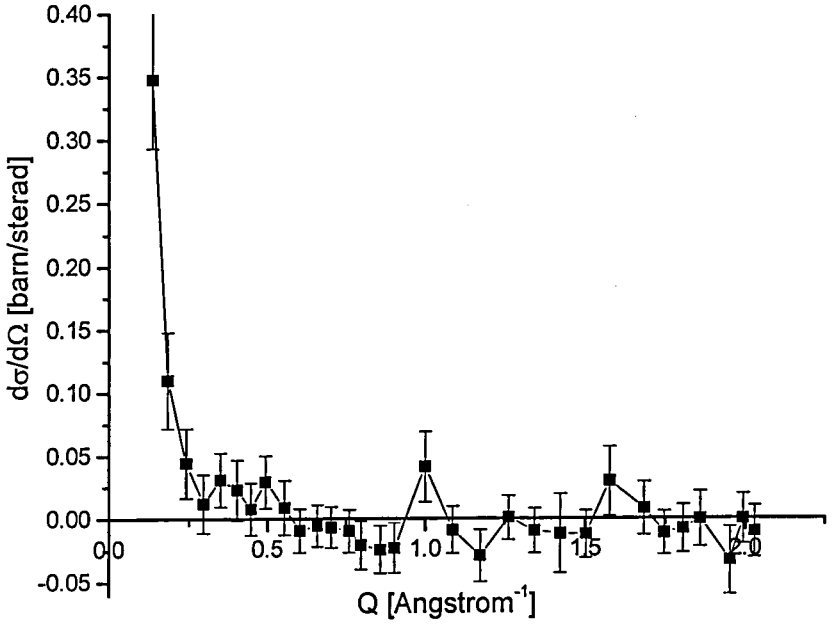

Figure 3.4.7: Paramagnetic neutron scattering of Sr_2RuO_4 at 20K

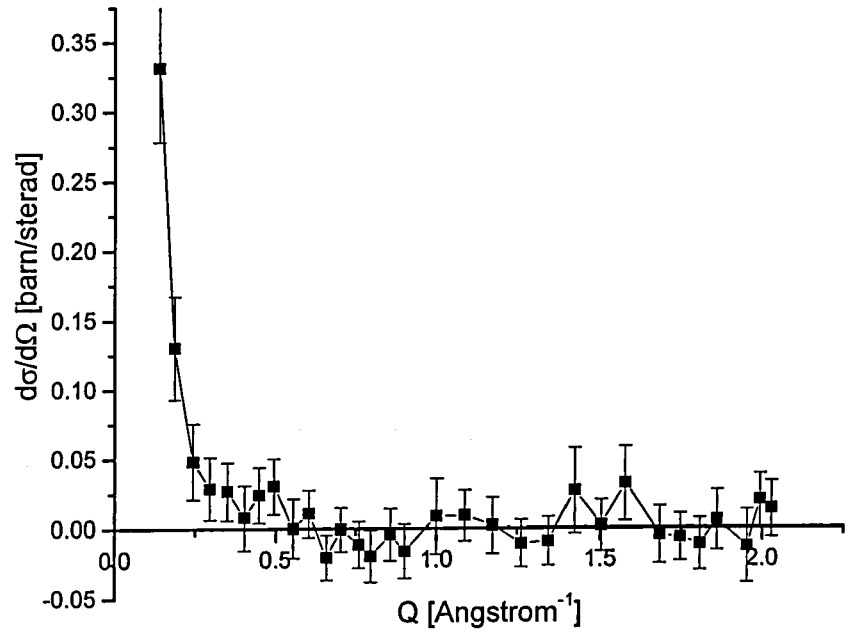

Figure 3.4.8: paramagnetic neutron scattering of Sr_2RuO_4 at 50K

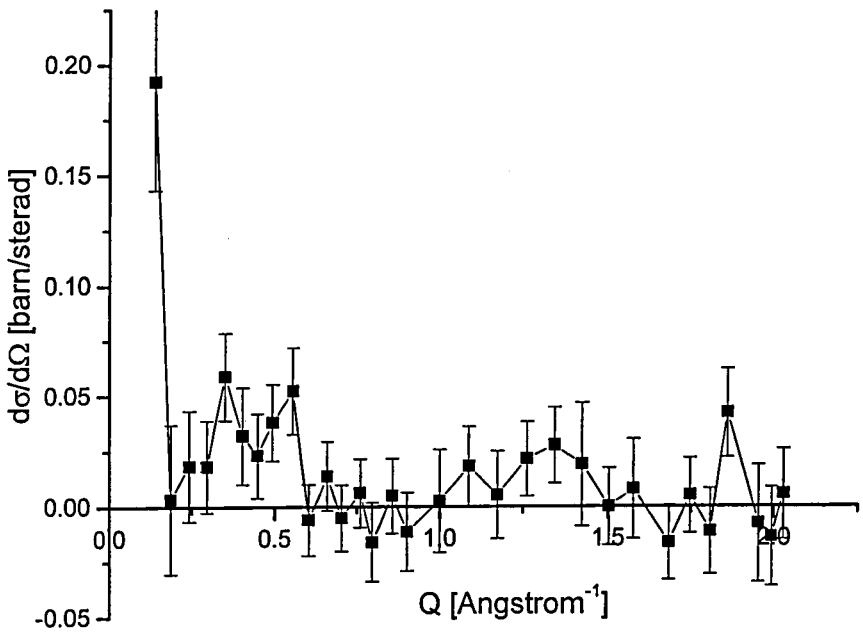

Figure 3.4.9: paramagnetic neutron scattering at 450K for Sr_2RuO_4

Although it is well known that Sr_2RuO_4 is not magnetically ordered even at low temperatures, there is a distinguishable peak at small wave vectors. As mentioned in detail in the magnetisation measurements section (section 3.3.3) there is an impurity phase of $SrRuO_3$ less then 1%. This impurity is the reason for this sharp peak. This sharp peak arises from the ferromagnetic nature of $SrRuO_3$. As expected and described in the previous section (section 3.3.4.a) no Bragg peaks have been observed due to the rapid decrease of form factor.

References

[1] Alfa Aesar, Johnsons Matthey Company, private communication.

[2] Boman, C. E., *J. Acta Chem. Scan. 24*, 116, (1970)

[3] Hahn., T., *International Tables for Crystallography, Vol. A,* D. Reidel publishing Company, (1987)

[4] Haines, J., Leger, J. M., *Phys. Rev., B* **48**, 13344, (1993)

[5] Roisnel, T., Rodriguez-Carvajal, J., *FullProf,*
Can be downloaded from: http://www-llb.cea.fr/fullweb/winplotr/winplotr.htm

[6] Burns, G., Glazer, A. M., *Space Group for Solid States Scientists*, Academic Press, (1990)

[7] Glazer, A. M., *Acta Cryst., B* **28**, 3384, (1972)

[8] Randall, J. J., Ward., R., *Acta Cryst.,* **81**, 2629, (1954)

[9] de Villiers, J. P. R., *The American Mineralogist,* **56**, 759, (1971)

[10] Jarosch, D., Heger, G., *Bull. Mineral,* **111**, 139, (1988)

[11] *International Tables for X-ray Crystallography, Vol. 1*, Kynoch Press, (1969)

[12] Kennedy, B. J., Hunter, B. A., *Phys. Rev., B* **58**, 653, (1998)

[13] Jones, W. C., Battle, P. D., *et al., Acta Cryst., C* **45**, 365, (1989)

[14] Shinkano M., Huang, T.-K., Inaguma, Y., Itoh, M., Nakamura, T., *Solid State Comm.,* **90**, 115, (1994)

[15] Bouchard, R. J., Gillson J. L., *Mat. Res. Bull.*, 7, 873, (1972)

[16] Kurmaev, E. Z., *et. al. Phys. Rev., B* **57**, 1558, (1998)

[17] X-Ray Generator, *Philips manual of Diffraction Kit PW 1300/00/60*

[18] Chakoumakos, C., Nagler, S. E., *et al., Physica B,* **241**, 358, (1998)

[19] Kiyama, T., *et. al. Phys. Rev., B* **54**, R756, (1996)

[20] Kobayashi, H., Nagata, M., *et al., Mat. Res. Bull.*, **29**, 1271, (1994)

[21] Ladd, M., Palmer, R., *Structure determinations by X-ray Crystallography,* Kluwer Academic / Plenum Publishers, (2003)

[22] Oguchi, T. *Phys. Rev. B.*, **51**, 1385, (1995)

[23] Dodge, J. S., *et al., Phys. Rev., B,* **60**, R6987, (1999)

[24] Smyth, J. R., Ahrens, T.J., *Geophysical Research Letters*, **23**, 1595, (1997)

[25] Wartchow, R., *Zeitschrift fur Kristallographie*, **186**, 300, (1989)

[26] Bensch, W., Schmalle, H. W., Reller, A., *Solid States Ionics,* **43**, 171, (1990)

[27] Wlaz, L., Lichtenberg, F., *Acta Cryst., C* **49**, 1268, (1993)

[28] Shikano, M., Huang, T., *et al., Solid State Comm.*, **90**, 115, (1994)

[29] Felner, I., Asaf, U., *Physica B*, **337**, 310, (2003)

[30] MPMS Software System Reference Manuel, Quantum Design (1990)

[31] Sidis, Y., Braden, M., *et al. Phys. Rev. Lett.*, **83**, 3320, (1999)

[32] Rodriguez-Carvajal, J., *Fullprof User Manual*, (1998)

[33] Stewart, J. R., *D7 Users Guide*, (2001). (Available on request from the author via e-mail: stewart@ill.fr)

[34] Richard, D., Ferrand, M., Kearley, G. J., *The Lamp Book, ILL.* Can be printed from: http://www.ill.fr/data_treat/lamp/front.html

Chapter 4
Discussion and Conclusion

4.1 Crystallographic Structures

The observed crystallographic structures according to X-ray diffractions and neutron scattering experiments have been shown in chapter three. All results agree with previous works.

$SrRuO_3$ occurs in a distorted perovskite structure at room temperature, specifically, it crystallises in the $GdFeO_3$ structure type with orthorhombic *Pnma* symmetry. This is typical for perovskites with an A-site cation that is too small relative to the B-site. The distortion consists of rotations of the oxygen octahedra with very little change in Ru-O bond lengths. $CaRuO_3$ has the same structure and space group as $SrRuO_3$, but, oxygen octahedral are tilted more and they are distorted further than $SrRuO_3$, because the ionic radius of Ca (0.99Å) is even less ideal for perovskite formation than Sr (1.18Å). As a result the $CaRuO_3$ compound has a smaller unit cell size compared to its analogue compound $SrRuO_3$.

All $Sr_{(1-x)}Ca_xRuO_3$ (x=0.5 and 0.75) compounds possess the same symmetry and crystallographic properties as $SrRuO_3$. With increasing concentration of Ca ions, the unit cell shrinks and thus the unit cell volume decreases. The tilting in Ru-O bond directions is also rising.

The impurity phase of $CaRuO_3$ in $Sr_{0.5}Ca_{0.5}RuO_3$ compound has made the refinement difficult. This impurity phase has not affected the crystallographic structure of $Sr_{0.5}Ca_{0.5}RuO_3$ and all the values which are obtained exhibit good agreement with published works.

The X-ray and neutron scattering experiments show that, Sr_2RuO_4 crystallises in the K_2NiF_4 structure type with the *I4/mmm* space group which is realised for a considerable number of compounds with the general composition A_2BX_4. The structure of Sr_2RuO_4 can be built up by three perovskite monolayers stacked along the resulting *c*-axis where layer 1 and 3 are ABX_3 perovskite cells centred with *B* atoms. Removing two BX_2 layers leads to the K_2NiF_4 structure.

4.2 Magnetic Investigations and Magnetic Structures

For investigating the magnetic properties and structures of $SrRuO_3$, $CaRuO_3$, Sr_2RuO_4 and $Sr_{(1-x)}Ca_xRuO_3$ SQUID measurements have been undertaken. For a more detailed magnetic investigation of $SrRuO_3$ and Sr_2RuO_4 paramagnetic neutron scattering experiments have been performed. For Sr_2RuO_4 the magnetic investigations have been obstructed due to the impurity phase $SrRuO_3$. As a consequence, the magnetic investigation for this compound is not reliable.

The experiments show that perovskite $SrRuO_3$ is ferromagnetic with T_C= 162K and the paramagnetic effective Bohr magneton number has been calculated as 3.17(±0.1) μ_B/Ru in the low spin state (s=1). On the other hand, $CaRuO_3$ was not ordered magnetically down to 2K. The inverse magnetic susceptibility measurements show that the paramagnetic Curie temperature for $CaRuO_3$ is -126K. When moved to $Sr_{(1-x)}Ca_xRuO_3$ compounds it can be seen that the ferromagnetic ordering is getting weaker with increasing Ca concentration and vanishes when x=1.

While both $SrRuO_3$ and $CaRuO_3$ have the same number of d-electrons, $SrRuO_3$ is ferromagnetic and $CaRuO_3$ is paramagnetic. This is obtained using SQUID and neutron diffraction experiments at low temperatures (2K). It showed that no additional magnetic neutron scattering peaks exist, indicating that $CaRuO_3$ is paramagnetic. The peaks which emerge in low temperature neutron scattering spectra of $SrRuO_3$ provide experimental proof that this compound has a ferromagnetic ground state.

While discussing bonding qualitatively, some authors proposed that the Ru-O t_{2g} bands are narrower in $CaRuO_3$ than in $SrRuO_3$ because of the ionic radius of Ca. This research supports this argument by X-ray diffraction and neutron scattering experiments. For structure determination experiments showed that $CaRuO_3$ is more distorted than $SrRuO_3$, which is very close to cubic. This should also decrease the Ru-O overlap and thereby reduce the width of π-bands. Furthermore, the unit cell volume of $CaRuO_3$ is smaller than that of $SrRuO_3$. This factor will act to increase the Ru-O interaction.

The stark contrast between $SrRuO_3$ and $CaRuO_3$ arises because of the closed shell s-like characters of Sr and Ca do not contribute to the density of states at the Fermi surface and therefore should not be the origin for the different magnetic ground states of these two compounds. One common structural feature of the two compounds is that they are composed of an array of corner-sharing RuO_6 octahedra. It is assumed that the degree of tilting and rotation of these octahedra within their ideal cubic-perovskite structure governs the observed differences in the magnetic ground states. A narrow itinerant $4d$ band is formed through hybridisation of Ru t_{2g} and O $2p$ orbitals. The octahedral crystalline electric field of O atoms splits the fivefold degeneracy of the Ru $4d^4$configuration into a triplet (t_{2g}) ground state, two-thirds occupied, and a doublet (e_g) excited state, unoccupied. The magnetism of $SrRuO_3$ and related ruthenates are influenced heavily by the covalent coupling of the Ru d shell to the O $2p$ electrons. It is believed that $CaRuO_3$ has a narrower itinerant $4d$ bandwidth than $SrRuO_3$ which is too narrow for long range magnetic order but not too narrow as to cause $CaRuO_3$ to be non-metallic. The bandwidth has been calculated and published [1]. This supports the magnetic measurements, which have been done for this research project. $CaRuO_3$ is on the edge of magnetic ordering and tends towards an ordered phase. With increasing Ca concentration in $Sr_{(1-x)}Ca_xRuO_3$ compounds the bandwidth gets narrower and with sufficient Ca ions ($x>0.3$) the compound starts to exhibits ferromagnetic ordering.

The paramagnetic neutron scattering experiments clearly indicate that the investigated ruthenate compounds have itinerant electrons rather than localised electrons as claimed in the literature. The itinerant electrons cause a drop of the form factor and hence no magnetic Bragg peaks or magnetic short range order close to nuclear Bragg reflections could be observed.

This research showed that the ruthenium oxides, which are transition metal oxides with a perovskite structure exhibit a variety of physical properties ranging from ferromagnetism ($SrRuO_3$) to paramagnetism ($CaRuO_3$), from a cubic structure (at high temperature) to orthorhombic, from metallic to insulating. Moreover, $Sr_{(1-x)}Ca_xRuO_3$ shows a rapid decrease in T_C with increasing Ca content. On the other hand the layered compound

Sr_2RuO_4 is the first copper free low temperature superconductor. The origin of the magnetism in $SrRuO_3$ is still not clear and the reason for the occurrence of superconductivity in Sr_2RuO_4 is still being discussed. In the future more detailed work has to be carried out on single crystals in order to clarify the structural, electrical and magnetic properties of these ruthenates.

References

[1] Mazin, I. I., Singh, D. J., *Phys. Rev., B* **56,** 2556 (1997)

Appendix

1.1 Macros for analysing the Paramagnetic Neutron Scattering

The following macros have been applied to $SrRuO_3$ at 170K data. The macros are similar for other compounds at various temperatures. Only the data file names need to be changed.

a) Quartz Correction

The incident beam polarizer and the analysers before the detectors are not perfect. A small number of neutrons with the wrong spin state always manage to pass through. To correct for this, a run is performed with an amorphous silicate (quartz) sample. Quartz is a perfect nuclear-incoherent scatterer with nuclei which do not possess a nuclear spin. Any signal picked up in the spin-flip channel must therefore arise from non-ideal polarization. The following macro has been applied for extracting the flipping ratios:

```
;quartz

w1= rdsum(73992, 73994)                ;quartz (up to 74995)
w2= normalise (w1, /monitor)

w3= rdsum (73996, 73999)
w4= normalise (w3, /monitor)           ;quartz empty

w5= background (sample = w2, empty = w4, T = 0.9)
w6= quartz(w5)
```

The numbers from 773992 to 73994 represent the data file name for quartz and from 73996 to73999 data file name represent the quartz holder. The line w5 corrects for the background and line w6 calls a macro quartz.pro which takes the background-corrected data file w5, calculates the flipping ratios, puts the result into w6 and writes the flipping ratios to a file quartz_73994.dat. This file is then used later in the analysis to make the flipping ratio correction.

b) Vanadium Correction

Vanadium is a purely nuclear spin-incoherent scatterer and nuclear spin-incoherent scattering is by definition isotropic. This helps to correct for the detector efficiency. Each detector has a different efficiency. The intensity seen in each detector is a measurement

of the apparent detector efficiency and also the analyser transmission. The following macro has been applied for vanadium corrections:

```
; vanadium

w1 = rdsum(74068,74069)                ;vanadium measurement
w2 = normalise(w1, /monitor)

w3 = rdsum(74063,74065)                ;empty measurement
w4 = normalise(w3,/monitor)

w5 = rdsum(74066,74067)                ;cadmium measurement
w6 = normalise(w5,/monitor)

w5 = background(sample = w2, empty = w4, cadmium = w6, T = 0.7825)
w6 = vanadium(w5)
```

The line w6 calls a macro vanadium.pro. This macro adds the non-spin-flip and spin-flip scattering together and puts the total intensities into w6. It also writes them to a file vanadium_74069.dat. This file is used later in the analysis.

c) Macro for XYZ Method of Polarisation Analysis

The XYZ difference technique has been used to separate the magnetic scattering from all other types of scattering. The macro for this technique is as follows:

```
;SrRuO3 170K_new 5.7Ang

w1= rdsum(74012,74020)                 ;sample
w8=normalise(w1,/monitor)
;-------------------------------------------------------------
w1= rdsum(74063,74065)                 ;empty
w7=normalise(w1,/monitor)
;-------------------------------------------------------------
w1=rdsum(74066,74067)
w6=normalise(w1,/monitor)              ;cadmium
;=============================================================
w17 = background(sample = w8, empty = w7, cadmium = w6, T = 0.969222)
w18=zero_detectors(w17,[58])

w9 = corr_xyz(w18, filenum= 73994)  ;flipping ratio corr.
w10 = norm_van(w9, filenum = 74069, S_Mass=18.1101,Fwt=236.535, V_mass=
9.0755) ;vanadium normalisation

w11 = components(w10)
```

```
w12 = theta_scan(w11, /all)
w13 = phi2q(w12)

w14 = w13(*,0) & y_tit(14) = y_tit(13)
w_tit(14) = 'Total '+ STRTRIM(w_tit(13))
w15 = w13(*,1) & y_tit(15) = y_tit(13)
w_tit(15) = 'Spin-Incoherent '+ STRTRIM(w_tit(13))
w16 = w13(*,2) & y_tit(16) = y_tit(13)
w_tit(16) = 'Nuclear '+ STRTRIM(w_tit(13))
w17 = w13(*,3) & y_tit(17) = y_tit(13)
w_tit(17) = 'Magnetic '+ STRTRIM(w_tit(13))

;w15= binq(w15, dQ=0.05)
;w20= total(w15(2:30))/26*1000,sqrt(total(e15(5:30)*e15(5:30)))/27/1000
;output, w20, file='deneme03.dat'

;output, w14, file='srruo3_170_total_woc.dat'
;output, w15, file='srruo3_170_spin-inc_woc.dat'
;output, w16, file='srruo3_170_nuclear_woc.dat'
;output, w17, file='srruo3_170_magnetic_woc.dat'
```

The zero_detectors macro in the line w18 zeroes bad detectors. In line w9 the corr_xyz macro file has been applied. This makes the flipping ratio correction with the aid of the vanadium file. Line w10 calls the macro norm_van which helps to correct detector efficiency and also provides an absolute normalisation, the data is then normalised to an absolute scale in units of barn/steradian. The components macro which is in the line w11, provides a macro for extracting the various contributions such as incoherent, coherent, magnetic, etc scattering. The theta_scan macro in line w12 rearranges the data in ascending order of the magnitude of the scattering angle and phi2q in line w13 transforms the x-scale from scattering angle in degrees to wave vector Q ($Å^{-1}$).

1.2 The Magnetic Correlation Function

If relativistic effects are unimportant and spin is conserved the observed scattering will extrapolate to the cross section at Q=0 given by the uniform susceptibility χ *i.e.* the ω=0 susceptibility. Thus as $Q \rightarrow 0$ the spectrometer D7 is able to integrate over all scattering for all temperatures used in the study. The spin-spin correlation function $\langle \vec{S}_q \cdot \vec{S}_{-q} \rangle$ at Q=0 is given by $\sum_j \langle \vec{S}_i \cdot \vec{S}_j \rangle = 3k_B \chi T$ which is related to the partial differential cross

section by $\frac{d\sigma}{d\Omega} = \sum_j \frac{2}{3}\left\langle \vec{S}_i \cdot \vec{S}_j \right\rangle (r_0\gamma)^2 f^2$ where $r_0\gamma$ is equal to $0.54\text{x}10^{-13}$ cm and f is the form factor which is unity at Q=0.

The magnetic correlation function

$$S(\vec{q},\omega) = \int_{-\infty}^{\infty} dt e^{-i\omega t} \sum_{i,j} e^{iq(\vec{R}_i - \vec{R}_j)} \left\langle \vec{S}_i(t) \cdot \vec{S}_j(0) \right\rangle \tag{A.1}$$

is related to the imaginary part of the dynamic susceptibility via

$$S(\vec{q},\omega) = \frac{1}{1 - e^{-\frac{\hbar\omega}{kT}}} \chi''(\vec{q},\omega) \tag{A.2}$$

For a system of local magnetic moments a sum rule for the scattering can then be defined

$$\sum_q \int_{-\infty}^{\infty} d\omega S(\vec{q},\omega) = \int_{-\infty}^{\infty} d\omega \sum_q \int_{-\infty}^{\infty} dt e^{-i\omega t} \times \sum_{i,j} e^{iq(\vec{R}_i - \vec{R}_j)} \left\langle \vec{S}_i(t) \cdot \vec{S}_j(0) \right\rangle \tag{A.3}$$

which yields

$$N\left\langle S^2 \right\rangle = NS(S+1) \tag{A.4}$$

Typically the sum rule is obtained by integrating the scattering up to some finite energy, which for a system in an ordered ground state usually is the maximum spin wave energy $\sim k_B T_C$. At finite temperatures the moments become directionally disordered but their magnitudes remain fixed. Thus the paramagnetic phase is characterised by disordered local moments. If the integration is carried out over the whole range of q and ω the sum rule is obtained. In the paramagnetic phase the response is diffusive and centred on ω=0 with a width $\Delta\omega$ which increases from zero at q=0 to its maximum value at the zone boundary.